ORNL/TM-2023/3108

Prioritization of Existing Reactor Materials

Sebastien Dryepondt, Stephen Taller, Fred List, Zackary Snow, Michael McMurtrey, Michael Moorehead, Michael Mulholland, Srinivas Aditya, Mantri, Xuan Zhang, Subhashish Meher, Chinthaka Silva, Mohan Sai Kiran Kumar Yadav Nartu, Ankit Roy, William Frazier, Mageswari Komarasamy, Tanvi Ajantiwalay, Shalini Tripathi, Nathan Canfield, Isabella van Rooyen

September 2023

M2CT-23OR1304052

OAK RIDGE National Laboratory

ORNL IS MANAGED BY UT-BATTELLE LLC FOR THE US DEPARTMENT OF ENERGY

ORNL/TM-2023/3108

Advanced Materials and Manufacturing Technologies

PRIORITIZATION OF EXISTING REACTOR MATERIALS

Sebastien Dryepondt*
Stephen Taller*
Fred List*
Zachary Snow*
Michael McMurtrey†
Michael Moorehead†
Michael Mulholland†
Srinivas Aditya‡
Mantri, Xuan Zhang‡
Subhashish Meher§
Chinthaka Silva§
Mohan Sai Kiran Kumar Yadav Nartu§
Ankit Roy§
William Frazier§
Mageswari Komarasamy§
Tanvi Ajantiwalay§
Shalini Tripathi§
Nathan Canfield§
Isabella van Rooyen§

* Oak Ridge National Laboratory
† Idaho National Laboratory
‡ Argonne National Laboratory
§ Pacific Northwest National Laboratory

September 2023

M2CT-23OR1304052

Prepared by
OAK RIDGE NATIONAL LABORATORY
Oak Ridge, TN 37831
managed by
UT-BATTELLE LLC
for the
US DEPARTMENT OF ENERGY
under contract DE-AC05-00OR22725

CONTENTS

LIST OF FIGURES

LIST OF TABLES

ABBREVIATIONS

AFA	alumina-forming austenitic
AGR	Advanced Gas-cooled Reactor
AM	additive manufacturing
AMMT	Advanced Materials and Manufacturing Technologies
ANL	Argonne National Laboratory
ASME	American Society of Mechanical Engineers
AsP.	as-printed
Bal.	balanced
BC	band contrast
bcc	body-centered cubic
BD	build direction
BF	bright-field
BSE	backscattered electron
BSE-SEM	backscattered scanning electron microscopy
CT	computed tomography
DBTT	ductile-to-brittle transition temperature
DED	directed energy deposition
DL	dislocation loop
DOE	US Department of Energy
EBM	electron-beam melting
EBSD	electron backscatter diffraction
EDS	energy-dispersive x-ray spectroscopy
fcc	face-centered cubic
GB	grain boundary
GE	General Electric
GFR	gas-cooled fast reactor
HAADF	high-angle annular dark-field
HFIR	High Flux Isotope Reactor
HIP	hot isostatic pressing
HV	Vickers hardness
INL	Idaho National Laboratory
IPF	inverse pole figure
IQ	image quality
KAM	kernel average misorientation
LANL	Los Alamos National Laboratory
LD	line dislocation
LMP	Larson–Miller parameter
Long.	longitudinal
LPBF	laser powder bed fusion
MC	metal carbide
MDF	Manufacturing Demonstration Facility
ML	machine learning
MO	metal oxide
MSR	molten salt reactor
ND	not determined
NDE	nondestructive examination
NE	nuclear energy
NIR	near-infrared

NN	neural network
NP	nanoparticle
ODS	oxide dispersion strengthened
ORNL	Oak Ridge National Laboratory
PAC	Powder Alloy Corporation
Per.	Perpendicular
PF	pole figure
PNNL	Pacific Northwest National Laboratory
PREP	plasma rotating electrode process
SCC	stress corrosion cracking
SEM	scanning electron microscopy
SS	stainless steel
STEM	scanning transmission electron microscopy
TCR	Transformational Challenge Reactor
TEM	transmission electron microscopy
TS	tensile strength
VED	volumetric energy density
VHTR	very high-temperature reactor
XRD	x-ray diffraction
YS	yield strength

ABSTRACT

The Advanced Materials and Manufacturing Technologies (AMMT) Program is aiming at the faster incorporation of new materials and manufacturing technologies into complex nuclear-related systems. An integrated approach, combining advanced characterization, high-throughput and accelerated testing, modeling and simulation, including machine learning and artificial intelligence, will be employed. Although 316H (Fe–[16–18]Cr–[10–14]Ni–[2–3]Mo–[0.04–0.1]C) has been identified as a key alloy to be integrated into the AMMT accelerated alloy qualification approach because of its relevance for many current and future nuclear energy reactors, many other alloys could be considered for the advanced fabrication of innovative, high-performance nuclear components. Argonne National Laboratory (ANL), Idaho National Laboratory (INL), Oak Ridge National Laboratory (ORNL), and Pacific Northwest National Laboratory (PNNL) are collaborating on identifying the most promising alloy candidates relevant for the AMMT Program. A selection criteria matrix was established to evaluate the alloys considering their relative importance and technological readiness levels for nuclear energy applications, with a focus on laser powder bed fusion (LPBF). Because of the broad range of potential candidate alloys, ORNL and INL focused on nickel-based alloys, and ANL and PNNL mainly evaluated iron-based alloys. PNNL previously published material scorecards reports on several key alloys, and this report provides a broader overview of iron- and nickel-based candidate alloys, expending beyond alloys well-known to the nuclear community.

Among the nickel-based alloys, Alloys 718 (Ni–[17-21]Cr–[4.75–5.5]Nb–[2.8–3.3]Mo–[0.65–1.15]Ti–[0.2–0.8]Al, 625(Ni–[20-23]Cr–[8–10]Mo [3.15–4.15]Nb), and 282 (Ni–20Cr–10Co–8.5Mo–2.1Ti–1.5Al) were considered the most promising alloys because of their printability, superior properties, significant amount of existing data, availability of commercial powder feedstock, and industry experience in fabricating complex components. All these alloys received great scorecards, but most of the other nickel-based alloys could not be evaluated in detail because of the lack of information on additively manufactured versions of these alloys. Generating data on molten salt–resistant Hastelloy N or Haynes 244 should be considered in the future because these alloys might be key to the development of molten salt reactors.

To assess the integration of Alloy 282 into the AMMT digital manufacturing framework, ORNL performed the rapid optimization of Alloy 282 printing parameters on a Renishaw 250 machine, the fabrication of sufficient materials for extensive characterization and mechanical testing both at ORNL and INL, and added the printing data into the digital platform via the Peregrine software. INL conducted an annealing study to determine the optimum heat treatment for LPBF 282 and concluded that 1 h at 1,180°C would result in a grain size after recrystallization that should provide a balance between the creep and fatigue properties of the alloy. Additionally, a detailed analysis of the LPBF Alloy 718 was conducted, with creep specimens being tested at 600°C–650°C and characterized by advanced electron microscopy. The alloy's superior creep strength confirmed that LPBF 718 is a promising candidate alloy for the AMMT Program.

Six different iron-based alloys were selected: three austenitic stainless steels (A709, D9, and alumina-forming austenitic [AFA]) and three ferritic/martensitic steels (HT9, Grade 91, Grade 92). Customized powders were obtained from vendors in small quantities to fabricate initial prints to check the printability of these specific alloys.

In total, 72 single track experiments were performed on two alloy systems—one austenitic stainless steel (A709) and one ferritic/martensitic steel (Grade 91)—to optimize the process parameters for the full 3D prints. The optimization led to the selection of 20 different powder processing conditions—10 for each class of alloys.

D9 and AFA alloys showed extensive cracking and porosity in the samples. This cracking was because of the less-than-ideal conditions present in the chamber during the deposition. A709 printed using the same process parameters showed almost fully dense samples with no noticeable porosity or any other defects. Scanning electron microscopy and electron backscatter diffraction analysis revealed single-phase face-centered cubic microstructure with cellular structure within the grains.

HT9, Grade 91, and Grade 92 alloys also showed no noticeable signs of cracking, and ImageJ analysis showed porosity <0.5% in all conditions. Although Grade 91 and Grade 92 showed single-phase body-centered cubic microstructures, the presence of martensite laths was noted in the HT9 alloy.

All these results were used to provide the AMMT leadership team with clear recommendations on the downselection of reactor materials, as well as establish a road map for the characterization and qualification of these nickel- and iron-based alloys that were selected.

1. INTRODUCTION

Additive manufacturing (AM) allows for the fabrication of complex near net shape components, reducing the needs for machining, welding, and brazing [1]. Recent studies predict that the large adoption of AM will drastically affect the supply chain and global economy across multiple commercial sectors [2]. For the nuclear industry, the Transformational Challenge Reactor (TCR) Program demonstrated that AM combined with artificial intelligence can deliver enabling technologies for advanced reactors [3]. Digital manufacturing is of particular relevance, using the tremendous amount of information generated during printing to accelerate part qualification through analysis by advanced data analytics techniques [4–6]. Three programs across the US Department of Energy (DOE) Office of Nuclear Energy were therefore combined in FY 2022 to create the Advanced Materials and Manufacturing Technologies (AMMT) Program, aiming at developing advanced materials and processes for current and advanced nuclear technologies. As stated in the AMMT Program road map [7], a key goal of the program is the faster incorporation of new materials and manufacturing technologies into complex products and systems that support a broad range of advanced nuclear reactor technologies.

Although the core efforts of the AMMT Program aim to demonstrate the potential of AM using stainless steel (SS) 316H, many other structural materials may be relevant to the program. Thus, four "Prioritization of Current Reactor Materials for Advanced Manufacturing" work packages at Oak Ridge National Laboratory (ORNL), Idaho National Laboratory (INL), Pacific Northwest National Laboratory (PNNL) and Argonne National Laboratory (ANL) aim to identify materials of interest to a broad range of advanced nuclear reactors and determine their suitability for use with AM laser powder bed fusion (LPBF). This effort is a continuation of the work initiated at PNNL with the publication of a materials scorecards report ranking several relevant structural NE materials [8]. Because of the large number of alloys of interest, ORNL and INL focused on nickel-based alloys, and ANL and PNNL investigated iron-based alloys; INL and PNNL looked at other alloys, which refers to non-steel and non-nickel-based alloys. A key goal for the four laboratories was to establish a decision criteria matrix for a fair and consistent assessment of several potential structural candidate materials. The selection process is based on potential effects to the nuclear industry, material processability via AM technologies, and improved performance. The core results presented in this report have been published in reports from each partnering laboratory, and the main goal of the report is to provide a comprehensive document including detailed recommendations on a few high-potential alloys to be integrated under the AMMT Program.

2. DECISION CRITERIA MATRIX

The determination of relevant criteria for the selection of reactor materials to be produced by AM for NE applications is needed to ensure a consistent and transparent decision process. Material scorecards were developed and reported by PNNL for the following nuclear-relevant materials, with detailed justifications of the proposed readiness levels: 316 SS, 304 SS, Alloy 800H, Graphite C/C, Hastelloy N, SiC, HT9, Alloy 617, and Alloy 718 [8]. The scorecards were based on published literature data, industry response to a survey, stakeholder input collected at workshops, and expert opinions. Six key categories were considered when evaluating each material: code availability, gaps in data availability for performance values and measurements, technical maturity for end use/development stage, deployment readiness requirements, supply chain availability, and programmatic factors. Although significant variability in data and knowledge gaps were recognized, 316 SS and 304 SS obtained the highest ranking, being the most common SSs in the nuclear industry, and a variant of 316 SS with higher carbon content, 316H, became the focus of the AMMT Program. To refine the approach and take advantage of the broad expertise at the four participating national laboratories, recurrent meetings were organized to discuss, select, and rank a broad range of relevant criteria for reactor materials selection. The current decision criteria matrix is shown in Table 1 with six key categories and 34 individual alloy criteria. The initial matrix was presented at several review meetings and at an industrial workshop at ORNL and was modified based on participants' feedback. This matrix is expected to evolve with time based on constant feedback from main stakeholders. The definition and relevance of each individual criterion will be provided in the final collaborative report, and information on each category of the decision criteria matrix is provided in this report.

Table 1. Decision criteria matrix that will guide the selection of materials to be evaluated under the AMMT Program

Category	Criteria and corresponding ranking					
Manufacturing/ powder	Powder availability: 4	Powder properties: 2	Powder chemistry: 3	Cost: 3	Recycling: 2	—
Manufacturing/ components	Printability (LPBF): 5	Defects: 3	Post-treatment: 3	Processing window: 4	Weldability: 3	Surface roughness or finish: 2
History and applications	NE experience: 4	Other industry experience: 3	Data availability: 4	Code data availability: 3	Experience with non-LPBF AM: 2	Scaling up: 3
Mechanical properties	Creep: 4	Fatigue: 4	Creep-fatigue: 4	High-temperature tensile strength: 3	Room temperature: 2	—
Environmental effects	Radiation resistance: 4	Oxidation resistance: 2	Stress corrosion cracking: 4	Molten salt: 3	Liquid metal: 3	—
Physical properties	Thermal properties: 2	Solidification-relevant properties: 2	Other modeling-relevant properties: 2	Nondestructive examination–relevant properties: 2	—	—
Microstructure	Material homogeneity: 3	Microstructure stability: 4	LPBF microstructure specificity: 3	—	—	—

2.1 MANUFACTURING/POWDER

2.1.1 Powder Availability

In comparison with commercially available wrought or cast alloys, only a few commercial powders are readily available. When custom-made powders are needed, minimum quantities might be requested from the powder manufacturer, and powder production will require several months. Similar concerns will affect other AM feedstocks, such as wires. This long time will have an effect on potential customer decisions, and many industrial partners expressed concerns related to the AM supply chain. Powder procurement issues might also complicate research to be conducted under the AMMT Program.

2.1.2 Powder Quality

The quality of the feedstock that is used in the AM process is key to the quality of the final part. The size, shape, surface morphology, composition, and amount of internal porosity are the main factors to be considered. The flowability and apparent density, which play a critical role in the printing process, are dependent on the quality of the powder, which is directly related to the production technique. The main techniques employed are rotary atomization, plasma atomization, gas atomization, and the plasma rotating electrode process (PREP). Each technique has its own benefits and shortcomings. Gas atomization and rotary can lead to irregular shapes or gas entrapment, but plasma and PREP do not have these issues. The gas entrapment leads to powder-induced porosity, which is very detrimental to the parts. This issue is offset by the cost of the powders produced by plasma atomization and PREP. Currently, the most-preferred way of powder production is PREP because it has been known to reduce powder-induced porosity.

2.1.3 Powder Chemistry

Another very important factor to consider is the powder chemistry/composition. The final chemistry of the parts is dependent on the initial powder composition. Impurities such as oxygen are, however, easily picked up either during the atomization process or, depending on the powder composition, in storage. The loss of metals to vaporization must also be accounted for (e.g., Mn). Although most of the work on LPBF is done using prealloyed powders, literature has been reported on using mixtures (i.e., using elemental powders and blending them). This process might lead to inhomogeneity in the final composition of the parts. The effect of interstitial elements such as oxygen and nitrogen also needs to be considered, especially when printing reactive materials such as titanium or aluminum-based alloys. Interstitial elements can also influence the melting kinetics of powder. Another crucial factor to consider is the optimization of powder chemistry specific to manufacturing techniques. Although conventional processes have specifications for alloy chemistry, because of the different thermokinetics involved in the AM processes, it might be ideal to tailor composition to the manufacturing process.

2.1.4 Powder Cost

Because AM is still in infancy in terms of widespread usage, the raw material needed to fabricate the parts is still very expensive. Depending on the alloy composition, the process used to make the powder (type of atomization), the source of the powders, and the overall cost of the powders, all can be very high. Although some of the alloys such as 316L, Ti-64, and IN-718 can be inexpensive owing to them being the most studied and produced alloys, any compositional variation leads to a tremendous increase in the cost. The lead time associated with the powder manufacturing/delivery also increases the cost.

2.1.5 Powder Recycling

For powder bed fusion processes to be viable, recycling of the powders is an important factor in terms of keeping the overall costs down. The recycling of powders could lead to other issues. The two main concerns would be the change in the composition (because of the evaporation) and oxygen pickup. Alloys containing elements with higher vapor pressure evaporate more easily, and this evaporation would change the composition of the alloy when reused. Oxygen intake is a bigger issue for reactive materials (i.e., Ti and Al alloys). Other factors influence both of these issues: the atmosphere in which the parts are built, the temperature (elevated temperatures cause more oxygen ingress and also effect evaporation), the process used to make the powders, and more. A way to counter some of these issues could be to use a mix of virgin and recycled powder. All four criteria mentioned here involving powders are interconnected.

2.2 MANUFACTURING/COMPONENTS

2.2.1 Printability (Laser Powder Bed Fusion)

The high susceptibility to defects and microstructure inconsistencies during the LPBF process poses a significant challenge to obtain optimal processing parameters for an alloy that was not previously investigated. Thus, requirements exist for efficient printability frameworks to effectively determine the processing parameter window of a given alloy considered as a potential feedstock for LPBF. An ideal framework integrates experiments, physics-based simulation, uncertainty analysis, and fabrication and characterization to determine the bounding region in the manufacturing space, resulting in near-full-density, defect-free parts.

2.2.2 Defects

The defects in LPBF-fabricated products can affect the creep and creep-fatigue properties, and these properties can be lower than those of wrought counterparts because of the critical role preexisting pores have on determining the mechanical properties.

2.2.3 Post-Treatment

The postprocessing heat treatment can promote the homogenization of the microstructure to redistribute residual stresses that are inherent in LPBF-fabricated components. The heat treatment can also improve the ductility of the as-built component to make it comparable with that of fully annealed wrought materials. The microstructural anisotropy is also reduced with post heat treatments.

2.2.4 Processing Window

The process window for highly efficient LPBF, ensuring the production of parts with low porosity, is a critical criterion for fabrication. The processing window comprises laser powers, laser beam diameters, and velocities of the moving laser beam. Beyond the suitable window for these parameters, the process can produce detrimental results such as key-holing, balling-up, and lack of fusion in the material.

2.2.5 Weldability

To use the LPBF technique as a commercial production process, joining small parts to build large sizes is essential. Because the LPBF can produce textured grains, the strength of the welds depends on the welding direction. The extent of cracking is usually observed to be smaller in samples welded parallel to the elongated grain orientation than in samples where the welding is performed perpendicular to it.

2.2.6 Surface Roughness/Finish

Fatigue cracks tend to initiate at the surface, making fatigue and creep-fatigue responses very sensitive to surface roughness. A rough surface finish can detrimentally affect the mechanical performance of LPBF components, particularly the fatigue and creep-fatigue properties. A substantial improvement in fatigue performance can be achieved through the minimization of surface roughness via machining. A high-frequency mechanical impact as postprocessing has been reported to improve uniaxial strength and high-cycle fatigue performance.

2.3 HISTORY AND APPLICATIONS

2.3.1 Nuclear Energy Experience

Previous experience on AM components for nuclear applications is of great relevance to the AMMT Program. This experience includes the fabrication of unique, complex components and the generation of a materials database. Relevant experience also includes the development of methodologies to accelerate the adoption of AM by the NE industry, such as the TCR digital manufacturing approach.

2.3.2 Other Industries Experience

Several industries have invested heavily in AM over the past few years. This investment is particularly true for the aerospace and gas turbine sectors, and companies such as General Electric (GE) and Siemens have developed activities dedicated to AM. Of particular interest is the fabrication of complex components potentially relevant to the NE industry such as valves, heat exchangers, and more, as well as approaches to rapidly design quality materials and components.

2.3.3 Data Availability

Another important criterion for the selection of materials to be integrated into the AMMT Program is current data availability. For the present context, the database should be focused only on additively manufactured alloys. Having a larger database of published data relevant to nuclear applications would merit a higher ranking in the matrix compared with alloys that have no published literature. As such, an alloy such as 316L, which has been extensively studied, would have a higher ranking in the matrix compared with an alloy such as Grade 92.

2.3.4 Code Data Availability

Code data availability refers to the data specifically approved by the American Society of Mechanical Engineers (ASME) for nuclear reactor applications. Currently, only six alloys are approved for structural applications. These alloys would have a higher rating in the decision criteria matrix. For example, the ranking for 316 SS would be higher than Alloy 625 even though they both have extensive AM literature; 316 SS is ASME code–qualified, whereas Alloy 625 is not. The other factor to consider is the available literature on AM (which ties in with the data availability). Even though both 316 SS and 9Cr–1Mo are both code-qualified and have code data availability in wrought form, the former would rank higher because of the current work on developing an ASTM International's standard for AM 316 SS.

2.3.5 Experience with Non–Laser Powder Bed Fusion Additive Manufacturing

Although the current work package focuses mainly on LPBF process, the usage of different manufacturing techniques is also important in terms of understanding and ranking the material. Other

manufacturing techniques include directed energy deposition (DED), electron powder bed fusion, wire-based DED methods, solid-state processing, and more.

2.3.6 Scaling Up

One of the ways to increase production rates in the LPBF process is to use multiple lasers to parallelize the process. The production rates can also be increased by maximizing the build rates of each individual laser. Increasing the layer thickness of the process can also increase the build rates for scaling up the process.

2.4 MECHANICAL PROPERTIES

2.4.1 Creep

Long-term exposure at high temperatures under constant stress will result in the evolution and degradation of the microstructure, leading eventually to component failures. Creep testing (ASTM E139 [9]) is a major element of material qualification requiring >500,000 h cumulative testing, with the duration of some of the tests exceeding 30,000 h. Creep is a major property to consider when selecting materials for NE structural applications because the component lifetime will be directly related to the alloy creep performance. The development of accurate lifetime creep models to reduce the need for long-term creep testing is key to the AMMT rapid qualification approach.

2.4.2 Fatigue

Vibrations and thermal gradients, particularly during start-up and shutdown, can induce cyclic loading on components. Fatigue testing (ASTM E606 [10], ASTM E466 [11]) is used to understand the detrimental effects of these load/strain cycles on components and to determine the risk of failure. When considering fatigue life, the controlling variables are the temperature of the testing, load ranges, and load ratios, along with the given total strain range and strain ratio (maximum strain/minimum strain) for testing performed to E606 or, alternatively, if the load-controlled process is used (following ASTM E466 [11]).

2.4.3 Creep-Fatigue

Creep and fatigue damage processes can interact in a synergistic way that leads to failure significantly earlier than would be expected when considering the individual damages from each of these processes. Creep-fatigue testing (ASTM E2714 [12]) is used to determine the degree of this interaction. Cyclic tests are performed with holds at the maximum strain and/or the minimum strain. The amount of damage from the cyclic load and the amount of damage from creep during the strain holds are determined, and the two values are typically plotted against each other in the form of a damage interaction diagram (sometimes referred to as a *D-diagram*). This interaction cannot be determined solely by creep and fatigue testing separately and is less-often considered. Optimization of material creep and fatigue properties often requires opposite microstructure features (e.g., grain size), highlighting the need for creep-fatigue experiments.

2.4.4 Room-Temperature Tensile Strength

Room-temperature tensile strength (TS), including yield strength (YS), ultimate TS, and total ductility, are determined through tensile tests as described in ASTM E8/E8M. These properties are the basic mechanical strength of the material.

2.4.5 High-Temperature Tensile Strength

High-temperature tensile properties, determined through tensile testing as outlined in ASTM E21 [14], are used to determine tensile properties as outlined in the room-temperature tensile testing. These properties change with increasing temperature.

2.5 ENVIRONMENTAL EFFECTS

2.5.1 Radiation Resistance

Material that will be near the core will see neutron damage. For structural materials, this damage often causes displacements of atoms from their lattice locations. Radiation resistance refers to the material's ability to resist changes in properties under radiation. This ability can be a result of locations (e.g., grain boundaries, precipitates) that act as sinks for radiation damage or compositions that have lower neutron cross sections. Because of their specific and often refined microstructure, alloys fabricated by AM may have radiation resistance differing from wrought counterparts.

2.5.2 Oxidation Resistance

Oxidation resistance is a key property for structural alloys because component lifetime can be directly affected by the alloy oxidation rates and resulting metal loss. The alloy oxidation behavior is of particular significance for high-temperature, gas-cooled reactors because impurities in flowing helium can result in significant oxidation (and carburization). Although oxidation may not be the limiting factor for liquid metal and molten salt reactors (MSRs), it may affect alloy selection. For example, the low chromium concentration in molten salt–compatible, nickel-based alloys such as Hastelloy N will hinder the formation of a protective Cr_2O_3 scale during oxidation at high temperatures.

2.5.3 Stress Corrosion Cracking

The resistance to stress corrosion cracking (SCC) is a critical parameter for many structural nuclear components. Corrosion rates might be affected by the applied stress and crack initiation, and propagation can be affected by corrosion products, as well as microstructure evolution because of corrosion. SCC is a major concern for current light-water reactors but might also be critical for any reactor exposed simultaneously to stress and a corrosive environment.

2.5.4 Molten Salt Compatibility

For MSR concepts, material compatibility is a major limiting factor and will drastically affect the reactor operating temperature. Both fluoride and chloride salts are currently being considered, and control of the salt impurities will reduce corrosion rates. Formation of a stable, protective, chromium-rich scale is not possible in molten salt environments, and the best-performing alloys have low chromium concentrations to avoid rapid chromium depletion at the alloy surface. Although capsule tests can provide information on alloy compatibility, flowing loops are required to capture the dissolution and reprecipitation taking place at high and low temperatures, respectively.

2.5.5 Liquid Metal Compatibility

Liquid metal compatibility is critical to sodium-cooled or lead-cooled concept reactors. As for molten salt testing, capsule tests can help with material selection, but flowing systems are required to assess the effect of material dissolution in the hot zone and reprecipitation in the cold zone.

2.6 PHYSICAL PROPERTIES

2.6.1 Thermal Properties

Thermal properties are the key factors of an alloy that determine how it behaves under different temperatures, such as close to its melting point. It also determines thermal conductivity and the coefficient of thermal expansion. These properties can affect the dimensional stability, printability, and performance of 3D printed materials. Thermal properties can be measured using differential scanning calorimetry, thermogravimetric analysis, laser flash analysis.

2.6.2 Solidification-Relevant Properties

The powder melting and solidification in the LPBF process is an important key aspect because it controls the size, shape, and distribution of the grains, the growth morphology, the elemental segregation, and precipitation. Because of localized, rapid heating and cooling during the LPBF process, the solidification is linked with multiphysics (such as fluid flow and diffusion of heat and mass) and multiscale (lengths, times, and temperature ranges) challenges.

2.6.3 Other Modeling-Relevant Properties

The aim of this category was to capture any relevant properties that are needed for the modeling of AM processes and resulting microstructures. Properties such as viscosity or surface tension of the molten metal at different temperatures might, for example, be needed for the simulations of solidification microstructure during LPBF. In addition to experimental data, simulation validation based on these data is of great interest.

2.6.4 Nondestructive Examination–Relevant Properties

Nondestructive analysis is of particular significance for the AMMT Program because nondestructive examination (NDE) data are needed for the validation of in situ data at the center of the AMMT digital manufacturing approach. The relevant properties are specific to the NDE technique under consideration. For example, the AMMT Program relies heavily on computerized tomography (CT) scans, and the alloy density is the main property affecting the CT scan resolution.

2.7 MICROSTRUCTURE

2.7.1 Material Homogeneity

Material homogeneity is an important factor for structural components to ensure that minimum required properties are met. Qualification of wrought or cast materials will require testing of several (at least three) batches to ensure that the measured properties are not drastically affected by the fabrication process. LPBF processing typically results in inhomogeneous, as-printed materials, with defects inhomogeneously distributed and chemical segregations occurring because of rapid cooling. The latter is directly related to the powder chemistry and processing conditions, and an AMMT work package is currently evaluating the effect of material heterogeneity on material properties. Notably, the AMMT digital manufacturing approach aims to predict defects distribution, which might allow for the qualification of inhomogeneous LPBF materials.

2.7.2 Microstructure Stability

In service, microstructure evolution is a major concern for structure components because it will affect the component properties and is directly linked to component failures. This failure link is especially true for LPBF alloys because the rapid cooling during printing results in far-from-equilibrium microstructure. The disappearance of specific microstructural features such as the as printed cellular structure and coarsening of fine strengthening precipitates is expected at high temperatures. Stabilization of the microstructure via specific heat treatments might be considered for some applications.

2.7.3 Laser Powder Bed Fusion Microstructure Specificity

Most alloys that have been considered for the fabrication of AM components are well-known wrought or cast alloys. Only six of these alloys are currently code-qualified for NE structural applications, which make them potential candidate alloys for the AMMT Program. Because of the very specific microstructure of LPBF alloys, the availability of code data might not accelerate the qualification of the LPBF version of the alloy. One potential solution is to carry out a heat treatment that will result in a microstructure similar to the microstructure of wrought alloy. For example, high-temperature recrystallization treatments can significantly reduce the microstructure anisotropy with respect to the build direction (BD). Alternatively, considering only the six code-qualified alloys drastically limits the range of potential alloys and applications to be evaluated under the AMMT Program.

3. EVALUATION OF NICKEL-BASED ALLOYS

Nickel-based alloys are of interest to a wide range of advanced reactor designs because of their good high-temperature strength and general corrosion resistance. Several extensive reviews of nickel-based alloys in use or considered for nuclear applications have already been published [15–18]. There are concerns, however, that need to be evaluated with respect to the nickel-based alloys' printability. LPBF is essentially a laser-based welding process, and most nickel-based alloys are highly susceptible to cracking during welding, including solidification cracking, hot tearing, grain boundary liquation cracking, and strain age cracking. The key reasons are the nickel-based alloy's wide solidification ranges and high concentrations of segregating and precipitating elements [19, 20]. LPBF parameters such as scan speed, laser power, and scan path must, therefore, be carefully selected to minimize porosity and cracking defects [21,22]. The previous PNNL materials scorecards report focused on four nickel-based alloys well-known to the nuclear community: 800H, 718, 617, and Alloy N. This report is evaluating a broader range of nickel-based alloys. Three categories of nickel-based alloys were identified in this report as potentially of interest to advanced reactor designs:

- Alloys with low amounts of cobalt
- Alloys with high-temperature strength
- Alloys with good compatibility with molten salts

All nickel-based alloys tend to have good high-temperature mechanical properties; however, some, such as Alloys 230, 233, 740H, 282, and 617, are particularly optimized for their high-temperature strength. This strength often comes with the inclusion of alloying elements to create strengthening phases, typically γ' or carbides. Some of those alloying elements, such as cobalt, are not desirable in applications where they will experience neutron irradiation, so a separate class with low cobalt concentrations was considered. These alloys, such as Alloys 718, 625, and 800H, tend not to have as good of a high-temperature strength but are more suitable for applications that will receive irradiation. Notably, nickel in general has concerns with irradiation and helium generation, so there will always be some restrictions on the irradiation application of these alloys. Finally, molten salt, particularly of interest to the molten salt–

cooled reactor designs but also of interest for thermal transport or storage in some other reactor designs, can cause significant corrosion in materials. Nickel-based alloys, particularly Hastelloy N and Alloy 244, tend to resist molten salt corrosion because of low chromium concentrations and are likely to see applications in this environment.

Within the nickel-based alloy family, some alloys are more easily printable than others. A given alloy's printability generally depends on its solidification range, γ′ fraction, phase fraction of topographically close-packed phases, and impurity concentrations [20, 23, 24]. Figure 1 [20] shows the strain age cracking propensity plotted against the γ′ volume fraction, with several of the alloys of interest shown in the figure. The two factors appear to be linearly related. The alloys of interest for this report are all in the low–strain age cracking area because of a relatively low γ′ volume fraction. The main alloys of interest will be discussed individually in the following sections, and their nominal compositions are shown in Table 2

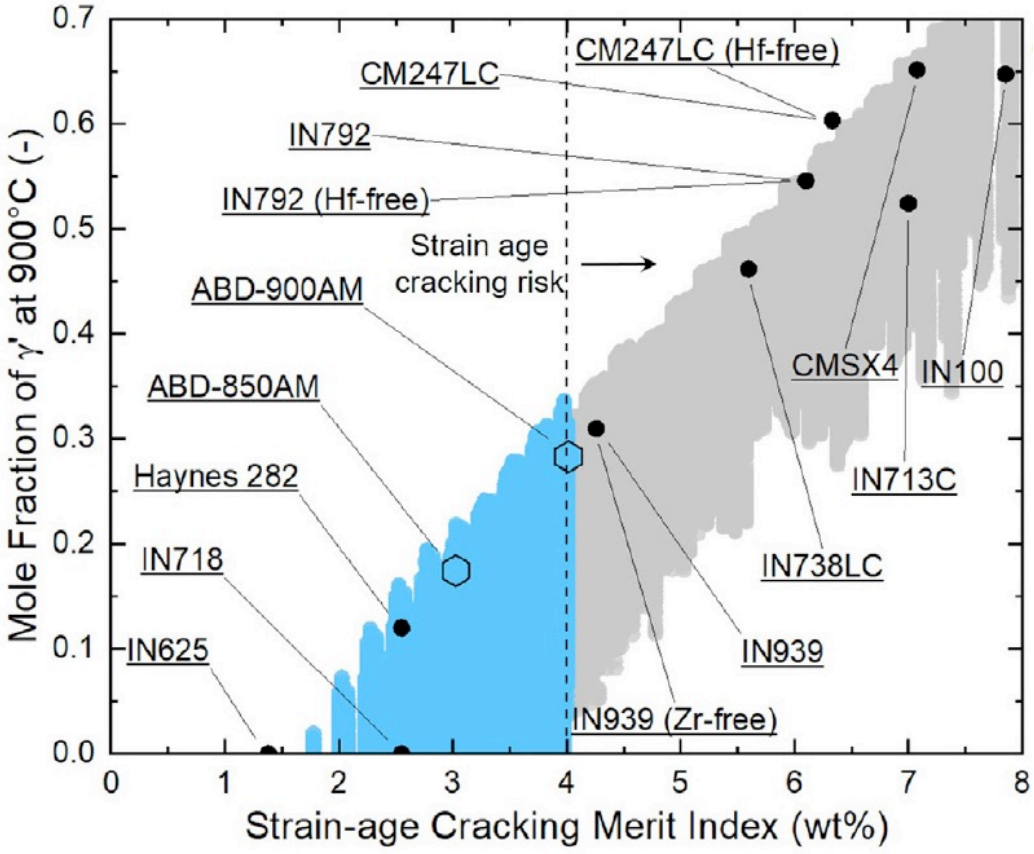

Figure 1. Relationship between γ′ fraction and strain–age crack merit index [20].

Table 2. Nominal compositions of alloys of interest (wt %)

Alloy	718	625	800H	282	740H	617	230	233	GRX-810	Hastelloy N	244
Cr	19	22	21	20	24.5	22	22	19	29	8	8
Co	1<	<1	—	10	20	13	<5	19	33	—	—
Mo	1<	9	—	8.5	0.1	9	2	7.5	—	22.5	22.5
Ti	0.9	<.4	0.4	2.1	1.35	<0.6	<0.1	0.5	0.25	—	—
Al	0.5	<.4	0.4	1.5	1.35	1	<0.3	3.3	0.3	<0.5	<0.5
Fe	Bal.	<5	<39.5	<1.5	—	<3	—	<1.5	—	<2	<2
Mn	<0.35	<.5	—	<0.3	—	<1	0.5	<0.4	—	<0.8	<0.8
Si	<0.35	<.5	—	<0.15	0.15	<1	0.4	<0.2	—	—	—
C	<0.08	0.05	0.075	0.06	0.03	0.1	0.1	0.1	0.05	<0.03	<0.03
B	—	—	—	0.005	—	<0.006	<0.015	0.004	—	—	—
Ta	—	1	—	—	—	—	—	0.5	—	—	—
Nb	—	3	—	—	1.5	—	—	—	0.75	—	—
W	—	—	—	—	—	—	—	<0.3	3	6	6
P	<0.015	<.015	—	—	—	—	—	—	—	—	—
S	<0.015	—	—	—	—	<.015	—	—	—	—	—
Cu	<0.3	—	—	—	—	<0.5	—	—	—	—	—
Y	—	—	—	—	—	—	—	<0.025	—	—	—
Zr/La	—	—	—	—	—	—	0.02La	0.03 Zr	—	—	—
Re	—	—	—	—	—	—	—	—	1.5	—	—
Y_2O_3	—	—	—	—	—	—	—	—	yes	—	—
Ni	52.5	Bal.	32.5	Bal.	Bal.	Bal.	Bal.	Bal.	Bal.	Bal.	Bal.

Bal.: balanced

3.1 LOW-COBALT NICKEL-BASED ALLOYS

Low-cobalt nickel-based alloys can be considered for components closer to the core outlet, experiencing significant neutron fluxes. The three key alloys to be evaluated in this category are Alloys 718, 625, and 800H.

3.1.1 Alloy 718

3.1.1.1 Manufacturing, Applications, and History

Superalloy 718 is one of the most-used nickel-based superalloys with many applications for aircraft and land-based gas turbine engines [25]. The exceptional strength of the alloy at temperatures up to approximately 700°C is due to the presence of strengthening nano size γ′ and γ″ precipitates. While developing the nickel-based 625 alloy, special metals researchers observed a drastic improvement of the YS of nickel-based alloys because of the addition of niobium and molybdenum, which led to the discovery of Alloy 718 [26]. Alloy 718 is currently used in boiling water reactor, pressurized water reactor, advanced reactor designs such as the gas-cooled fast reactor (GFR) and the very high-temperature reactor (VHTR) are looking into the potential use of Alloy 718 components for high-temperature applications [8,15]. As the *workhorse* alloy for the gas turbines and aerospace industries, companies such as Siemens Energy and GE have acquired extensive experience in fabricating 718 components by AM. As an indication of Siemens's involvement in the AM production of 718, Siemens and Senvol recently advertised a partnership to commercialize databases for three AM-produced alloys: nickel-based 718, nickel-based 625, and titanium-based Ti-64 [27]. A broad range of component demonstration projects involving AM 718 have been reported by GE, from a partnership with Shell to produce an oxygen hydrogen micromixer [28] to the large-scale fabrication of an advanced additive integrated turbine centre

frame 718 casing [29]. On the nuclear side, Inconel 718 was a candidate alloy under the TCR program for several structural elements below the reactor core [30].

Such an interest in AM 718 components has led to the development of a reliable supply chain, with 718 powder being commercially available from many powder manufacturers, including Praxair, Carpenter, Oerlikon, Powder Alloy Corporation (PAC), and more. It is worth noting that, on the Praxair powder website, only two powders have dedicated powder datasheets: nickel-based 718 and nickel-based 625 [31]. Carpenter Additive highlights only three nickel-based alloys on its website: Alloy 718, Alloy 625, and Hastelloy X [32]. Requirements for the 718 powder manufacturing, thermal processing, microstructure, properties, and more, are covered by the ASTM F3055-14a, *Standard Specification for Additive Manufacturing Nickel Alloy (UNS N07718) with Powder Bed Fusion*.

3.1.1.2 Microstructure, Mechanical Properties, and Environmental Effects

In addition to the substantial experience from industry, extensive literature has been published on AM 718. In their review article on AM nickel-based alloys in 2021, Sanchez et al. estimated that 192 studies out of 290 were focused on Alloy 718 (68%) [33]. As previously mentioned, hot cracking is often considered the main challenge for the printing of nickel-based superalloys and is directly related to the γ' volume fraction and, thus, the aluminum and titanium concentration [20, 34]. With its very low aluminum and titanium contents, Alloy 718 is considered a printable superalloy, with the only potential defect being porosity, which can be minimized, and a density superior to 99.9% in the as-printed conditions is achievable [35]. Tensile data generated at room and high temperatures on as-printed LPBF 718 showed variations of properties based on the specimen orientation, with higher strength but lower ductility perpendicular to the BD. Columnar grains along the BD with a cellular structure or fine dendrites have been reported for the as-printed material, explaining the observed anisotropic tensile behavior for the as-printed LPBF 718. Additionally, the presence of laves and δ phases in the as-printed conditions have a deleterious effect on the alloy's tensile properties [36–38]. Many authors have, therefore, studied the effect of heat treatments and/or hot isostatic pressing (HIP) on the alloy microstructure and performance [37–43]. As expected, the microstructure and, in particular, the volume fraction of the δ phase is strongly affected by the solution annealing temperature [43], but Taller and Austin [40] showed that tensile properties at 20°C–600°C are superior or similar to the properties of wrought 718 and can be achieved after the following HT2 heat treatment: homogenization at 1,174°C for 2 h and 1,204°C for 6 h, solution anneal at 1,093°C for 1 h, and aging at 718°C and 621°C, both for 8 h. These excellent tensile properties were due to a recrystallized grain structure, high fraction of γ'' precipitates, and a low fraction of intragranular δ phase. In addition to tensile data, research teams studied the effect of the microstructure, surface finish, and heat treatment on the LPBF 718 fatigue performance [44, 45]. Komarasamy et al. [44] reported a number of cycles to failure similar to wrought 718, both in the as-printed and annealed conditions, and they concluded that the high-volume fraction of δ phase at grain boundaries did not significantly affect the alloy's fatigue behavior. Kevinsanny et al. performed fatigue testing on HIP and annealed LPBF 718 specimens, with or without surface polishing, and concluded that the rough surface of the AM specimen did not decrease the alloy fatigue performance owing to the presence of large equiaxed grains [45].

Moreover, Sanchez et al. performed creep testing at 650°C and 600 MPa on 718 material fabricated by LPBF using one or several lasers [46]. Specimens were then machined at 0°, 45°, and 90° with respect to the BD. All the specimens were heat-treated according to the AMS 5662 standard (i.e., 980°C, 1 h, gas quench; 720°C, 8 h, furnace cooling; to 620°C, 8 h, gas quench). They observed longer lifetimes for the specimens machined along the BD, with the multilaser strategy resulting in lifetimes similar to the lifetimes measured for wrought 718. All the specimens exhibited, however, a very low ductility at rupture, again with superior results along the BD, with a deformation at a rupture of approximately 7% but still significantly lower than the 29% average strain measured for the wrought 718 creep specimens. It

is, however, worth noting that a deformation of approximately 30% for wrought 718 is quite high and might not be representative of a fully heat-treated wrought 718 [47]. Brinkman et al. analyzed creep data from several 718 heats and showed that the ductility decreases with the increase of the creep lifetime [48].

Kuo et al. [49] studied the effect of BD and heat treatment on the creep properties of direct metal laser sintering and observed better performance along the BD. However, in all cases, very low creep lifetime and elongation at rupture were observed for the AM material in comparison with wrought 718 (strain at rupture of 7%). They concluded that the inferior AM creep properties were due to δ precipitates in the interdendritic region and the presence of a cellular structure with high dislocation density. The amount of δ phase decreased with increasing the solution anneal temperature, with nearly complete disappearance of the δ phase at $T > 1{,}120$°C, but increasing the temperature also resulted in grain growth and carbide formation at grain boundaries [50]. HIP improved the creep lifetime but did not enhance creep ductility at rupture, with all the AM specimens exhibiting less than 2% deformation at rupture. Wu et al. [51] conducted similar creep experiments at 650°C and 650 MPa after different heat treatments, and they drew the same conclusions (i.e., lower lifetime and ductility for the LPBF 718 compared with wrought 718). They attributed the lower creep lifetime in the as-printed condition to the presence of deleterious δ and Laves phases at grain boundaries, leading to grain boundary cavitation and cracking. Because of the elongated grain structure along the BD, this degradation mechanism also explains the lower lifetimes measured perpendicular to the BD.

Finally, it was reported in the PNNL materials scorecards report that no irradiation study has been published on the LPBF Alloy 718 [8], but Taller et al. recently submitted an AMMT milestone report on the evolution of LPBF 718 after irradiation at ORNL's High Flux Isotope Reactor (HFIR) [30]. The heat-treated LPBF 718 showed negligible differences to the YS and ultimate TS at both 300°C and 600°C with an irradiation of 2 dpa.

3.1.1.3 Alloy 718 Scorecard

In the PNNL materials scorecards report, Alloy 718 received a score of 4 for programmatic factors because of the use of the alloy in current reactors and the potential use in GFR and VHTR advanced reactors; a score of 3 was attributed to the alloy for supply chain availability. The 718 score cards based on the selection matrix criteria is presented in Table 3. Alloy 718 scored well in the powder and component manufacturing categories because high-quality 718 powder is routinely produced by several powder manufacturers, and complex components have already been produced for a broad range of applications. Knowledge of the LPBF 718 extends beyond the NE industry, with tremendous experience from the aerospace and gas turbines industries. This report focused on LPBF 718, but notably, Alloy 718 has been produced using a broad range of AM techniques, including electron-beam melting (EBM) [52]; DED [53]; wire-based, large-scale AM [54]; and binder jetting [55]. Code data availability is the limiting factor in the history and applications category, but overall, Alloy 718 scores were high. Mechanical properties data are already available—in particular, tensile data both at room and high temperatures—but published data on creep, fatigue, and creep-fatigue are limited. A significant amount of data have likely been generated by industry, but these results are not publicly available. Partnerships with key industrial partners such as Siemens or GE could give the AMMT Program access to these data. This current work described in detail in this report also shows that the AMMT Program could rapidly generate relevant data to further improve the LPBF 718 scorecard. The microstructure of the LPBF alloy has been extensively characterized in the as-printed conditions and after various heat treatments, but the long-term stability, with and without stress, needs to be studied further. This lack of availability is also the case for information related to environmental effects. Corrosion and/or stress corrosion data for the LPBF 718 alloy are currently missing, but the AMMT Program is in a good position to generate such data and compare the results with wrought 718. This task was accomplished in FY 2022 and FY 2023 on the irradiation side, with the generation of unique data at HFIR at 300°C and 600°C.

Finally, the physical properties required for microstructure prediction during printing (e.g., thermal properties, phase diagrams) are already available and have been used by several teams to correlate processing parameters with microstructure. The aerospace industry is also heavily invested in digital manufacturing, and Alloy 718 has been integrated in approach similar to (but not as advanced as) the AMMT approach using the Peregrine software.

Table 3. Scorecard for Alloy 718

Category	Criteria and corresponding ranking					
Manufacturing/ powder	Powder availability: 5	Powder properties: 4	Powder chemistry: 4	Cost: 3	Recycling: 3	—
Manufacturing/ components	Printability (LPBF): 4	Defects: 4	Post-treatment: 3	Processing window: 5	Weldability: 4	Surface roughness or finish: 3
History and applications	NE experience: 1	Other industry experience: 4	Data availability: 4	Code data availability: 0	Experience with non-LPBF AM: 4	Scaling up: 3
Mechanical properties	Creep: 4	Fatigue: 3	Creep-fatigue: ND	High-temperature tensile strength: 4	Room temperature: 5	—
Environmental effects	Radiation resistance: 3	Oxidation resistance: 3	Stress corrosion cracking: ND	Molten salt: ND	Liquid metal: ND	—
Physical properties	Thermal properties: 3	Solidification-relevant properties: 4	Other modeling-relevant properties: ND	CT-relevant properties: ND	—	—
Microstructure	Material homogeneity: 3	Microstructure stability: 4	LPBF microstructure specificity: 3	—	—	—
ND: not determined						

3.1.2 Inconel 625

3.1.2.1 Manufacturing, Applications, and History

Alloy 625 is a solution-strengthened alloy designed for high-temperature structural applications in corrosive environments, such as turbine components, chemical plant components, and nuclear power reactor core components [56]. Alloy 625 was found to be highly printable with a wide processing window by Wong et al. [57]. Similar to 718, 625 powder is widely available from many suppliers and often highlighted as a key powder product [31, 32].

3.1.2.2 Microstructure, Mechanical Properties, and Environmental Effects

Many studies of LPBF 625 focused on the microstructure and room-temperature tensile properties. Marchese et al. [58] reported the as-built room-temperature YS and ultimate TS in the transverse direction as 783 MPa and 1,041 MPa, respectively. Tian et al. [59] and Yadriotsev et al. [60] report similar values in the transverse direction. Yadriotsev et al. reported that the YS and TS in the BD is 800 MPa because of the anisotropic as-built microstructure, and the TS is similar to the transverse direction at 1,030 MPa.

Most authors did not report tensile properties in the BD. These values are stronger than the rolled and annealed wrought values reported in [19], which are approximately 530 MPa and 930 MPa, respectively.

Limited data exist for high-temperature properties of LPBF 625. Lee et al. [61] reported the high-temperature tensile properties at several temperatures and compared them with wrought values. They found that the as-built YS and TS of LPBF IN625 at 700°C were 520 and 743 MPa, respectively. The fully recrystallized microstructure had YS and TS values of 280 and 615 MPa, respectively, at 700°C. Both of these conditions were stronger than the wrought 625 material at 700°C, which had a YS and TS of 210 and 612 MPa, respectively. Kim et al. [62] reported tensile and fatigue data of HIP LPBF 625 at 650°C. They found that the YS and TS values were 246 and 637 MPa, respectively. The YS was similar to the wrought value, but the wrought TS was higher at 721 MPa. Despite undergoing HIP, the LPBF material still had worse fatigue performance than the wrought component in the high cycle fatigue region.

Son et al. [63] studied the creep behavior of LPBF IN625 at 650°C and 800°C. They found that the creep strength of LPBF 625 was the same or better (in the case of HIP parts) than wrought IN625 at a given strain rate. However, the creep ductility of LPBF parts was significantly inferior to wrought IN625.

A few authors investigated the oxidation resistance of LPBF 625. Ramenette et al. [64] found that as-built LPBF 625 had significantly worse oxidation resistance than wrought IN625 at 1,050°C because of the inherent segregation of molybdenum and niobium to boundaries during the LPBF synthesis. At 900°C, the oxidation resistance of LPBF 625 was only slightly worse than that of wrought IN625. Lewis et al. [65] found that heat treating LPBF 625 at 1,177°C to recrystallize it produced an oxidation resistance at 950°C that was almost as good as that of the wrought material.

Andurkar et al. and Keya et al. [66, 67] studied the irradiation response of wrought and LPBF 625 samples under fast neutron irradiation. They found that LPBF 625 exhibited less irradiation-induced hardening than wrought IN625. Andurkar et al. also found that the as-built BD samples underwent less irradiation-induced hardening than other orientations. Cieslik et al. [68] studied the irradiation response of LPBF and wrought IN625 under ion irradiation. Contrary to the results of Andurkar et al., they found that the LPBF material had a higher hardness change than the wrought material after ion irradiation.

3.1.2.3 Alloy 625 Scorecard

The score cards for alloy 625 is given in Table 4. A great similarity with the score card of 718 is evident because both of these alloys are critical to the aerospace industry. Both powders are commercially available from many powder manufacturers, and a broad range of components are routinely fabricated. The mechanical properties are overall better for 718, but notably, 625 could be considered for temperatures above 700°C, the temperature at which the mechanical properties of 718 will start to drastically decrease.

Table 4. Scorecard for Alloy 625

Category	Criteria and corresponding ranking					
Manufacturing/ powder	Powder availability: 5	Powder properties: 4	Powder chemistry: 4	Cost: 3	Recycling: ND	—
Manufacturing/ components	Printability (LPBF): 4	Defects: 4	Post-treatment: 3	Processing window: 5	Weldability: 4	Surface roughness or finish: 3
History and applications	NE experience: 0	Other industry experience: 3	Data availability: 3	Code data availability: 0	Experience with non-LPBF AM: 4	Scaling up: 2
Mechanical properties	Creep: 3	Fatigue: 2	Creep-fatigue: ND	High-temperature tensile strength: 3	Room temperature: 4	—
Environmental effects	Radiation resistance: ND	Oxidation resistance: 3	Stress corrosion cracking: ND	Molten salt: ND	Liquid metal: ND	—
Physical properties	Thermal properties: 3	Solidification-relevant properties: 4	Other modeling-relevant properties: ND	CT-relevant properties: ND	—	—
Microstructure	Material homogeneity: 3	Microstructure stability: 4	LPBF microstructure specificity: ND	—	—	—
ND: not determined						

3.1.3 Alloy 800H

Alloy 800H (Fe–[30–35]Ni–[19–23]Cr–[0.05–0.1]C) was discussed extensively in the PNNL materials scorecards report. A high programmatic factors score was given to the alloy because of its potential use in nuclear reactor designs such as MSRs and VHTR. It was, however, noted that very little is known of the alloy fabricated by AM, with only two papers by Yang et al. investigating the sensitization and stress corrosion cracking performance of LPBF 800H in the as-printed and annealed conditions [69, 70]. The report mentioned that 800H powder can be ordered from Carpenter Powder Products, but the company was contacted and has stopped producing the alloy. A powder quantity of approximately >500 lb would need to be ordered for Carpenter to consider producing the alloy. A detailed evaluation of the LPBF 800H will be provided in the next report, but the alloy readiness score will be low because of a lack of information on AM 800H and limited powder availability. The alloy 800H scorecard is given in the Appendix A, but the overall scores are considerably lower because of the lack of powder availability and published data.

3.2 HIGH-TEMPERATURE, HIGH-STRENGTH ALLOYS

These high-temperature alloys offer much more high-temperature capability compared with austenitic steels but cannot be considered for applications in the vicinity of the reactor core due to their high cobalt content. Although 617 is an obvious candidate alloy as the only nickel-based alloy code-qualified, other alloys of interest will be discussed—in particular, Haynes 282—because of their superior high-temperature performance.

Because most alloys studied do not have sufficient high-temperature mechanical property data for samples manufactured by LPBF, a comparison can be made using the published wrought properties.

Figure 2 shows the wrought stress–rupture data taken from the manufacturer brochures [56, 71–75] for several of the alloys studied. H233 does not have sufficient data to add to the figure. The figure shows that the precipitation-strengthened alloys IN740H, H282, and H244 have higher creep-rupture strengths than the 625 and 617 solution-strengthened alloys in the temperature range of 650°C–760°C. At 760°C, the γ″ precipitation in H244 apparently coarsens and/or dissolves, reducing its strength to the same level as IN625. At temperatures above 927°C, the γ′ precipitation in IN740H and H282 dissolves, reducing their strength levels to that of the solution-strengthened alloys. GRX-810 appears to have a higher creep-rupture strength than IN617 at high temperatures because of its oxide dispersion–strengthened (ODS) component.

A larger data set was used to generate the Larson–Miller plot displayed in Figure 3, comparing the creep performance of 718, 617, 282, 230, 244, and Hastelloy N alloys [71–72, 76–79]. Again, a significant improvement in creep performance is observed for Alloy 282 when compared with Alloy 617 for Larson–Miller parameter (LMP) values less than approximately 27,000, corresponding to temperatures lower than approximately 850°C. Alloy 230, another solution-strengthened alloy, exhibits similar properties as 617. Notably, Alloy 282 exhibits a similar behavior as Alloy 718 at high stresses and low temperatures, but at temperatures >700°C, γ′ precipitates in Alloy 282 are more stable than the γ″ in Alloy 718.

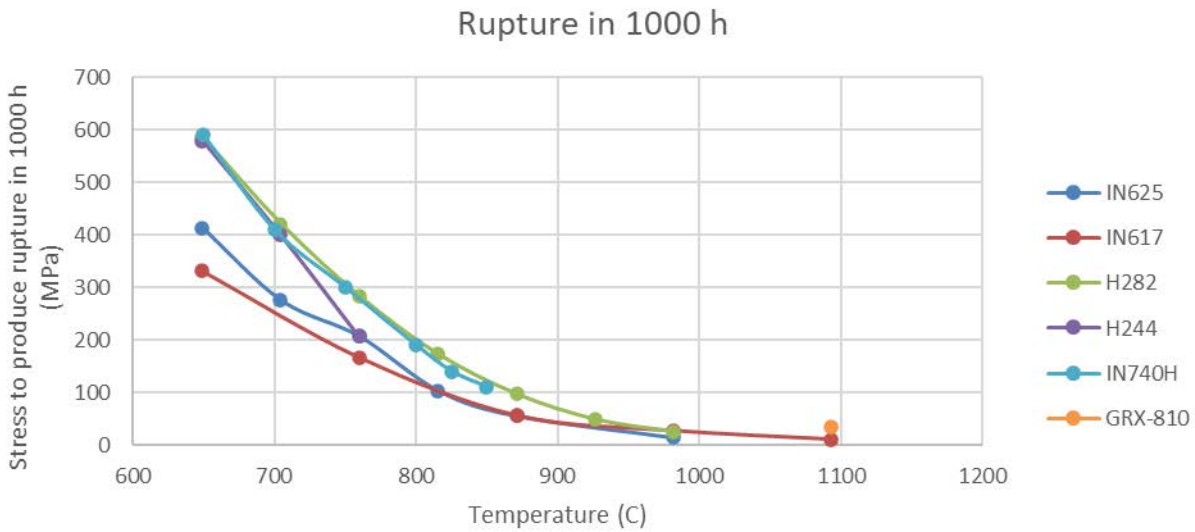

Figure 2. Creep stress–rupture data for alloys of interest. Data taken from [56, 71–75].

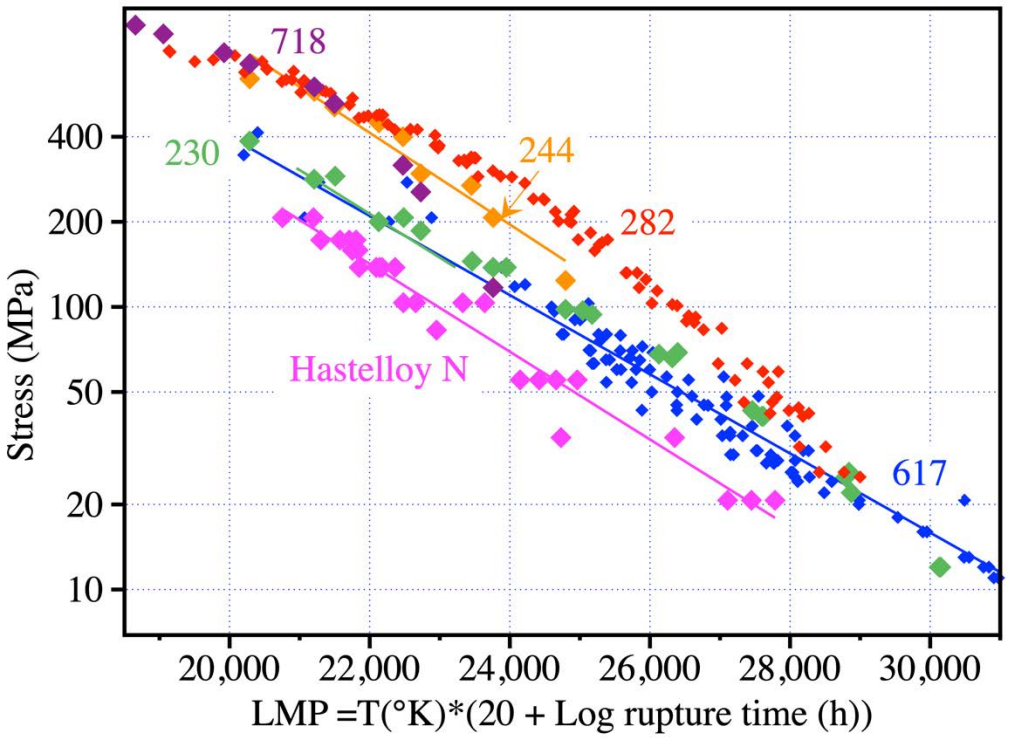

Figure 3. Comparison of the creep properties of Alloys 617, 282, 230, Hastelloy N, and 244 using an LMP plot.

Figure 4 shows a comparison of high-temperature YS data from both wrought alloys and the LPBF data that are available [56, 71–74, 80–82]. Again, the precipitation-strengthened alloys have higher strengths than the solution-strengthened alloys over most of the temperature range. At the highest temperatures, the YSs of all alloys are very similar. As stated previously, the high-temperature YS values of the alloys made by LPBF are very similar to or, in some cases, better than those of the wrought alloys.

Figure 5 [83] shows a comparison of the maximum allowable stress per the ASME *Boiler and Pressure Vessel Code* as a function of temperature for various wrought nickel-based alloys. The allowable stress follows the trends shown in Figure 2, Figure 3, andFigure 4, as expected.

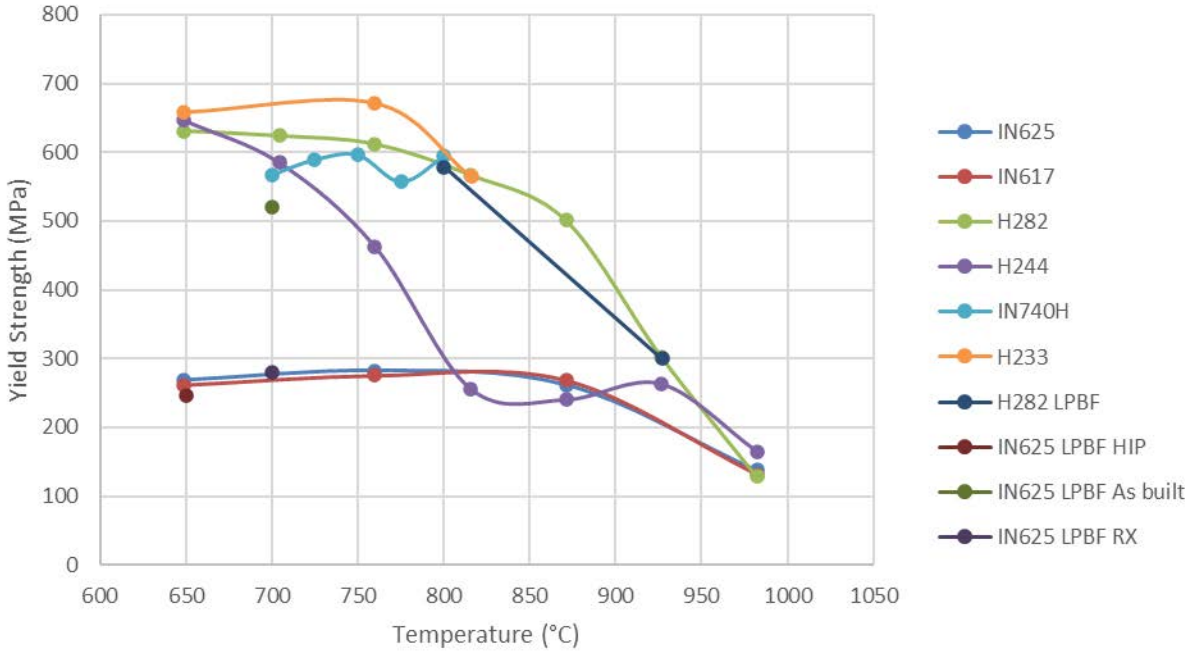

Figure 4. High-temperature YS of selected alloys. Data from [50, 65–68, 74–76].

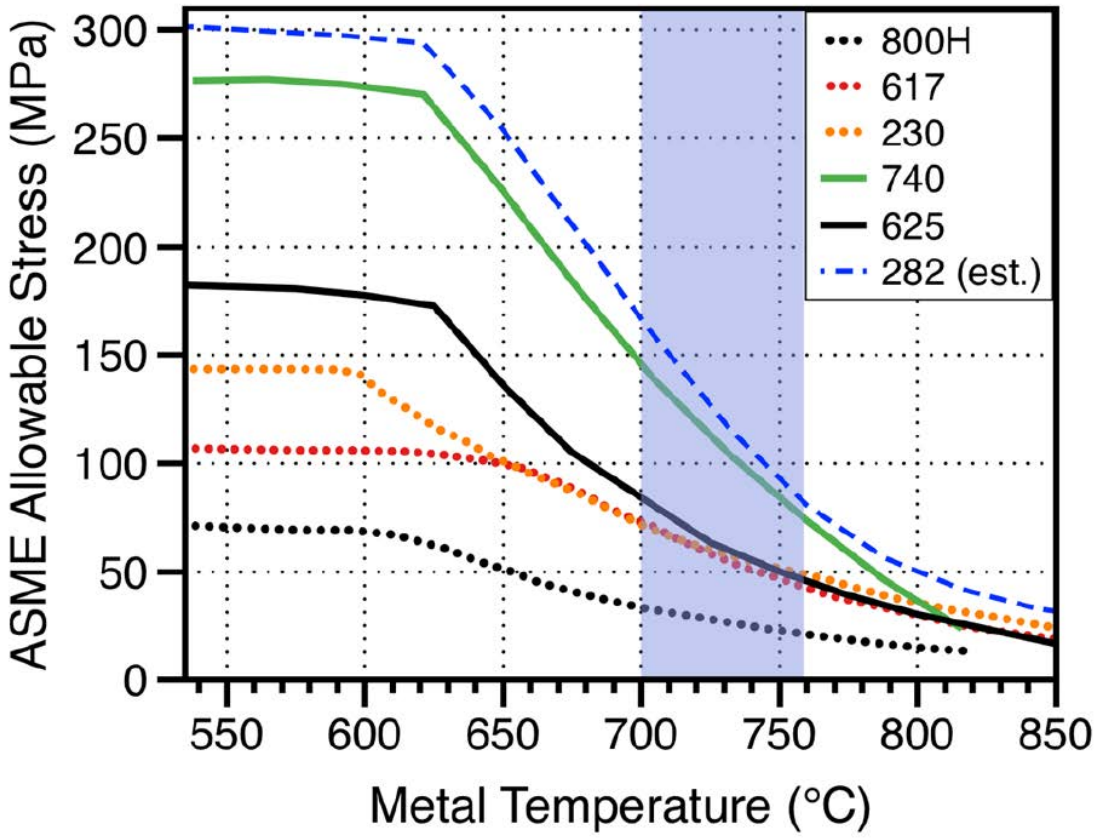

Figure 5. ASME-allowable stress as a function of temperature for various nickel-based alloys. Data from [83].

3.2.1 Alloy 282

3.2.1.1 Manufacturing, Applications, and History

Haynes 282 (Ni–20Cr–10Co–8.5Mo–2.1Ti–1.5Al) is a γ′-strengthened superalloy developed by Haynes International for high-temperature structural applications, especially for the aerospace and land-based gas turbines industries [84]. The 282 alloy was identified as a potential candidate for advanced ultra-supercritical components such as steam turbine disk (wrought) or turbine valve body (cast), which led to an extensive study of the alloy creep, fatigue, and creep fatigue performance [85–87]. The ASME *Boiler and Pressure Vessel Code* Case 3024 was approved in 2021 for Alloy 282 [88]. Because of potential applications in steam and supercritical CO_2 systems, the high-temperature corrosion performance of Alloy 282 has been evaluated in various environments at 700°C–800°C [83, 89–94]. Small mass changes have been observed at 750°C for up to 10,000 h of exposure with limited internal oxidation penetration, and oxidation in steam or supercritical CO_2 is not considered as a critical factor for the alloy up to 750°C.

Haynes 282 powder is a commercial product proposed by several key powder manufacturers, including Praxair, Oerlikon, Hogonas, and PAC, and key AM machine manufacturers such as Renishaw and EOS can provide recommended printing parameters for the alloy. A few research projects are exploring the use of LPBF 282 for the fabrication of high-temperature supercritical CO_2 heat exchangers [95, 96], but limited information has been shared by industry on current applications.

3.2.1.2 Microstructure, Mechanical Properties, and Environmental Effects

A key goal when developing alloy 282 was to balance the alloy strength and fabricability by carefully controlling the titanium and aluminum contents to achieve a γ′ volume fraction of approximately 20% [84]. As shown in Figure 1, this relatively low volume fraction of strengthening γ′ for a superalloy is also limiting or suppressing hot cracking during AM printing, which explains the growing interest for the alloy from the LPBF community and gas turbine industry. Crack-free, high-density LPBF 282 has been fabricated, and the as-printed microstructure consisted of textured grains elongated along the BD, also with the presence of a cellular structure [81, 97–98]. Slightly lower YS and ultimate TS and higher ductility have been reported for the as-printed LPBF 282 in comparison with wrought 282, with higher strength but lower ductility perpendicular to the BD [97]. After conducting a full heat treatment with a solution annealing at 1,150°C for 1 h and the standard double-aging treatment—2 h at 1,010°C followed by 8 h at 788°C—the situation was reversed, with higher YS and ultimate TS for the annealed LPBF 282 compared with wrought 282 but lower ductility. Shaikh et al. also measured tensile properties at 800°C and reported similar strength for the annealed LPBF 282 and wrought 282 but higher ductility for the wrought alloy [97]. Notably, the standard solution annealing at 1,150°C for 1 h did not result in alloy recrystallization, as already mentioned by Christofidou et al. [99]. To achieve recrystallization, Boswell et al. annealed the LPBF 282 alloy for 1 h at 1,250°C, followed by a one-step aging treatment at 788°C for 8 h [98].

To date, no fatigue data have been published on LPBF 282, and only a few short-term creep tests have been performed on annealed LPBF 282. Boswell et al. performed 10 creep tests at 750°C and 410 MPa, and the approximately 80 h lifetime was consistent with wrought 282 data [98]. Shaikh et al. carried out creep testing at 927°C and 89 MPa, and the lifetime was superior to the lifetime for wrought 282 along the BD but inferior perpendicular to the BD [81]. Boswell et al. annealed the material at 1,250°C and achieved recrystallization while elongated grains along the BD were still present after 1 h at 1,150°C for the LPBF 282 material creep tested by Shaihk et al. [81]. The 30 nm γ′ precipitates were observed by Shaihk et al. [81], as expected from the standard single- or double-aging heat treatments for Alloy 282 [100], but Boswell et al. observed larger nonspheroidal γ′ precipitates because of a slow cooling rate after the solution annealing treatment. Finally, no data are currently available on the alloy performance under

irradiation, but one study looked at the oxidation behavior of LPBF and EBM 282. Romedenne et al. discovered that recrystallized LPBF 282 had slightly worse oxidation resistance at 800°C and 950°C compared with as-cast 282 because of its fine grain structure, resulting in faster diffusion of titanium at the surface and incorporation of titanium into the protective chromium-rich scale [101].

3.2.1.3 Alloy 282 Scorecard

Alloy 282 powder is a commercial product routinely produced by key manufacturers. The alloy is considered for AM applications such as supercritical CO_2 heat exchangers [95–96]. Because of its relatively low γ′ content at approximately 20%, the alloy is relatively easy to print, and hot cracking is not considered a major challenge (see Figure 1). An alloy density of >99.5% [81, 97–98] has been achieved by several teams. As will be described later in this report, this current work has shown that a relatively large processing window exists for the alloy. For these reasons, Alloy 282 received high scores in the powder and component manufacturing categories but not as high as Alloys 718 or 625. The PNNL materials scorecards report did not evaluate Alloy 282 because the alloy is not currently considered for nuclear applications. The alloy is, however, well-known by the aerospace, gas turbines, supercritical CO_2, and concentrated solar power communities, with growing interest in LPBF 282. In addition to LPBF, several studies have investigated the microstructure, tensile properties, creep properties, and crack propagation of Alloy 282 fabricated by EBM [102–104], and Alloy 282 wire is available for large-scale AM studies. Therefore, average to low scores were given to the alloy in the history and applications category. Mechanical properties data are already available, mainly for tensile properties at room and high temperatures, and the limited creep studies indicate that LPBF 282 should perform better at high temperatures than Alloy 617 (and likely LPBF 617). With the appropriate heat treatment, recrystallized microstructure with a high density of nano-strengthening γ′ precipitates can be achieved, similar to the wrought 282 microstructure. Alloy 282 scored, therefore, very well to well in the mechanical properties and microstructure categories. Limited information did not allow for scoring most of the criteria in the environmental effects and physical properties categories.

Table 5. Scorecard for Alloy 282

Category	Criteria and corresponding ranking					
Manufacturing/ powder	Powder availability: 4	Powder properties: 4	Powder chemistry: 3	Cost: 3	Recycling: ND	—
Manufacturing/ components	Printability (LPBF): 4	Defects: 4	Post-treatment: 3	Processing window: 3	Weldability: 3	Surface roughness or finish: 3
History and applications	NE experience: 0	Other industry experience: 2	Data availability: 3	Code data availability: 0	Experience with non-LPBF AM: 3	Scaling up: ND
Mechanical properties	Creep: 5	Fatigue: ND	Creep-fatigue: ND	High-temperature tensile strength: 5	Room temperature: 5	—
Environmental effects	Radiation resistance: ND	Oxidation resistance: 3	Stress corrosion cracking: ND	Molten salt: ND	Liquid metal: ND	—

Table 5. Scorecard for Alloy 282 (continued)

Category	Criteria and corresponding ranking					
Physical properties	Thermal properties: 3	Solidification-relevant properties: ND	Other modeling-relevant properties: ND	CT-relevant properties: 3	—	—
Microstructure	Material homogeneity: 3	Microstructure stability: 3	LPBF microstructure specificity: 4	—	—	—
ND: not determined						

3.2.2 Alloy 617

Alloy 617 (Ni–[20–24]Cr–[10–15]Co–[8–10]Mo–[0.65–1.15]Ti–[0.8–1.5]Al–[0.05–0.15]C) was discussed in detail in the PNNL materials scorecards report [8]. The attractiveness of Alloy 617 comes mainly from the alloy code qualification in 2019 for the construction of nuclear components in ASME *Boiler and Pressure Vessel Code* Section III. As a solution-strengthened alloy with temperatures of use up to 950°C, Alloy 617 is considered for VHTR designs. The alloy's high strength is also of interest for MSRs, but the high chromium content limits the alloy's compatibility with chloride and fluoride salts. The drawbacks of Alloy 617 are the lack of powder availability and the limited number of studies published to date on AM 617. Although 617 powder is not currently a commercial product, ordering 617 powder from Praxair is occasionally possible based on other customers' requests, and 90 lb of Alloy 617 will be acquired in October 2023 to assess the alloy printability. To the authors' knowledge, only two papers have been published on the fabrication and characterization of Alloy 617 by AM, and in both cases, the alloy was fabricated by wire-based AM [105–106]. The 617 scorecard is given in Appendix A, as well as the scorecards for the alloys discussed in the next sections. Most of the criteria could not be evaluated because of a lack of available information.

3.2.3 Alloy 230

Haynes 230 (Ni–22Cr–14W–2Mo–0.02La) is a solution-strengthened alloy developed by Haynes International with a high tungsten content and is known for its good oxidation resistance in various environments. Creep data from the Haynes database were added to the LMP plot in **Error! Reference source not found.**, showing creep strength similar to the creep strength of Alloy 617. The alloy is mainly used in the aerospace and power industries because of its microstructure stability and corrosion resistance at high temperatures. Alloy 230 powder is a commercial product produced by several powder manufacturers such as PAC, Hoganas, and Oerlikon. Only a few recent studies have been published on AM 230 [107–109], but the chemistry of the powder was modified to facilitate printing. Alloy 230 powder has been received from PAC, and printing of the powder was initiated in September 2023. It will provide the opportunity to directly compare the microstructure, tensile, and creep properties of LPBF 230 and LPBF 617, in addition to the current work on LPBF 282.

3.2.4 Alloy 233

Haynes 233 (H233) is an aluminum-containing solution and carbide-strengthened alloy designed for extreme high-temperature oxidation resistance [110]. It can be precipitation-strengthened at intermediate temperatures. Because it has a significant cobalt addition, it should not be used for in-core applications. No data on H233 parts produced by LPBF are available in the published literature. H233 powder can be made by licensed suppliers but is not generally available off the shelf.

3.2.5 Alloy 740(H)

Inconel 740 (Ni–24.5Cr–20Co–1.35Al–1.35Ti–1.5Nb) is a nickel-based, γ′-strengthened superalloy produced by Special Metals. The alloy is often compared with Alloy 282 with similar creep strength and is considered for similar applications [85, 89–94]. Alloy 740(H) powder is not currently a commercial product, and it was decided to focus attention and resources on Alloy 282 in FY 2023. Notably, a researcher from Special Metals attended the AMMT industrial workshop, highlighting a growing interest in AM technology from the company.

3.2.6 GRX-810

GRX810 is an ODS, high-cobalt, medium-entropy, nickel-based alloy invented by NASA [75] as a printed nickel alloy for very high-temperature service at temperatures >810°C. As shown in Figure 2, initial data show superior creep strength at 1,093°C compared with other nickel-based alloys. Because it contains cobalt, it cannot be used for in-core applications. GRX-810 powder is not yet available from any commercial suppliers. It requires a specialized acoustic mixing step to incorporate Y_2O_3 dispersoids into the metal powder [75].

3.3 LOW-CHROMIUM, MOLTEN SALT–COMPATIBLE, NICKEL-BASED ALLOYS

3.3.1 Hastelloy N

Hastelloy N (Ni–7Cr–16Mo) was developed by ORNL for use in ORNL's MSR. The alloy, with its low chromium content, continues to be a reference in terms of molten salt compatibility [111]. The alloy was extensively discussed in the PNNL materials scorecards report [8]. Although the alloy scored well in the programmatic factors category owing to its importance for MSRs, the overall rating of the alloy was low because Hastelloy N powder is not a commercial product, and very limited work has been conducted on Hastelloy N fabricated by AM. However, very recently, Pillai et al. demonstrated fabrication by DED of a graded structure from the chemistry of Hastelloy N for molten salt compatibility to the chemistry of Alloy 282 for high creep strength [112]. Discussions with Praxair were initiated by both ORNL and INL to obtain a custom-made batch of Hastelloy N, and printing will likely take place in FY 2024.

3.3.2 Alloy 244

Alloy 244 (Ni–8Cr–22.5Mo–6W) was developed by Haynes as a high-temperature, low–thermal expansion coefficient alloy. The low chromium content makes the alloy attractive to molten salt applications, and the creep data shown in Figure 2 and Figure 3 highlight the alloy's excellent creep strength, with lifetimes two orders of magnitude longer compared with Hastelloy N when tested under similar conditions. One drawback is the high concentration of refractory elements, leading to a higher cost. As for Hastelloy N, the alloy is not commercially available, and no work has been conducted on AM 244. The fabrication for the first time by LPBF of the alloy is of interest for MSRs, and Alloy 244 powder will likely be purchased from Hoganas in FY 2024. The goal is to assess the printability of the alloy, optimize the microstructure, and generate tensile data. LPBF 244 should offer much-higher temperature capability in comparison with LPBF Hastelloy N.

4. ONGOING CHARACTERIZATION OF NICKEL-BASED ALLOYS

4.1 ALLOY 718

As mentioned previously, limited creep studies have been published on LPBF 718, all reporting lower lifetime and lower ductility compared with wrought 718. The use of LPBF materials previously fabricated

under the TCR program was a great opportunity to initiate creep testing on material with a well-known pedigree [30, 40]. Because the material exhibited excellent tensile properties after the HT2 heat treatment described previously, it was decided to assess the material creep properties in the as-printed and after exposure to HT2. A Concept X-Line 2000R machine at the Manufacturing Demonstration Facility (MDF) was used to fabricate a large block, and the powder chemistry provided by the supplier was Ni–18.22Fe–19Cr–5.15Nb–0.93Ti–0.5Al–0.04Si–0.04C–0.0012N–0.016O in weight percent. The large block was sectioned into four identical pieces with nominal dimensions of 59 × 18 × 15 mm, and one was heat-treated according to HT2.

Prior to creep testing, microstructural evaluation was performed at the grain level and lower length scales. Standard metallographic grinding using successively finer grits of SiC paper and polishing using diamond solutions with successively decreasing particle sizes of 6 μm, 3 μm, and 0.25 μm were performed until a mirror-like surface was achieved with approximately 0.02 μm silica particles. Surface characterization was performed on a Tescan MIRA3 GHM scanning electron microscope using 20 keV electrons. Electron backscatter diffraction (EBSD) Kikuchi band patterns were collected on an Oxford Instruments Symmetry EBSD detector with AZtec software using a step size of 1 μm. At each point, the AZtec software indexes the Kikuchi band structure and determines the Euler angles of the lattice. The open source MTEX toolbox [113] was used to generate orientation maps and inverse pole figures and to determine grain sizes from the Euler angles exported from AZtec for grains consisting of more than five pixels. The equivalent grain diameter was calculated by taking the area of the 2D grain determined by the orientation map, A, and assuming a circular area through Equation 1, and the degree of sphericity was calculated from this diameter, the grain boundary area, and the length of the grain perimeter, *P*, through Equation 2. The sphericity, Ψ, ranges from 0.5 being a perfect circle to 0 being a straight line.

$$d_{\mathrm{eq}} = 2\sqrt{\frac{A}{\pi}}, \text{ and} \tag{1}$$

$$\Psi = \frac{A}{\frac{1}{2} d_{\mathrm{eq}} \times P}. \tag{2}$$

Microstructure characterization occurred at regions nearest to the gauge region of the SS3-type dog bone specimens and consisted of backscattered scanning electron microscopy (BSE-SEM) with electron backscatter diffraction (EBSD) to quantify grain size and morphology. An example of the length scales of this investigation are shown in Figure 6 for the as-printed LPBF 718. Even with the minimal contrast from typical BSE-SEM imaging, a columnar grain structure is visible, oriented along the BD. This texture became apparent in the EBSD grain orientation maps, shown in Figure 7 with the corresponding sphericity. Many grains in the as-printed LPBF Alloy 718 displayed a [001] orientation or near there and elongated preferentially in the BD. This characteristic is evident in the sphericity, where larger grains display a lower degree of sphericity. Within the grains, the color intensities corresponding to grain orientation are not uniform, suggesting a degree of residual stress internal to the grains causing minor variations in crystal structure. The observations in the as-printed LPBF Alloy 718 are in stark contrast to the HT2 condition in which the grains are much larger with uniform orientations within each grain. Transmission electron microscopy (TEM) revealed the presence of a high density of γ'' in HT2 [40]. TEM of as-printed Alloy 718 is ongoing to determine the nanoscale microstructure and assess heterogeneities such as a dislocation cell structure that may influence the creep behavior.

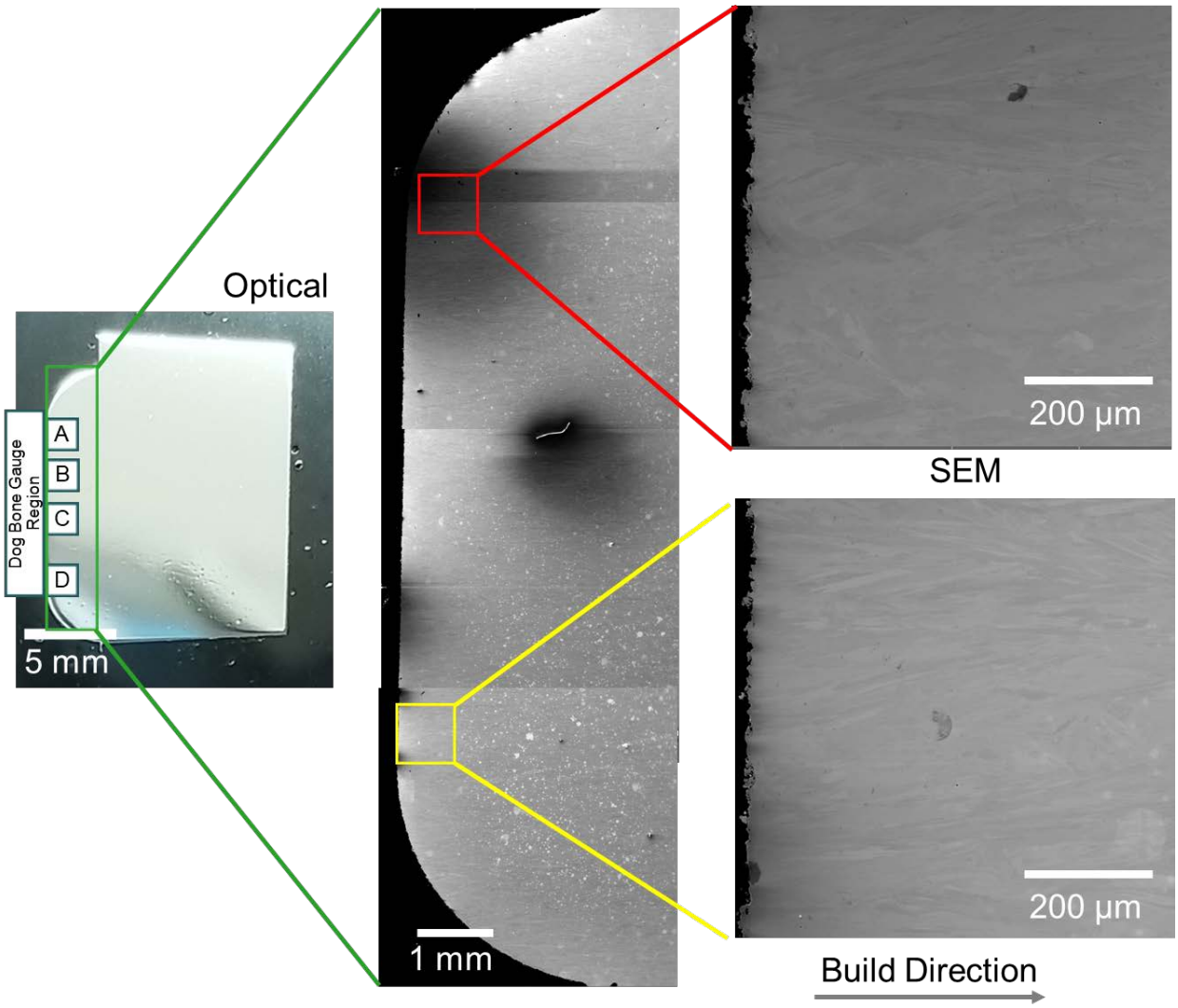

Figure 6. Overview of the microstructure characterization across length scales for as-printed superalloy 718 near the gauge region of a creep dog bone.

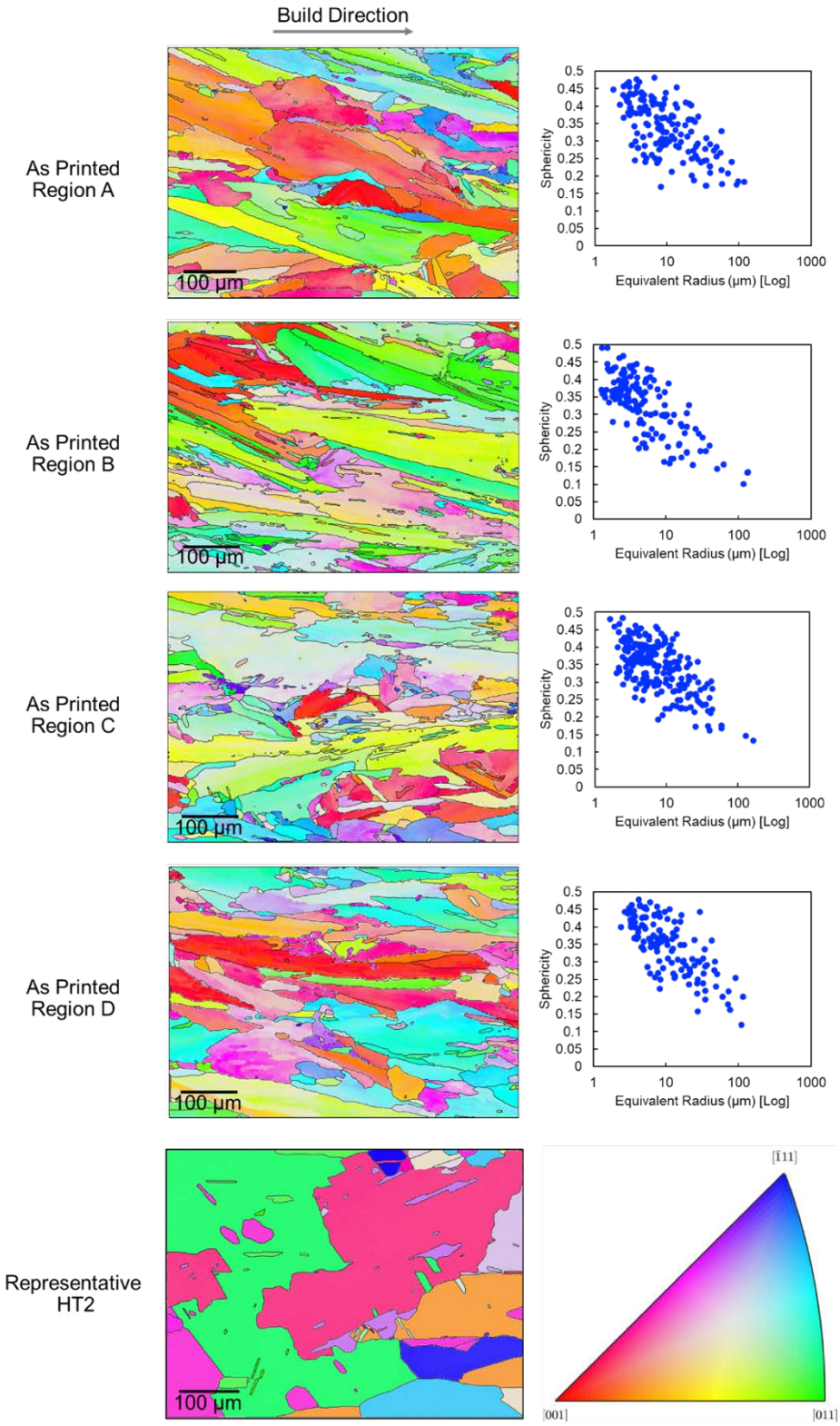

Figure 7. EBSD orientation maps for as-printed LPBF Alloy 718 with regions corresponding to those identified in Figure 6, with corresponding measures of grain sphericity and a representative EBSD grain orientation map for HT2.

For creep testing, SS3-type dog bone specimens with a gage length of 7.62 mm and a gage section of 1 × 2 mm were machined along and perpendicular to the BD from an as-printed approximately 9 × 29 ×15 mm LPBF 718 rectangular block, as shown in Figure 8. Specimens were also machined along the BD from the block annealed according to HT2, and all the specimens were polished using 600 grit sandpaper before creep testing. Testing was then conducted on dead-load frames equipped with a radiation furnace using custom-made high-temperature grips for shoulder loading. Rods clamped to the top and bottom grips were connected to two linear variable differential transformers to generate semiquantitative creep curves. Two thermocouples were attached to the specimens, and the temperature was controlled within ±2°C of the target temperature. Creep testing was conducted at 600°C with an applied stress of 750 MPa and at 650°C with an applied stress of 600 MPa or 650 MPa. Generated creep curves are shown in Figure 9, and the creep results are summarized in Table 6.

As reported in the literature, most of the specimens exhibited low ductility, with a 2%–5% ductility at rupture except for one HT2 specimen, which had a ductility of 9.5%. The creep lifetimes were slightly superior for the HT2 specimens compared with the as-printed specimens, and the lifetime was marginally higher along the BD in the as-printed condition. These results are compared in the Larson–Miller plot presented in Figure 10 with creep data for wrought 718 from Haynes International and LPBF 718 literature data [39, 42–44]. The LMP was calculated according to the relation in Equation 3:

$$LMP = T \times (C + \log[t_r]), \tag{3}$$

with $C = 20$, temperature T measured in in kelvin, and time to rupture t_r measured in hours.

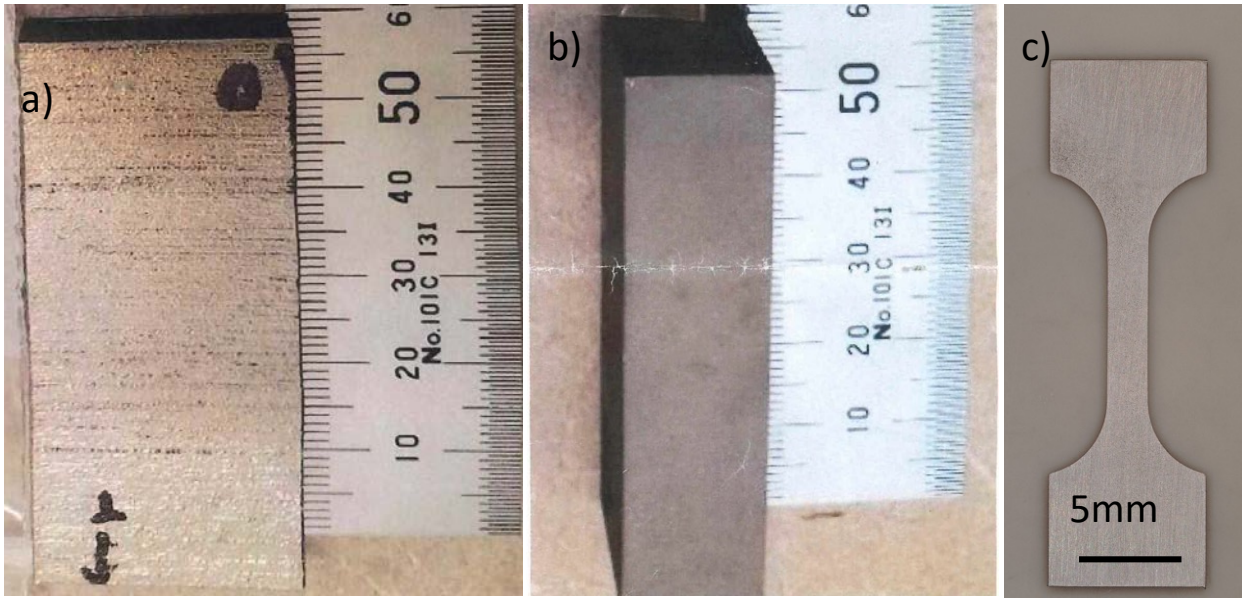

Figure 8. (a) LPBF 718 block used to machine the as-printed specimens along and perpendicular to the BD, (b) block used to machine the annealed specimens along the BD, and (c) example of one annealed specimen before testing.

The specimen lifetimes are overall consistent, with expected lifetimes for wrought 718 and superior to the lifetimes reported in the literature for LPBF 718. The low deformations at rupture are also consistent with reported results for LPBF 718 [46,49–51]. Significant data scattering is expected for the deformation at rupture for wrought 718 [48], but ductility at rupture lower than approximately 2% for LPBF 718 might be a concern for NE structural applications.

Table 6. Summary of the creep tests conducted on as-printed and annealed LPBF 718

Specimen	Condition	Orientation	Temp. (°C)	Stress (MPa)	Lifetime (h)	LMP
9VS1	As fabricated	BD	650	650	385	20850
9VS6	As fabricated	BD	600	750	724	19960
9HS3	As fabricated	Per. To BD	650	650	357	20819
9HS6	As fabricated	Per. To BD	600	750	524	19837
92S1	HT2	BD	650	650	18	19622
92S3	HT2	BD	650	650	463	20924
92S6	HT2	BD	600	750	991	20079
92S4	HT2	BD	650	600	536	20982

Per.: perpendicular

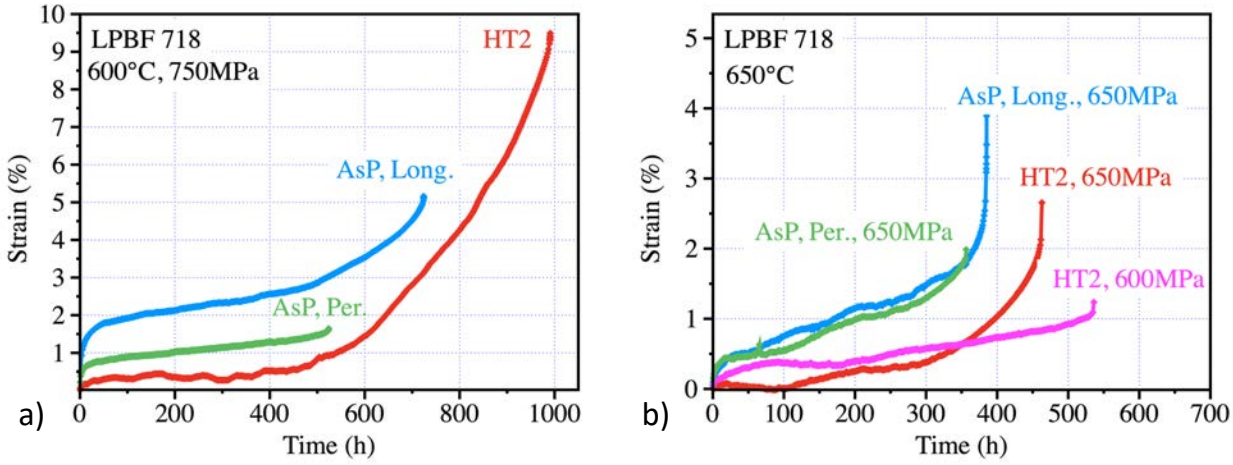

Figure 9. LPBF 718 creep curves for the as-printed and annealed specimens: (a) 600°C, 750 MPa; (b) 650°C, 600 MPa or 650 MPa. *AsP.* stands for *As-printed*, *Per.* indicates perpendicular to the BD, and *Long.* indicates along the BD.

The ruptured specimens were then cross-sectioned and polished using standard metallographic techniques as described previously. BSE-SEM micrographs are shown in Figure 11 for the specimen tested at 650°C and 650 MPa in the as-printed condition and tested along the BD. Only a few cracks were observed, and as shown in Figure 11b, these cracks were related to void formation at grain boundaries. As shown in Figure 11b–6c, the initial cellular structure was still present after 385 h at 650°C, with elongated cells approximately 1 µm in size. Figure 11c also highlights locally the formation of a dendritic structure rather than a cell structure with significant chemical segregation, as illustrated by the niobium energy-dispersive x-ray spectroscopy (EDS) map in Figure 11d.

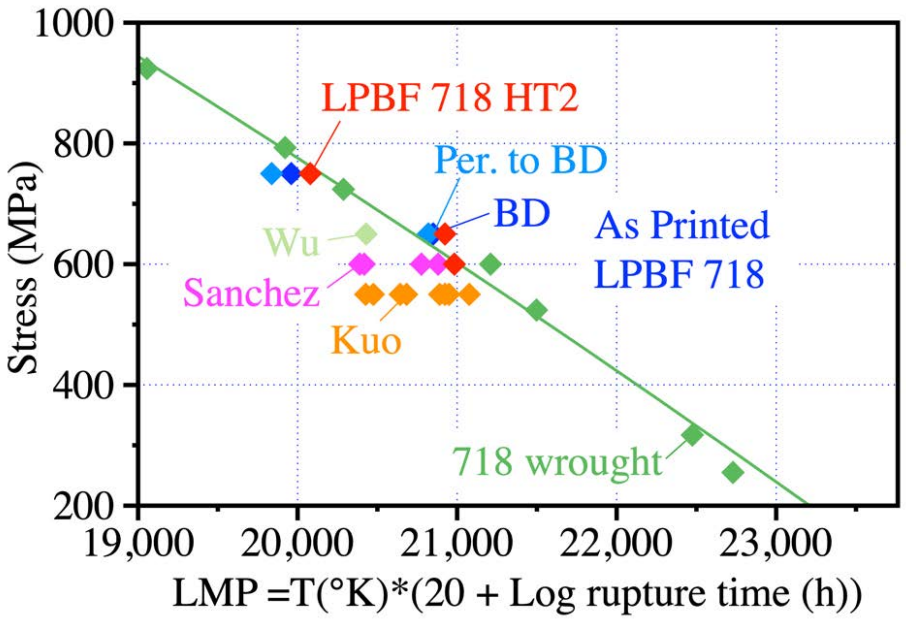

Figure 10. Comparison in a Larson–Miller plot of the creep performance of the LPBF 718 alloy with wrought 718 according to the Haynes data sheet and LPBF 718 literature data [46, 49–51].

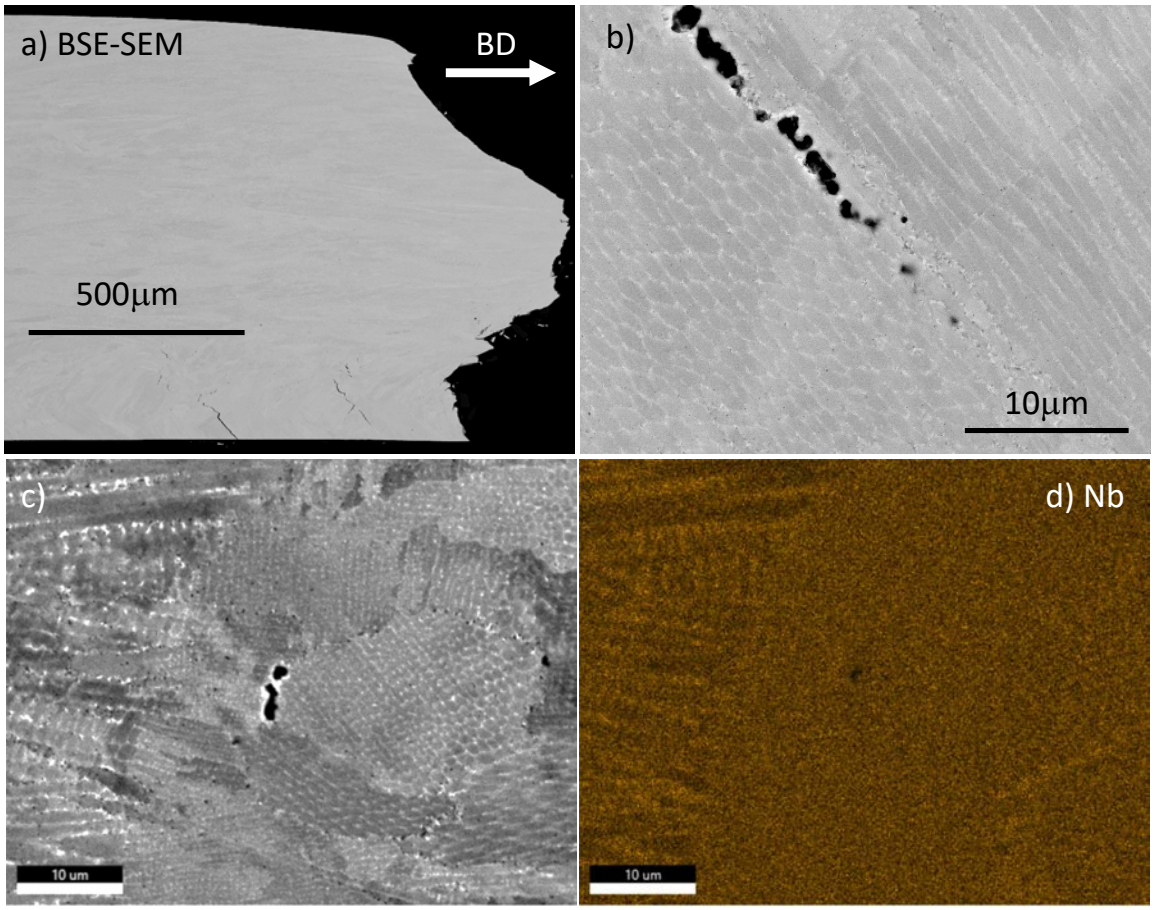

Figure 11. BSE-SEM cross section micrographs of the as-printed specimen machined along the BD after creep testing at 650°C and 650 MPa for 385 h.

As shown in Figure 12, similar microstructural features were observed for the as-printed specimens tested at 650°C and 650 MPa perpendicular to the BD. Voids and cracks were again observed mainly at grain boundaries with the clear presence of a cellular structure. The EDS elemental maps in Figure 13 revealed the segregation of molybdenum and niobium at the cellular structure level. Although segregation of titanium was not clearly observed, several authors have reported the formation of (Mo, Nb)-rich Laves phases in the walls of the LPBF 718 cellular structure [44, 49–50]. Figure 13a revealed that similar precipitates have formed at grain boundaries, with also the presence of chromium-rich precipitates.

As shown in Figure 14, the microstructure was very different for the HT2 specimen creep tested at 650°C and 650 MPa for 463 h. As described in [30, 40] and shown in Figure 7, the HT2 heat treatment resulted in the formation of equiaxed grains and the disappearance of the cell structure, consistent with Figure 14b and Figure 14c. Cracking was again observed only at grain boundaries, with the presence of coarse precipitates, identified in Figure 15 as (Nb,Ti)-rich carbides. The higher magnification micrograph in Figure 14d highlights the presence of the nano size-strengthening γ' and γ'' precipitates, but TEM is needed for in-depth characterization of these precipitates.

The microstructure for the as-printed longitudinal specimen tested at 600°C and 750 MPa was very similar to the microstructure at 650°C and is not reported here. On the contrary, the microstructure for the heat-treated HT2 specimen tested at 600°C and 750 MPa was quite different compared with the microstructure observed at 650°C, and BSE-SEM micrographs are shown in Figure 16. Cracking was, as always, observed at grain boundaries, but needle-like precipitates, likely δ phase, were observed all over

the specimen. These δ precipitates made it more difficult to image the nano γ′ and γ″ precipitates, but Figure 16d clearly reveals the presence of these precipitates. EBSD and TEM will be conducted to clearly identify and quantify all the precipitates in these creep-tested specimens. Although the characterization of the postcreep microstructure is in progress, the strong agreement between the LPBF 718, with or without HT2, and the wrought 718 on the Larson–Miller plot suggests the strong differences in initial grain structure and the nanoscale dislocation cell structure are not the primary influence on creep performance; precipitating phases may be the dominant microstructure feature.

Additionally, although the creep lifetimes presented here are superior to what has been reported in the literature for LPBF 718, likely because of the specific HT2 heat treatment, including homogenization at 1,174°C and 1,204°C, further improvement in creep ductility might be needed for NE applications. In collaboration with other high-temperature alloy programs, additional 718 material will be printed and annealed to further improve understanding of the process–microstructure–creep properties relationship at 550°C–700° C.

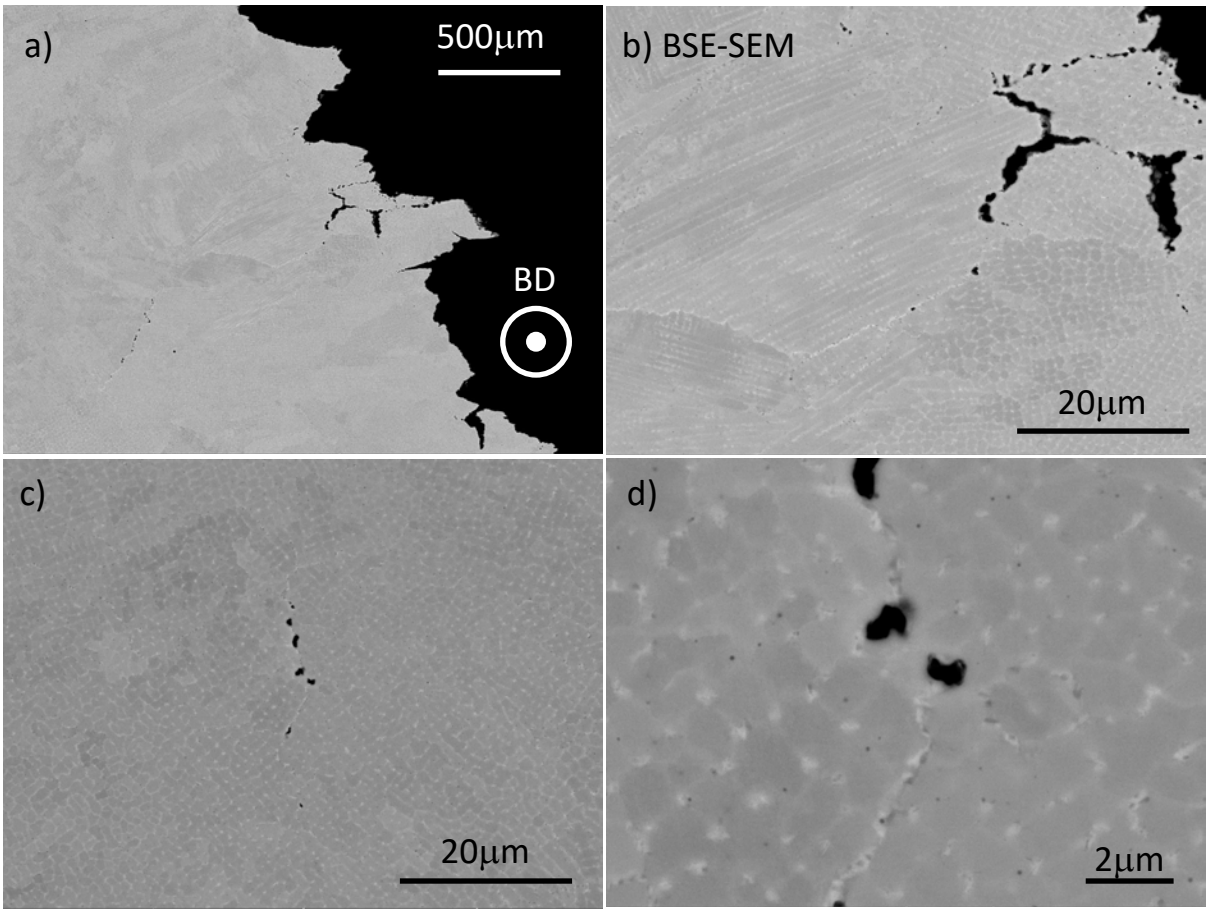

Figure 12. BSE-SEM cross section micrographs of the as-printed specimen machined perpendicular to the BD after creep testing at 650°C and 650 MPa for 357 h.

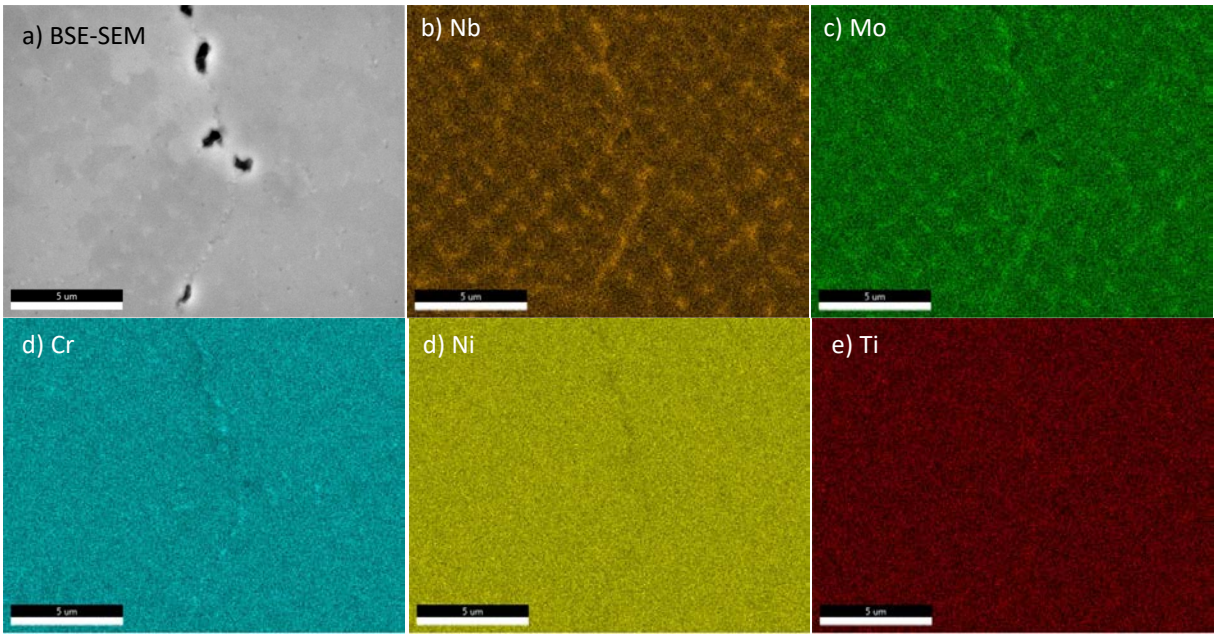

Figure 13. (a) BSE-SEM micrograph of the as-printed specimen machined perpendicular to the BD after creep testing at 650°C and 650 MPa for 357 h, (b)–(e) corresponding EDS elemental maps.

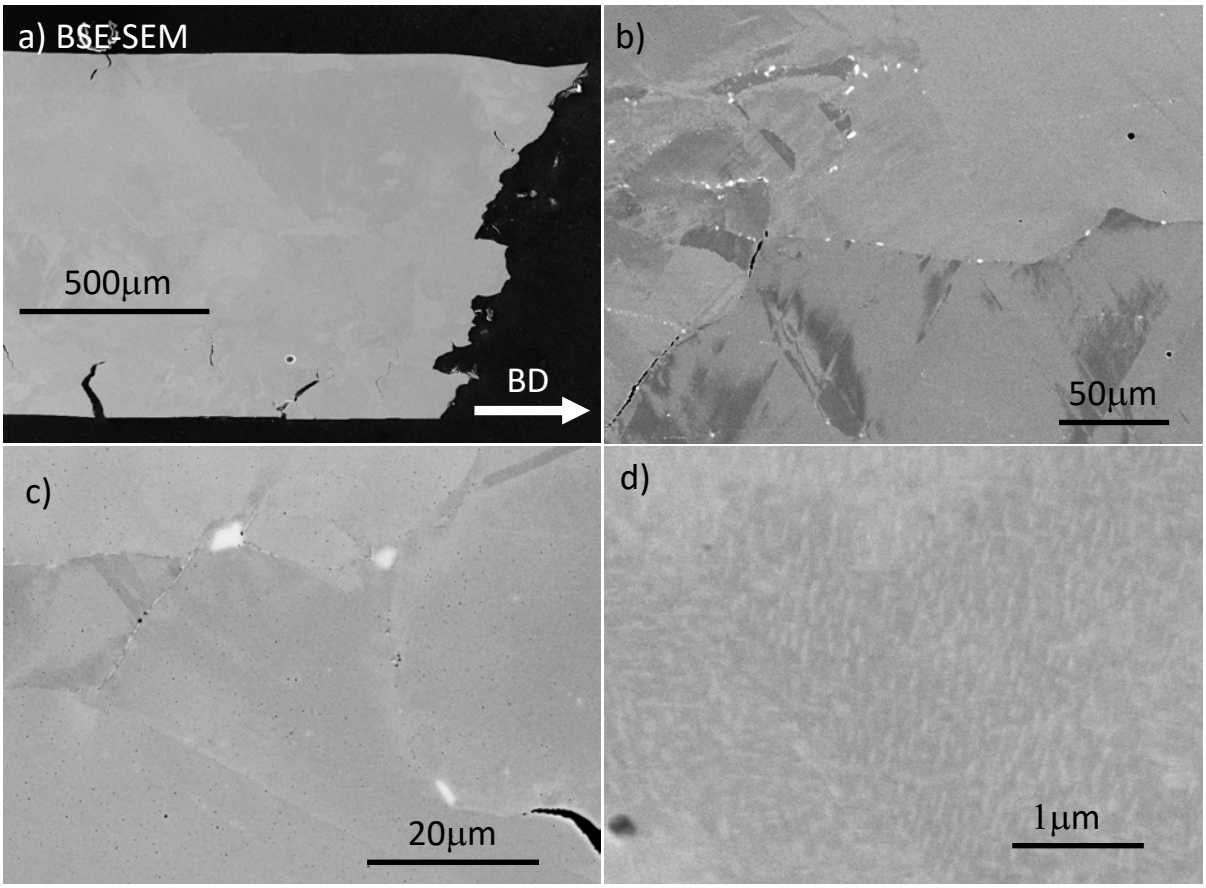

Figure 14. (a) BSE-SEM cross section micrographs of the annealed specimen machined along the BD after creep testing at 650°C and 650 MPa for 463 h.

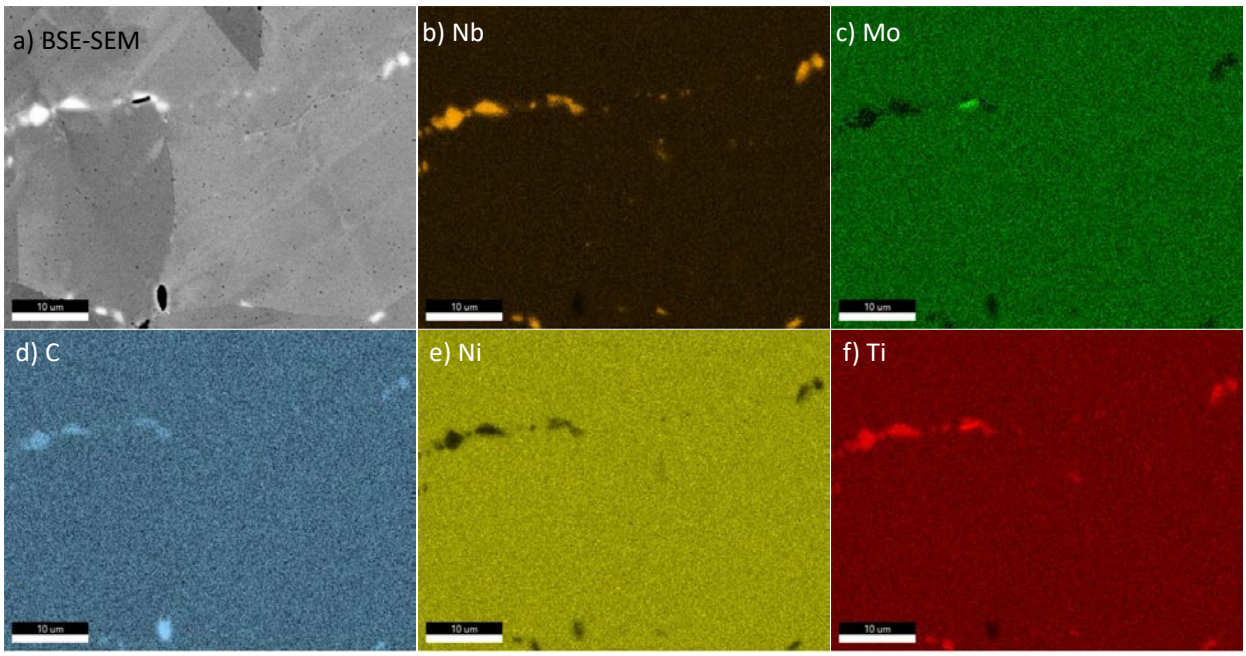

Figure 15. (a) BSE-SEM cross section micrograph of the annealed specimen machined along the BD after creep testing at 650°C and 650 MPa, (b)–(e) corresponding EDS elemental maps.

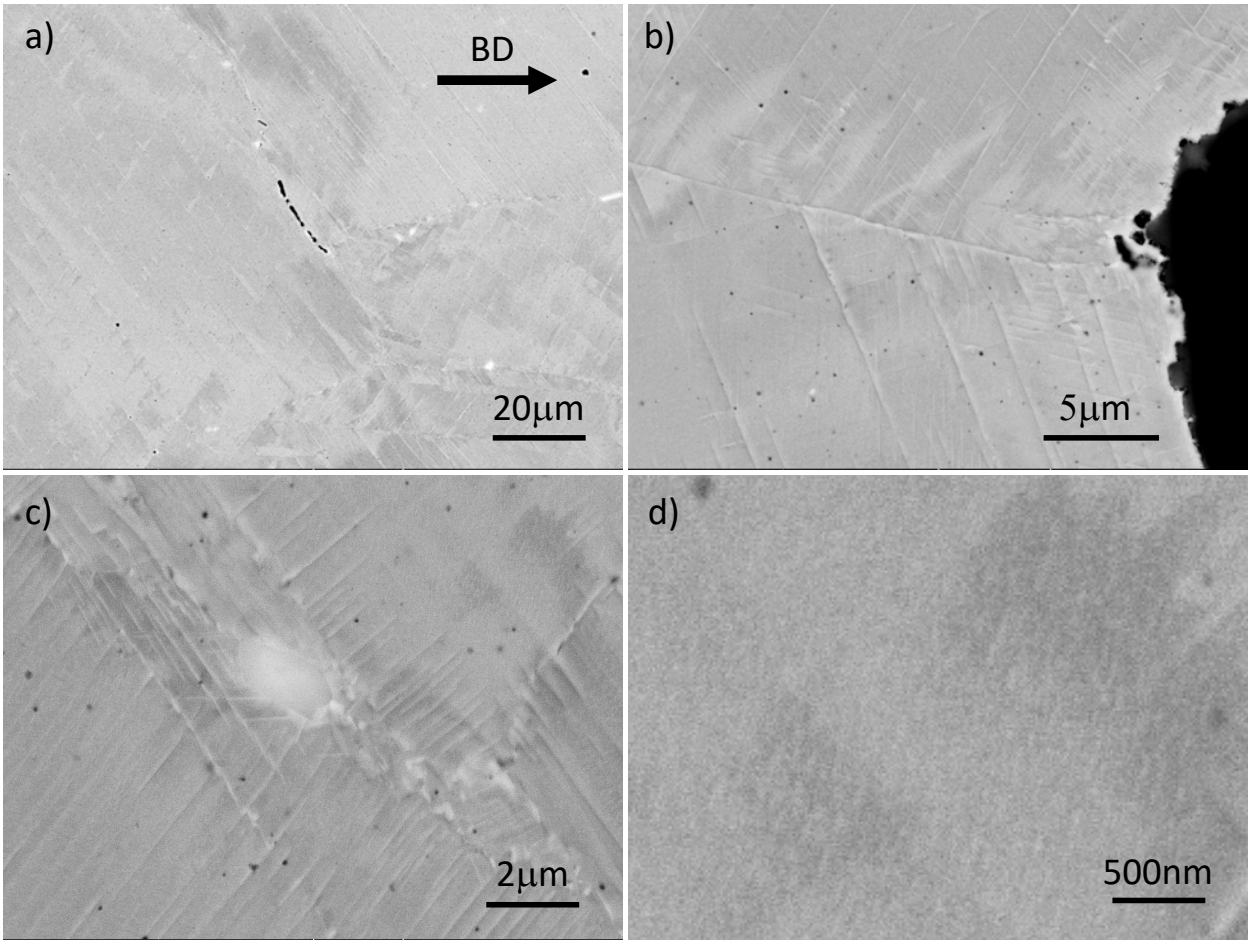

Figure 16. (a) BSE-SEM cross section micrographs of the annealed specimen after creep testing at 600°C and 750 MPa.

4.2 ALLOY 282

4.2.1 Laser Powder Bed Fusion 282 Printing

Alloy 282 was selected for additional evaluation because of the superior properties of the wrought alloy compared with wrought 617, promising existing data for the LPBF 282 alloy, and powder availability. In addition to generating relevant creep, fatigue, and creep-fatigue data for LPBF 282, the goal is to assess the integration of a new alloy into the AMMT accelerated component qualification framework. An amount of 200 lb of 282 powder was purchased from Praxair, and the powder was received approximately 4 weeks after the purchase order was submitted. The powder chemistry provided by Praxair was as follows: Ni–19.37Cr–10.24Co–8.33Mo–2.11Ti–1.54Al–0.05C–0.03Si–0.01O in weight percent. A Renishaw AM250 machine was used at the MDF to optimize the Alloy 282 printing parameters and fabricate large rods and blocks for microstructure and mechanical properties characterization. The Renishaw machine was first upgraded with new cameras to generate during printing in situ data that can be integrated into the AMMT digital manufacturing approach using the Peregrine software [114, 115]. A central composite design centered on Renishaw's recommended laser parameters for Alloy 282 was used to optimize the processing parameters. Although the laser power and layer thickness were kept constant at 200 W and 60 μm, respectively, three key factors were evaluated: the hatch distance, point spacing, and exposure time, resulting in the fabrication of 18 samples. A standard Zeiss geometry was used to be

consistent with current AMMT work on 316H and to facilitate in situ data analysis using the Peregrine software and ex situ CT scan measurements.

Table 7 summarizes the printing parameters for the 18 samples and Figure 17 shows the printing configuration and the resulting Zeiss build.

Characterization of the fabricated samples included visual inspection and mass and skeletal (pycnometer) density measurements. The volumetric energy density (VED) input was also calculated according to the following relationship in Equation 4:

$$VED = \frac{P \times t}{p \times h \times l}, \tag{4}$$

where P is the laser power in Watts, t is the exposure time in microseconds, p is the point spacing in micrometers, l is the layer thickness in micrometers, and h is the hatch spacing in micrometers.

Variations of the specimen mass and skeletal density as a function of the calculated VED are given in Figure 18a and Figure 18b, respectively. The sample mass increased rapidly with increasing VED to reach a plateau at approximately 45 J/mm^3. Visual inspection revealed a high level of porosity at low VED and swelling at high VED. A similar trend was observed for density measurements at VED greater than approximately 42 J/mm^3, but significant results' variability was observed at lower VED. A high fraction of open porosities not included into the skeletal density measurement is likely the reason for the data scattering. Based on these results, parameters corresponding to sample 13 (i.e, hatch spacing of 86 μm, point spacing of 70 μm, and exposure time of 80 μs) were considered to be optimum for the processing of Alloy 282 and were selected for the fabrication of larger builds. Notably, the selected hatch spacing is not the recommended one by Renishaw—86 μm vs. 100 μm—but Renshaw is likely also considering the build rates, which are faster with a 100 μm hatch spacing and could reduce production cost. The two large builds that were then fabricated, one for ORNL and one for INL, are displayed in Figure 19. Each of the rods and rectangular blocks were engraved to ensure the data that will be generated can be integrated into the digital manufacturing approach. The build configurations were based on the standard tensile/creep specimens at ORNL and the standard tensile/creep and fatigue specimens at INL. As shown in Figure 20, the INL smooth button head fatigue specimen is 6 in. long, requiring, therefore, rods 6 in. long and 0.75 in. in diameter or plates 6 in. long and 0.75 in. thick. A summary of all the samples and their corresponding intended use is given in Table 8. In addition to the mechanical testing samples, one rod and four thin plates, 0.02 to 0.08 in. thick, will be used at ORNL for microstructure characterization. Although ORNL was fabricating the 282 material, INL was conducting heat treatments on LPBF 282 rods provided by EOS. Once the optimum microstructure has been achieved, samples will be heat treated and machined. Analysis of the Zeiss build by CT scans was also initiated, and the higher density of the nickel-based alloy did not seem to affect defect detection. Additional information will be provided in the final report.

Table 7. Summary of the LPBF 282 printing parameters for the central composite design

Sample	Hatch (µm)	Point spacing (µm)	Exposure time (µs)	Comments
14	90	65	60	Corner
4	110	65	60	Corner
16	90	75	60	Corner
15	110	75	60	Corner
11	90	65	100	Corner
8	110	65	100	Corner
3	90	75	100	Corner
10	110	75	100	Corner
13	86	70	80	Axial
17	114	70	80	Axial
12	100	63	80	Axial
18	100	77	80	Axial
6	100	70	52	Axial
9	100	70	108	Axial
2	100	70	80	Replicates
7	100	70	80	Replicates
5	100	70	80	Replicates
1	100	70	80	Replicates

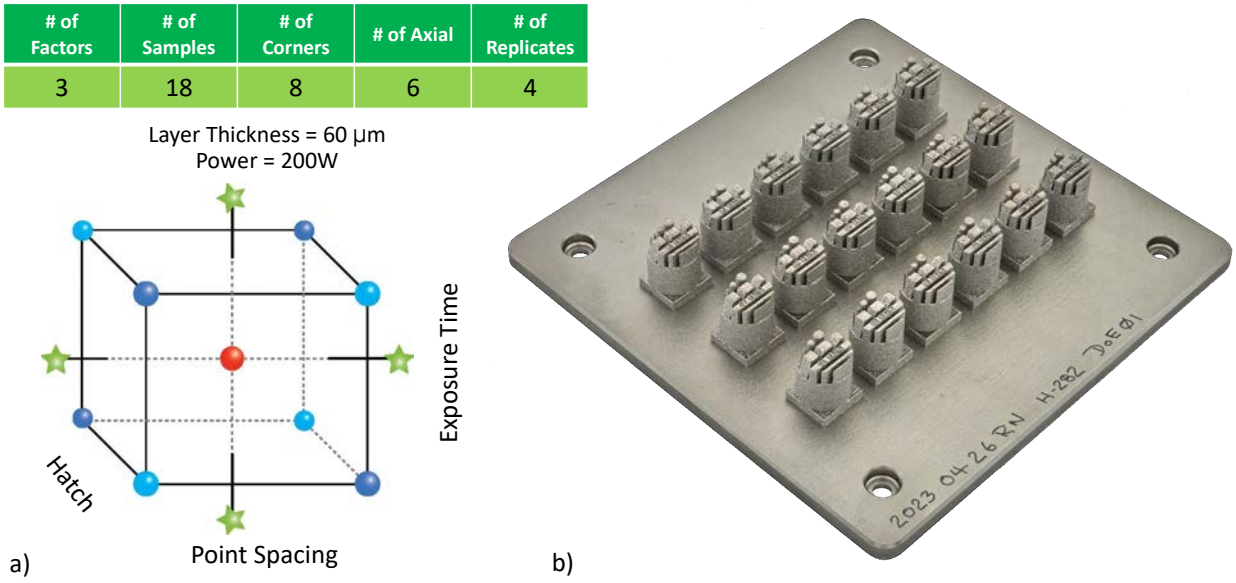

Figure 17. (a) Printing configuration based on the central composite design, and (b) resulting LPBF 282 Zeiss build.

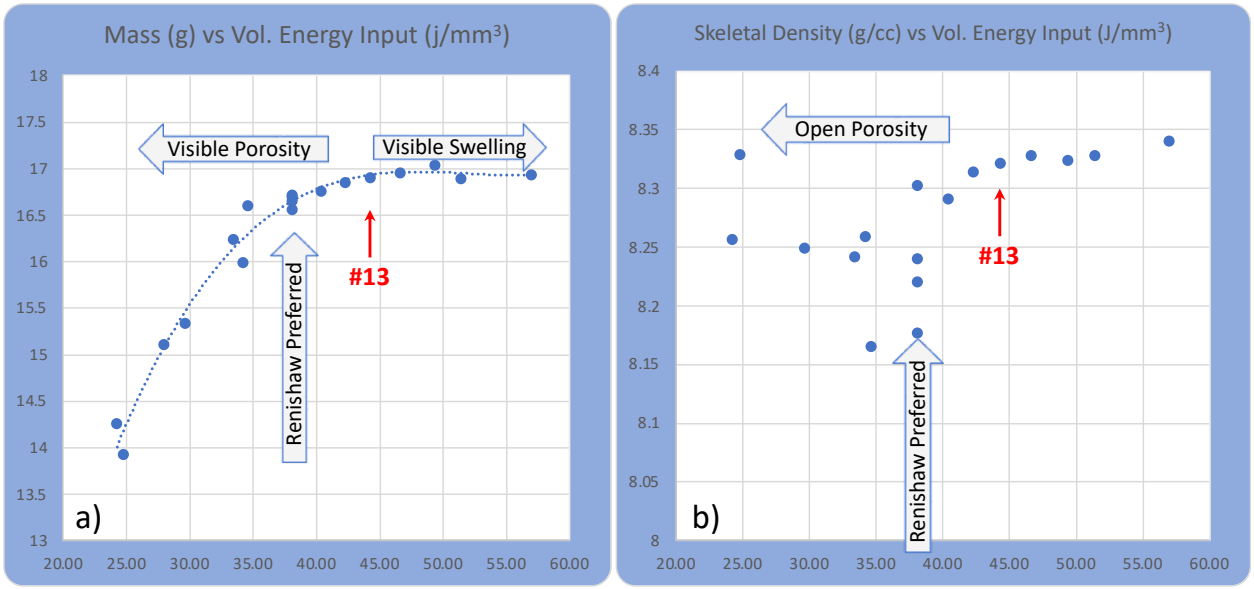

Figure 18. Characterization of the LPBF 282 samples: (a) mass vs. VED and (b) skeletal density vs. VED.

Table 8. Summary of the samples fabricated for characterization and mechanical testing at ORNL and INL

Build	Geometry	Dimension	Number	Testing	Engraving
ORNL	Cylindrical	0.5 in. diameter, 4 in. long	10	Tensile along the BD	T1 to T10
ORNL	Cylindrical	0.5 in. diameter, 4 in. long	10	Creep along the BD	C1 to C10
ORNL	Cylindrical	0.5 in. diameter, 4 in. long	1	Microstructure characterization	MC
ORNL	Rectangular	0.5 × 5 × 4 in.	1	Tensile perpendicular to BD	HT1 to HT7
ORNL	Rectangular	0.5 × 5 ×4 in.	1	Creep perpendicular to BD	HC1 to HC7
ORNL	Thin plates	0.5 × 4 × (0.02, 0.04, 0.06, or 0.08) in.	3	To be determined	1 to 3
INL	Cylindrical	0.5 in. diameter, 6 in. long	8	Tensile along the BD	TV1 to TV8
INL	Cylindrical	0.5 in. diameter, 6 in. long	8	Creep along the BD	CV1 to CV8
INL	Cylindrical	0.75 in. diameter, 6 in. long	8	Fatigue along the BD	FV1 to FV8
INL	Rectangular	0.5 × 6 × 4 in.	1	Tensile perpendicular to BD	V sign
INL	Rectangular	0.5 × 6 × 4 in.	1	Creep perpendicular to BD	V sign
INL	Rectangular	0.75 × 6 × 6 in.	1	Fatigue perpendicular to BD	V sign

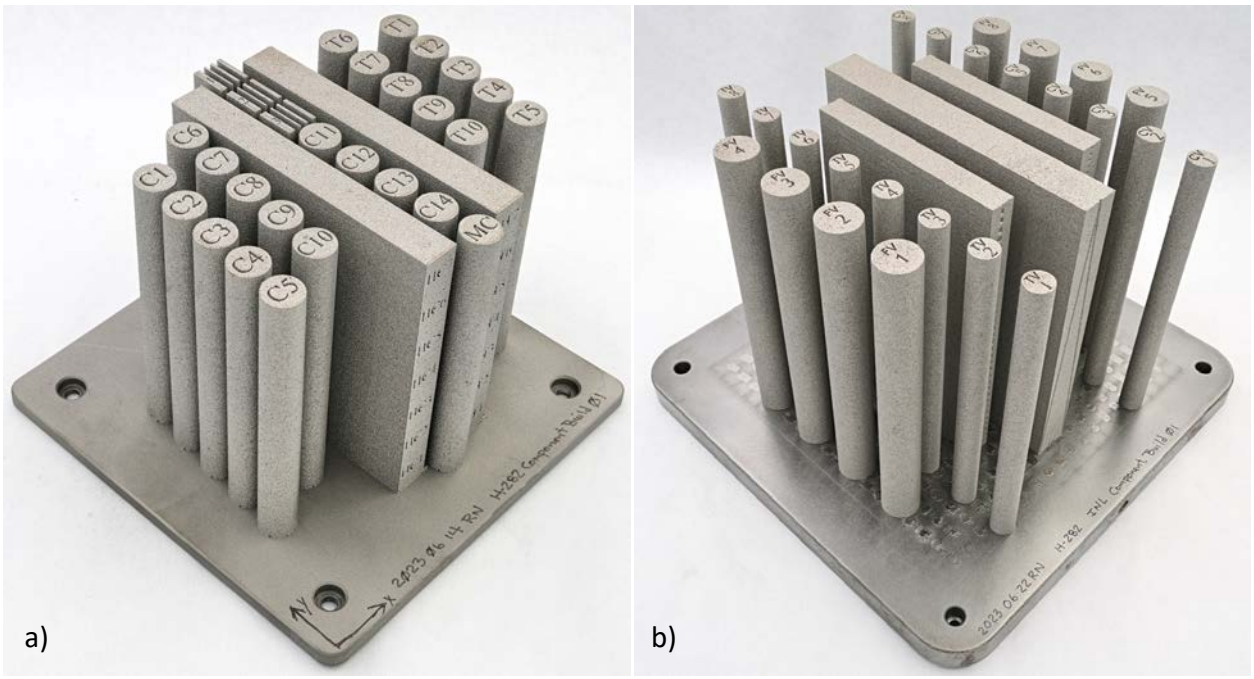

Figure 19. Large builds for mechanical testing: (a) ORNL build, 4 in. tall, and (b) INL build, 6 in. tall.

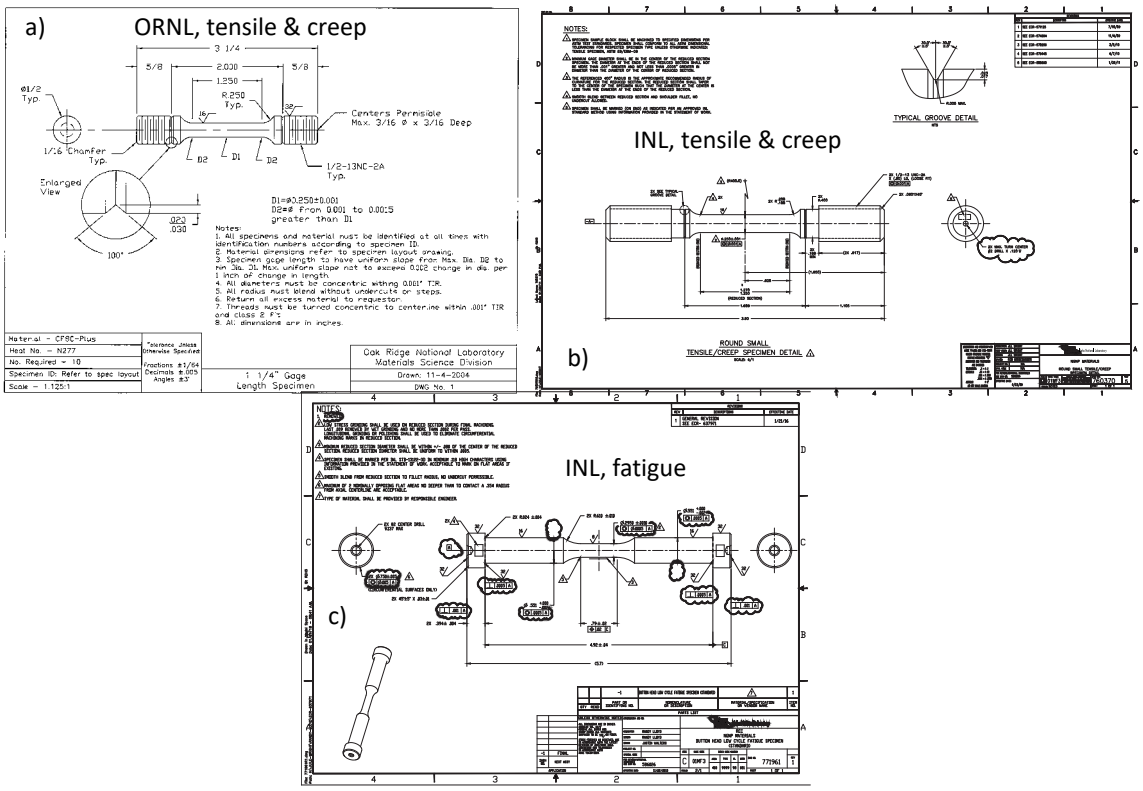

Figure 20. Geometry of the standard specimens: (a) tensile and creep, ORNL; (b) tensile and creep, INL; and (c) fatigue and creep-fatigue, INL.

4.2.2 Digital Manufacturing for 282

As part of the digital manufacturing work package, a digital manufacturing effort is being developed across the MDF, allowing digital record keeping, advanced data analytics, and centralized data storage across a number of manufacturing technologies and material systems. To support the efforts of various work packages in the current FY and beyond, several LPBF systems were instrumented with state-of-the-art sensors and connected to this digital platform. On the Renishaw AM250, for example, three new imaging modalities were installed and connected to an edge computing system at the machine. These sensors include a 20 megapixel visible light camera, a 4.2 megapixel near-infrared (NIR)-sensitive camera, and a long-wave infrared camera. Each of these data modalities can produce multiple images per layer, some of which are used as input to the deep learning algorithm hosted inside of Peregrine, while others are used for digital recordkeeping, process understanding, and data exploration. Data associated with these builds (including build metadata, design files, operators notes, in situ data, and more) can then be recorded as entries in the digital platform for historical tracking and analysis.

Builds performed with Alloy 282 were used as a test bed for these digital integrations, and representative examples of the installed data modalities are exhibited in Figure 21. For example, the visible light camera, which has a spatial resolution of approximately 55 μm, captures two images per layer: a postmelt image and a post-recoat image. In contrast, the NIR camera, which has an approximate spatial resolution of 125 μm, produces a video buffer that is dynamically analyzed at the end of a layer to produce a total of three images. These temporally integrated data modalities are engineered to extract relevant dynamics exhibited in the video buffer and include temporally integrated sum, max, and argmax images.

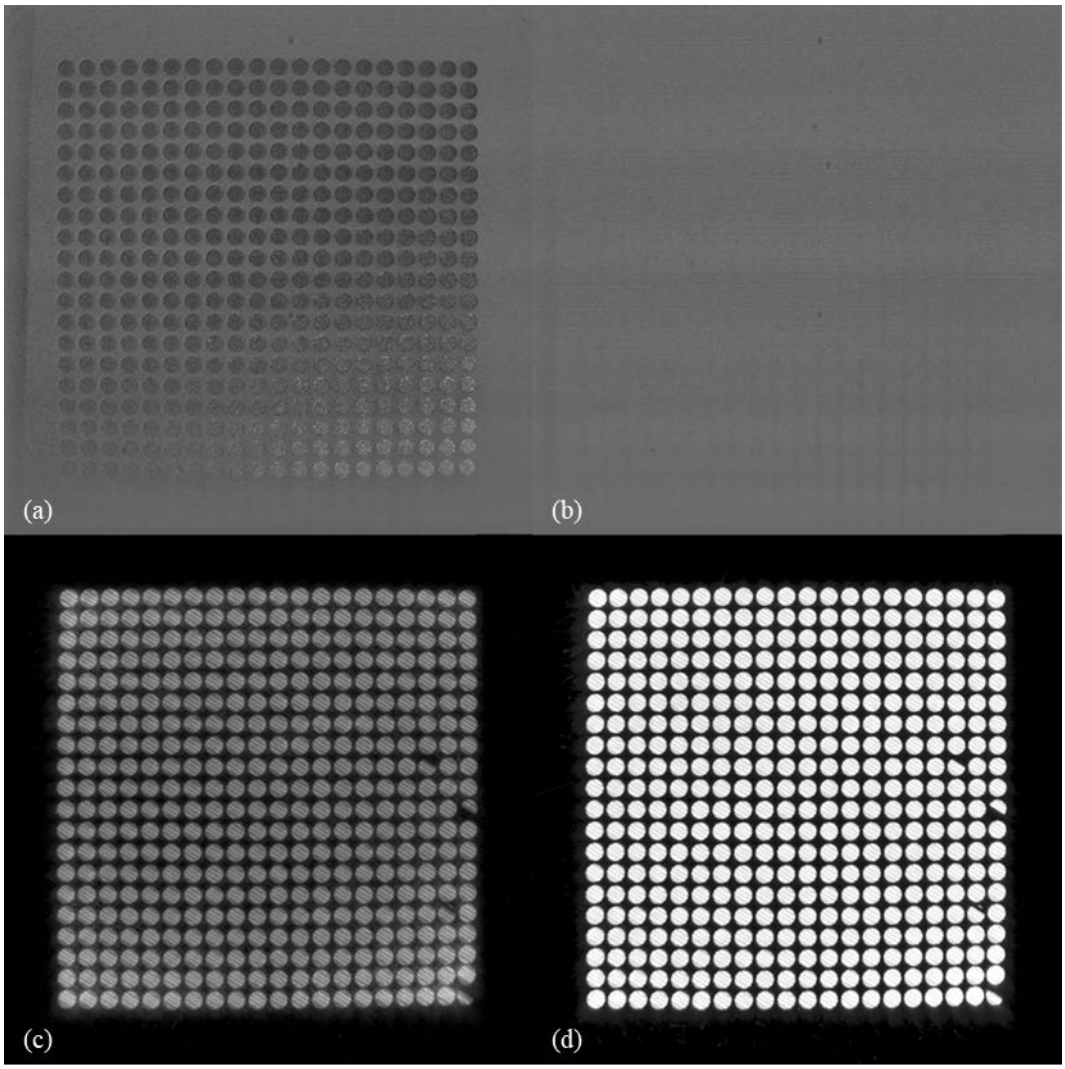

Figure 21. Representative images from the visible light and NIR cameras installed on the Renishaw AM250: (a) postmelt visible, (b) post-recoat visible, (c) temporally integrated sum from the NIR camera, and (d) temporally integrated max from the NIR camera. These four data modalities are used as input for the neural network, initial results for which are shown in Figure 22.

As part of these efforts, a new Peregrine workspace was instituted for the Renishaw AM250, allowing in situ data collection, data registration, and recording of metadata and build notes from the machine operators. Throughout the sensor installation process, numerous hardware and software changes were made to improve the robustness and stability of data acquisition and reduce the influence of temporally integrated imaging artifacts. However, a stable hardware and software solution is being converged upon, which will allow for better comparisons between geometries and materials in the coming FY. As such, a preliminary neural network (NN) has been trained in Peregrine for the Renishaw AM250's workspace, which makes use of four of the imaging modalities produced by the three installed cameras (see Figure 21) to produce a pixelwise segmentation map on a layer-by-layer basis. This preliminary network predicts only four pixel classes, but as more data are added to the training database in the next FY, additional process anomalies (e.g., recoater streaking, incomplete spreading) will also be classified to assess the quality of the printed components.

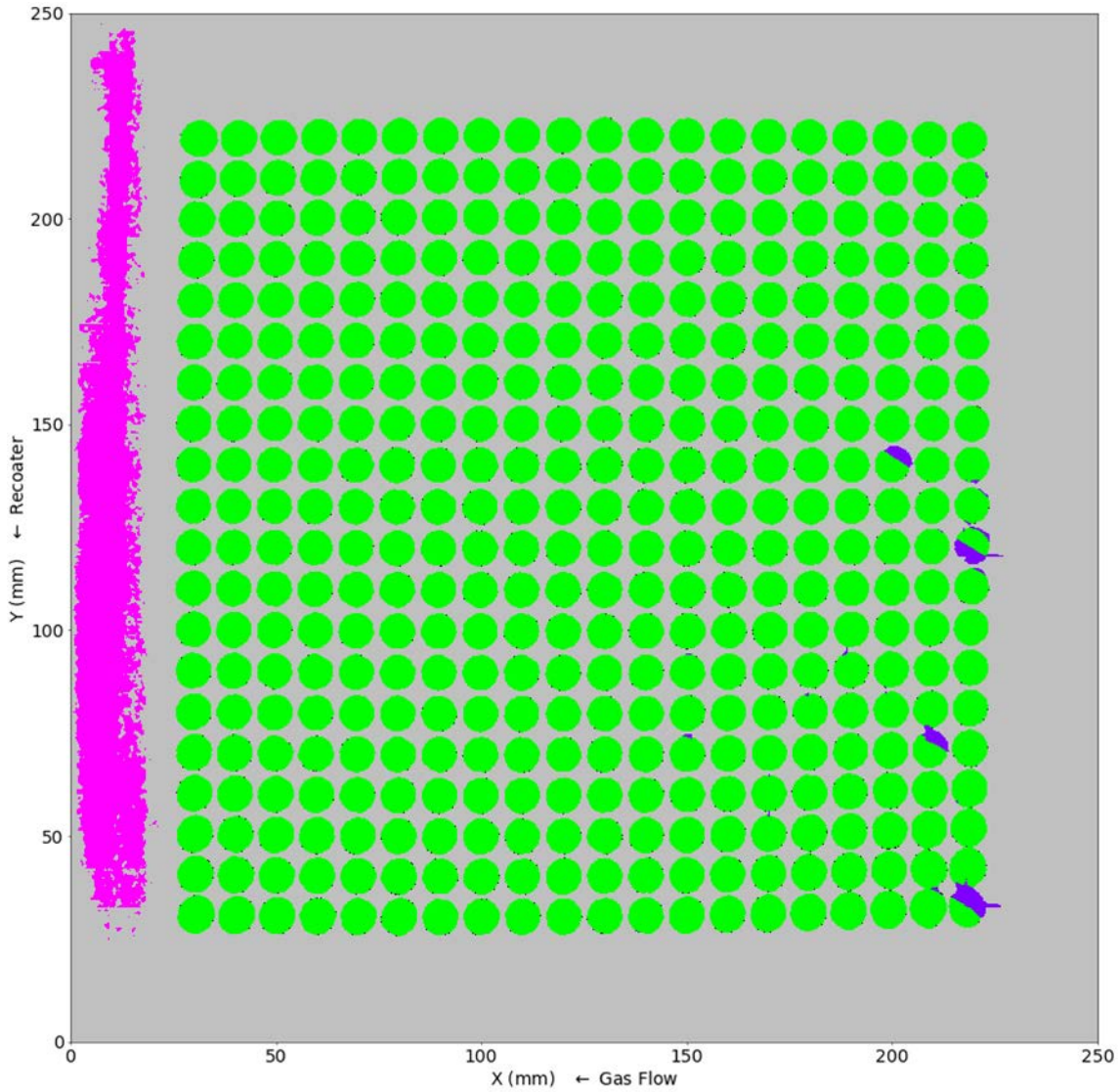

Figure 22. Preliminary NN results for the NN trained in the Renishaw AM250's Peregrine workspace. The network accepts the four data modalities shown in Figure 21 and produces a pixelwise segmentation map on a layer-by-layer basis. For this workspace, four pixel classes were used: (1, gray) unmelted powder, (2, green) printed material, (3, pink) soot or spatter particles, and (4, purple) dropped NIR data frames.

4.2.3 Laser Powder Bed Fusion 282 Heat Treatment

4.2.3.1 Motivation

As stated previously for IN625 and H282, the as-built properties of nickel-based alloys manufactured by LPBF are anisotropic because of their anisotropic microstructures. This anisotropy manifests itself in everything from room-temperature tensile properties to high-temperature creep properties and is undesirable because it imparts a directional dependence of design stresses for components. One way to reduce the anisotropy of mechanical properties is to heat treat the microstructure. Various authors [81, 98–99, 116] found that the standard wrought solution heat treatment at 1,100°C did not recrystallize the anisotropic microstructure produced by LPBF. A study of the recrystallization kinetics of LPBF H282 is therefore in progress to optimize the microstructure and minimize anisotropy. Once this study is completed, high-temperature mechanical testing (creep and fatigue, primarily) will be performed to

provide additional data on these properties for LPBF material because such a limited amount of data currently exists such that it is difficult to determine the usability of these alloys produced by LPBF.

4.2.3.2 Materials

EOS Sweden supplied four bars of H282 manufactured by LPBF, with each bar measuring $72 \times 13 \times 13$ mm^3. The bars were sectioned in the build and transverse directions to characterize the as-built microstructure. Pieces in both directions were then encapsulated in quartz tubes that were evacuated and partially backfilled with argon gas to avoid oxidation during heat treatments. The quartz tubes were heat-treated in a standard tube furnace under the following conditions: 1,250°C for 1 and 2 h, 1,210°C for 2 h, 1,180°C for 1 h, and 1,100°C for 1 h. All samples were furnace-cooled after the completion of the heat treatment.

Samples for microstructural examination were mounted and prepared using standard SiC papers and diamond polishing suspensions. Samples for EBSD analysis were finally polished with 0.01 μm colloidal silica. Samples for optical microscopy were electrolytically etched in 10% oxalic acid at 2.2 V. EBSD was performed on an FEI Quanta field emission gun scanning electron microscope using a magnification of 200×, working distance of 14–15 mm, and step size of 0.8–0.9 μm.

4.2.3.3 Results to Date

Figure 23 shows an optical micrograph of the as-built H282 samples. In the figure, the BD is toward the top of the page. Overlapping melt pools are visible, as are elongated columnar grains and areas of cellular microstructure. A small amount of round, gas-induced pores are also visible. Figure 24 shows the same sample in the transverse direction. The grain size appears much smaller and the laser scanning tracks are visible in this orientation. A small amount of gas porosity and one irregular-shaped pore are visible.

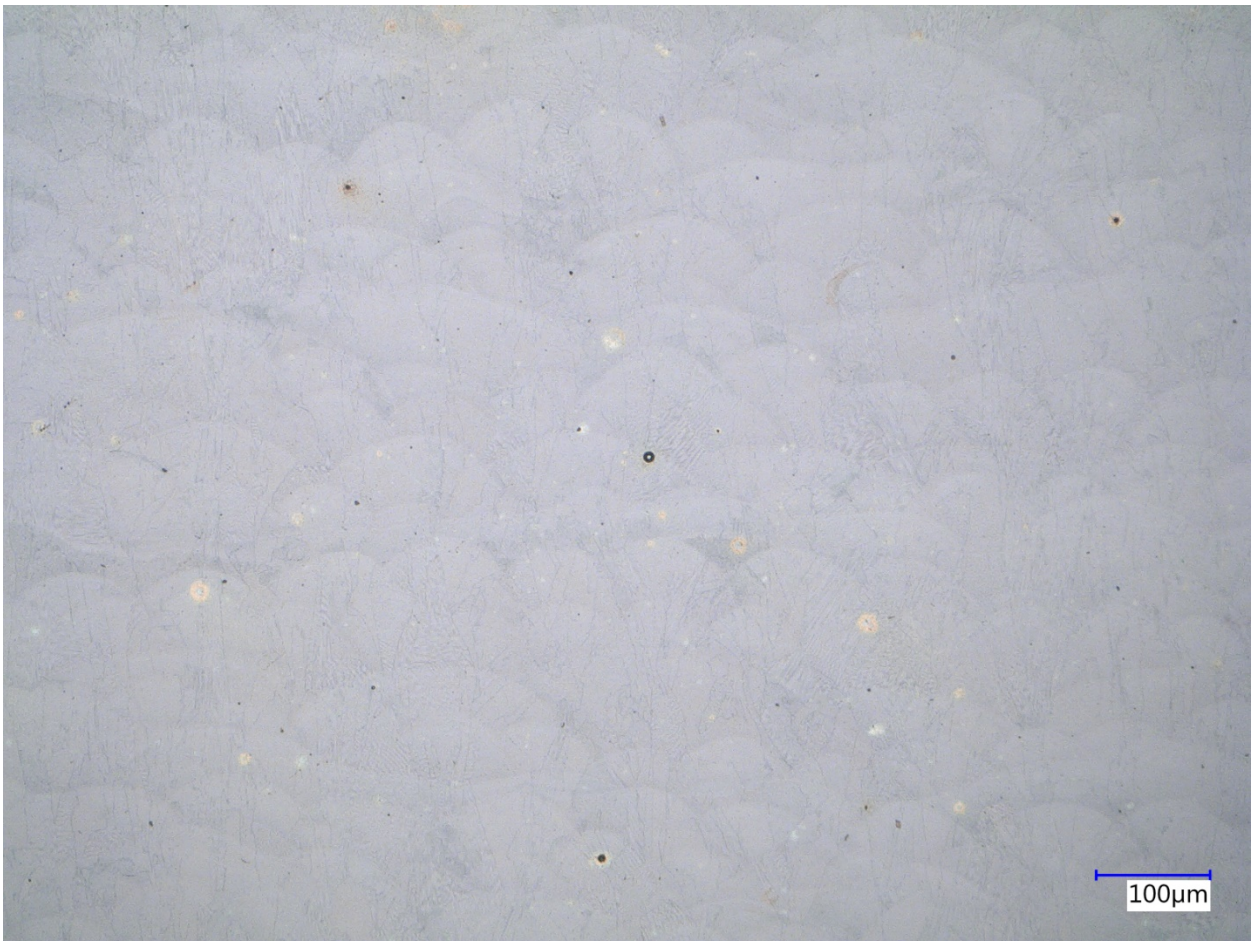

Figure 23. Optical micrograph of as-built LPBF H282, with the BD going toward the top of the page in the image. 200× magnification, oxalic acid etch.

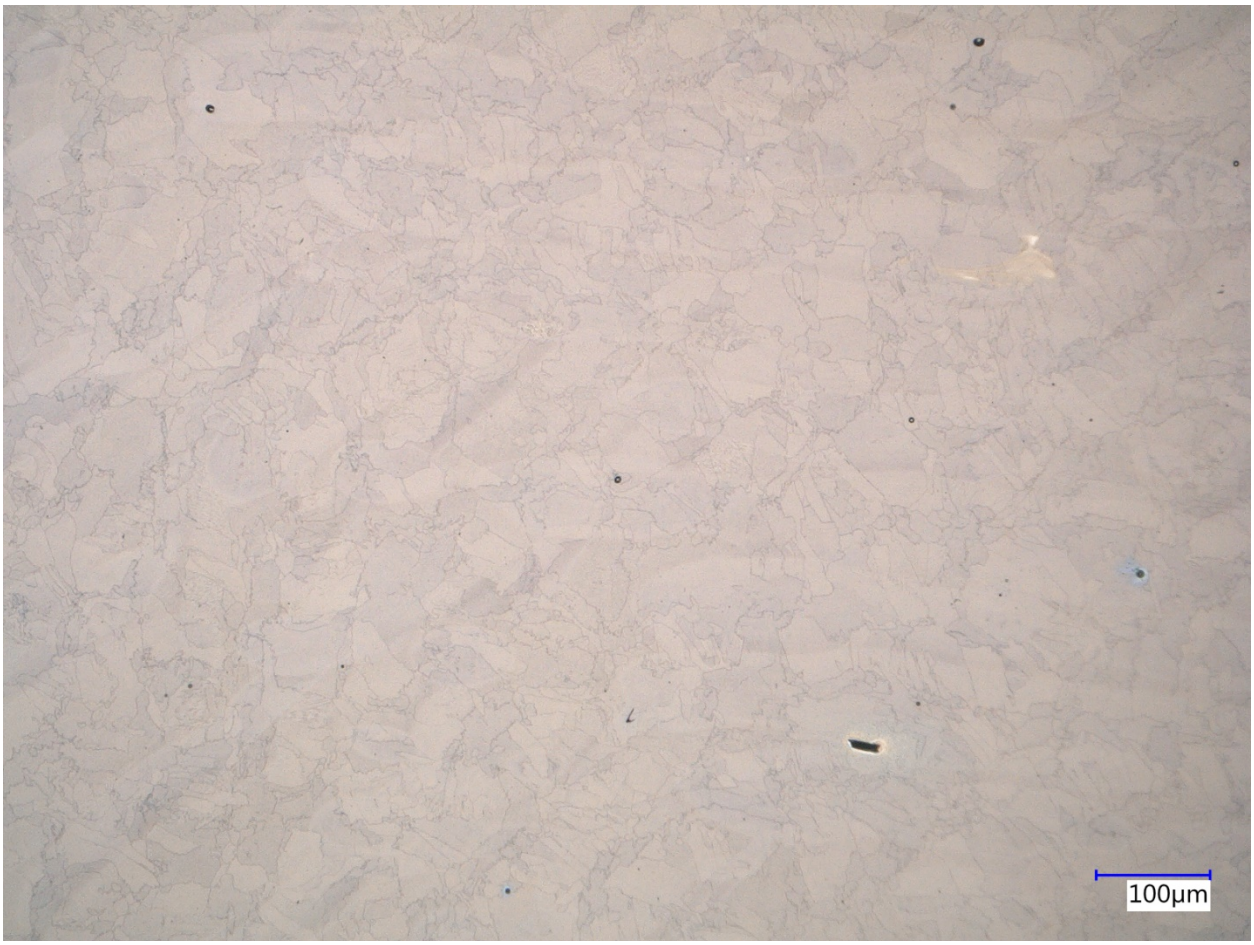

Figure 24. Optical micrograph of as-built LPBF H282, sectioned in the transverse direction.
200× magnification, oxalic acid etch.

In contrast to the as-built microstructure, Figure 25 shows an optical micrograph of the H282 sample aged at 1,210°C for 2 h. In this case, the grains appear roughly equiaxed and much larger. Annealing twins are also visible.

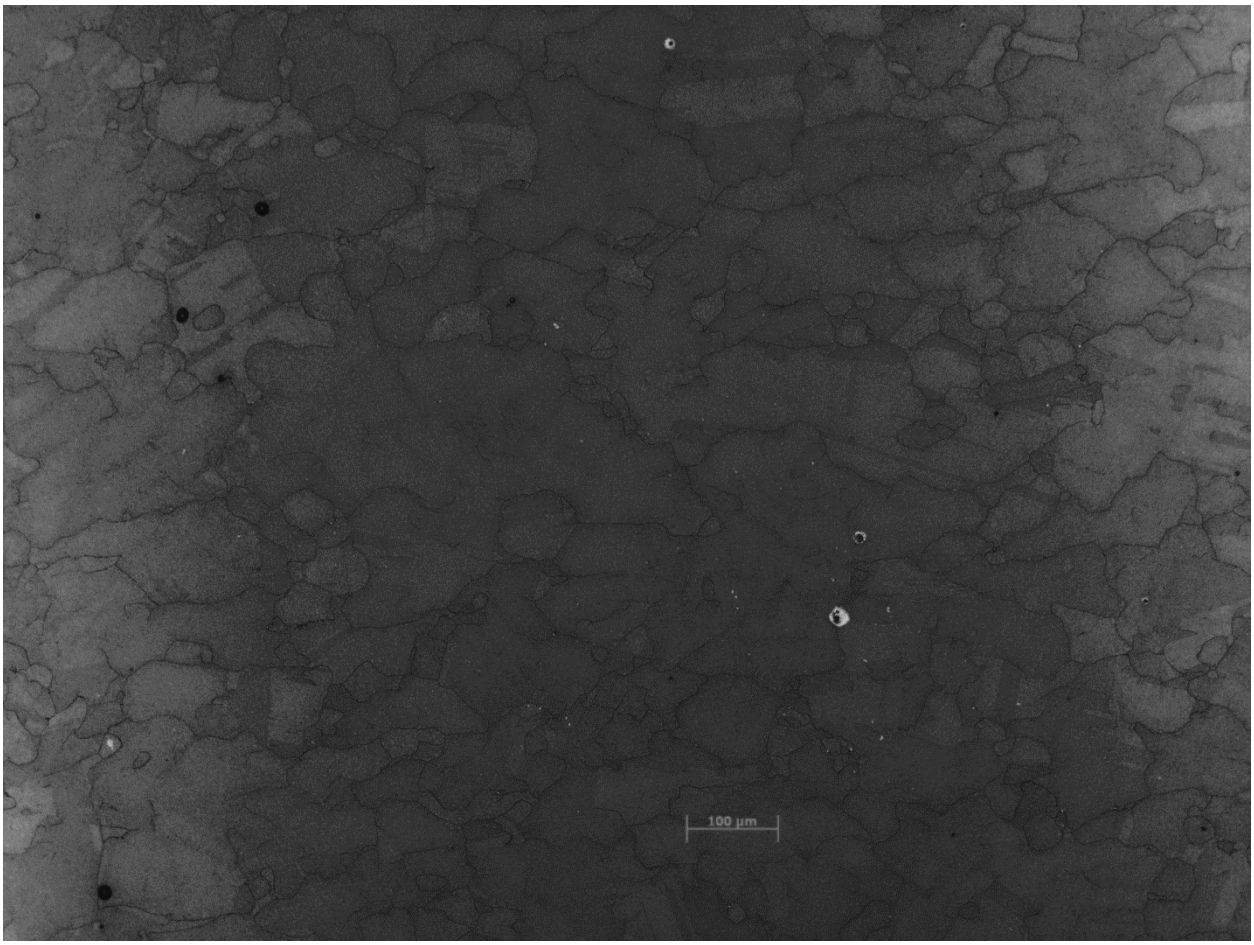

Figure 25. Optical micrograph of LPBF H282 heat-treated at 1,210°C for 2 h, with the BD going toward the top of the page in the image. 100× magnification, oxalic acid etch.

Figure 26 shows a scanning electron microscopy (SEM) image of the as-built microstructure using backscattered electron (BSE) imaging. The elongated grains are visible here. Elemental microsegregation of elements such as chromium is also evident as variations in the gray scale intensity of the image. Cellular microstructure is evident in Figure 26. A higher magnification image of an area of cellular microstructure is also displayed in Figure 27. To more accurately quantify the grain size, EBSD analysis was performed on the various samples. Figure 28 shows an EBSD inverse pole figure (IPF) map of the as built H282.

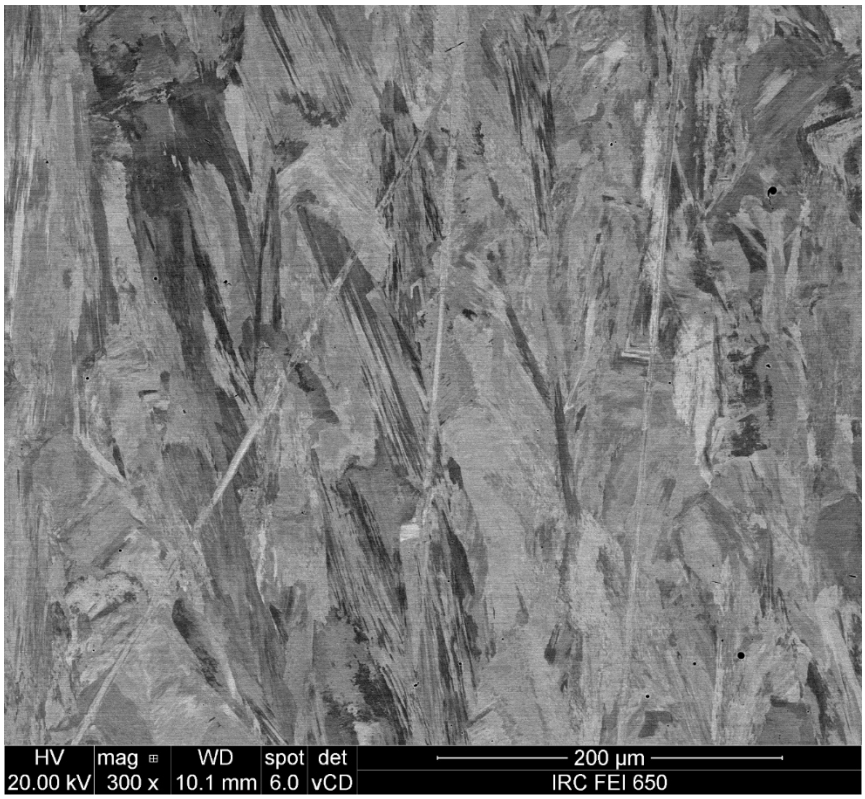

Figure 26. BSE-SEM image of as-built LPBF H282, with the BD going toward the top of the page.

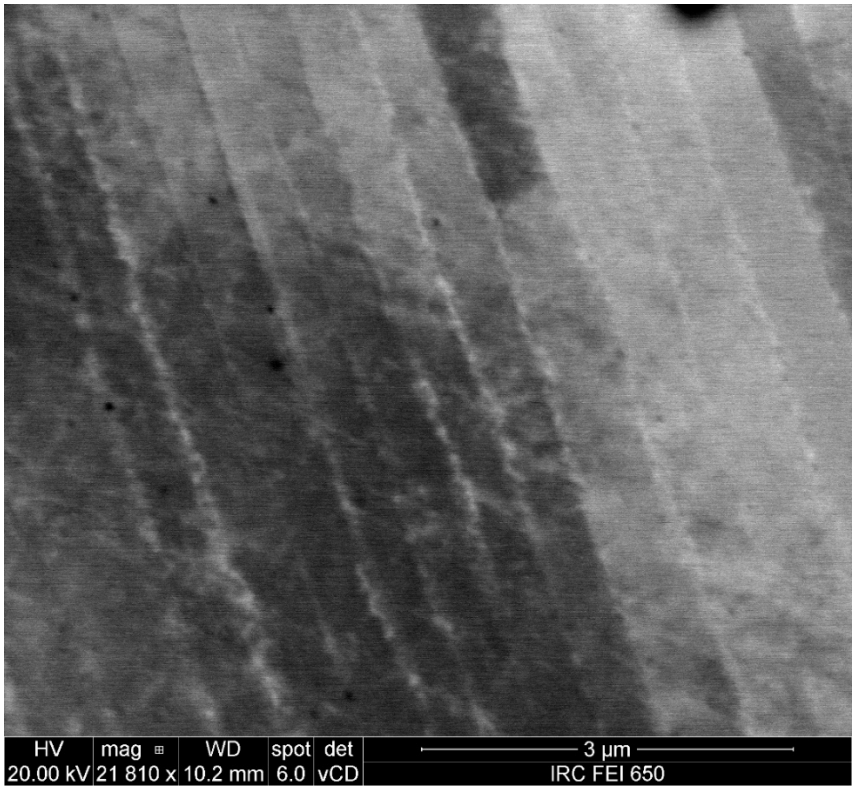

Figure 27. Higher magnification BSE-SEM image of cellular microstructure.

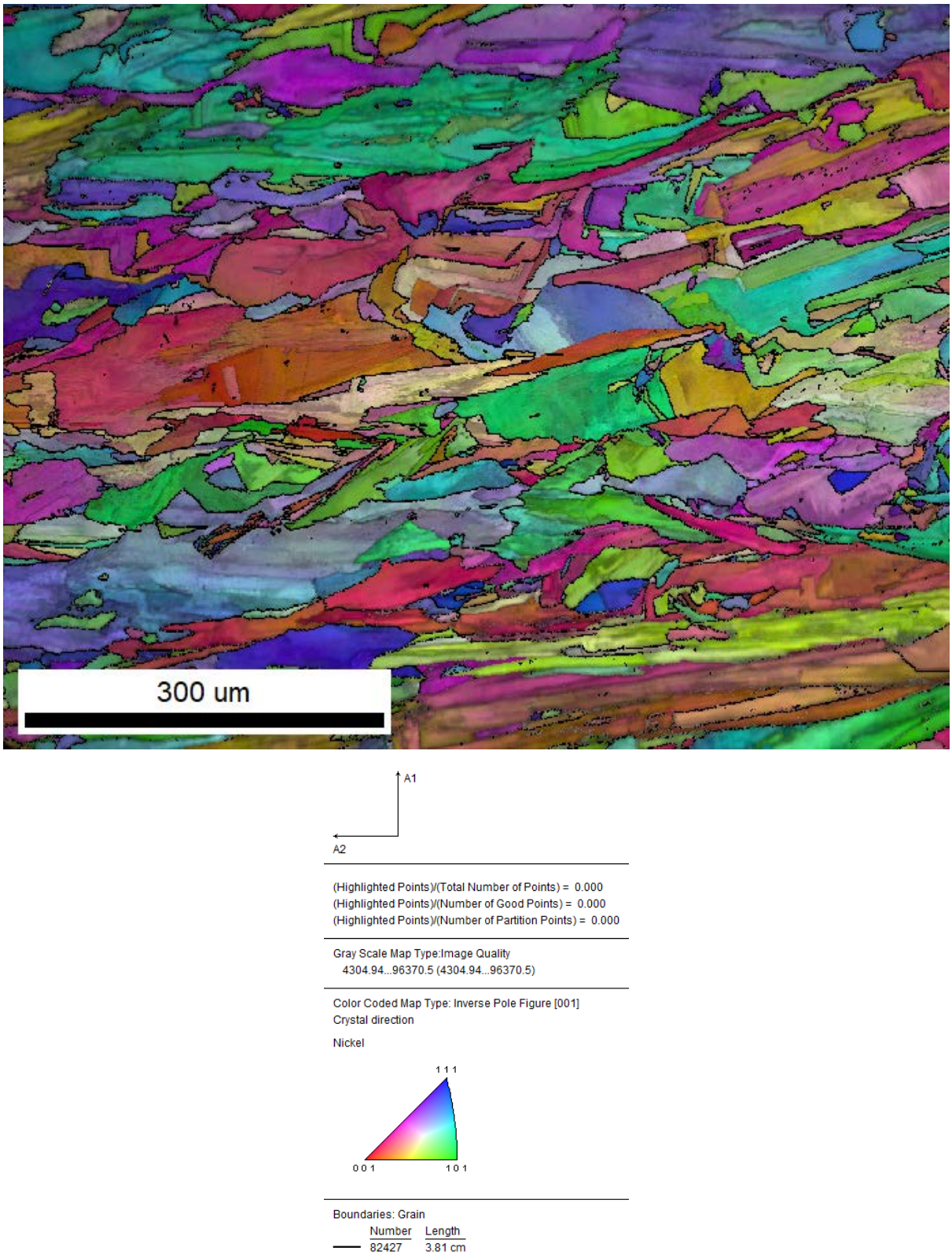

Figure 28. EBSD IPF map of as-built LPBF H282, with the BD going toward the right.

Figure 29 shows the IPF corresponding to the EBSD map. The IPF shows that that the grains are textured with the [001]-type planes parallel to the BD, as expected. However, some textural variation exists, and not all grains conform exactly to that orientation relationship.

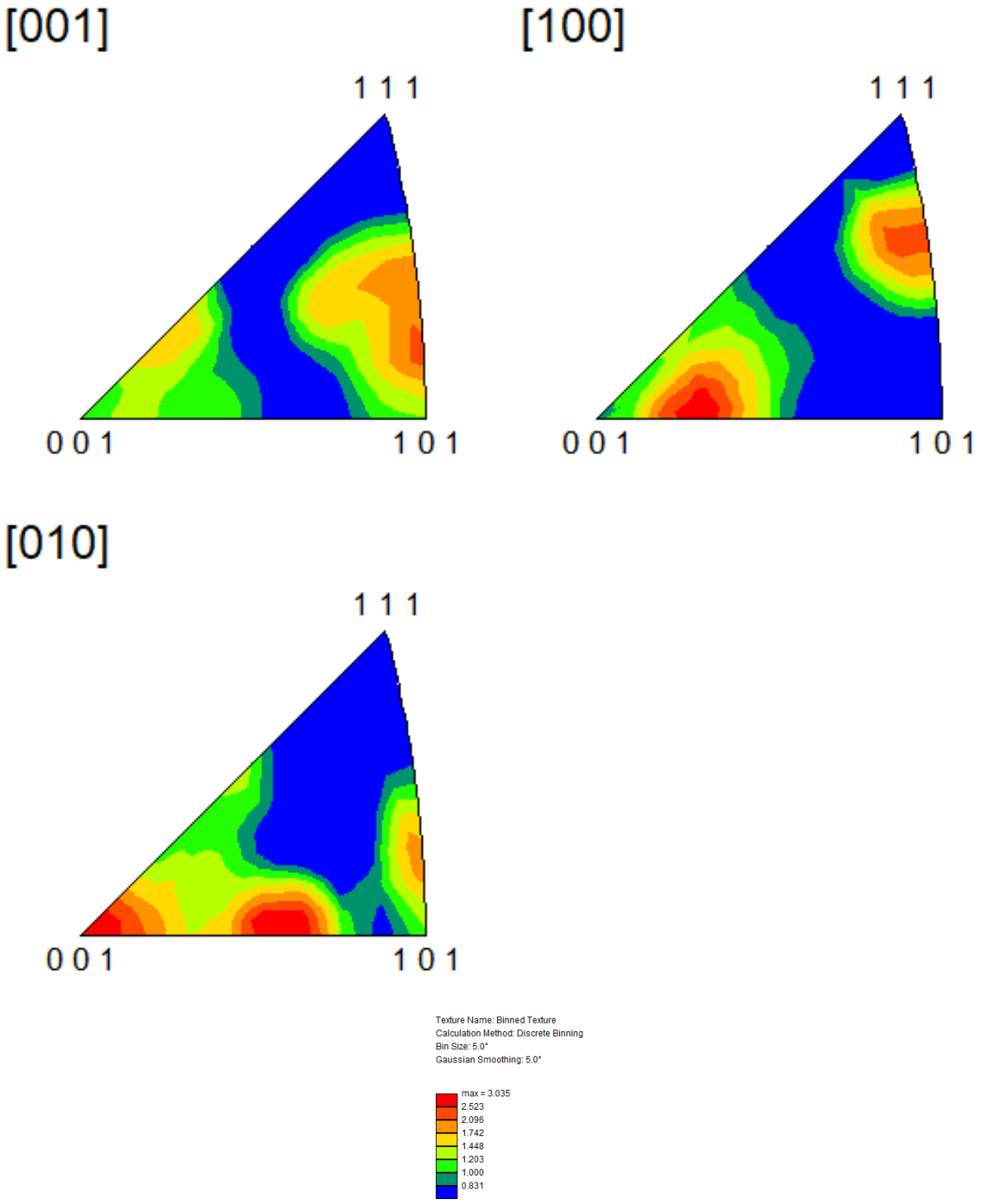

Figure 29. Integrated IPF corresponding to the same scanned area as Figure 28.

Figure 30 shows an IPF map of the sample that was heat-treated at 1,100°C for 1 h. Similar to the observations of [81,99,116], the figure shows that the microstructure is still elongated in the BD and not recrystallized.

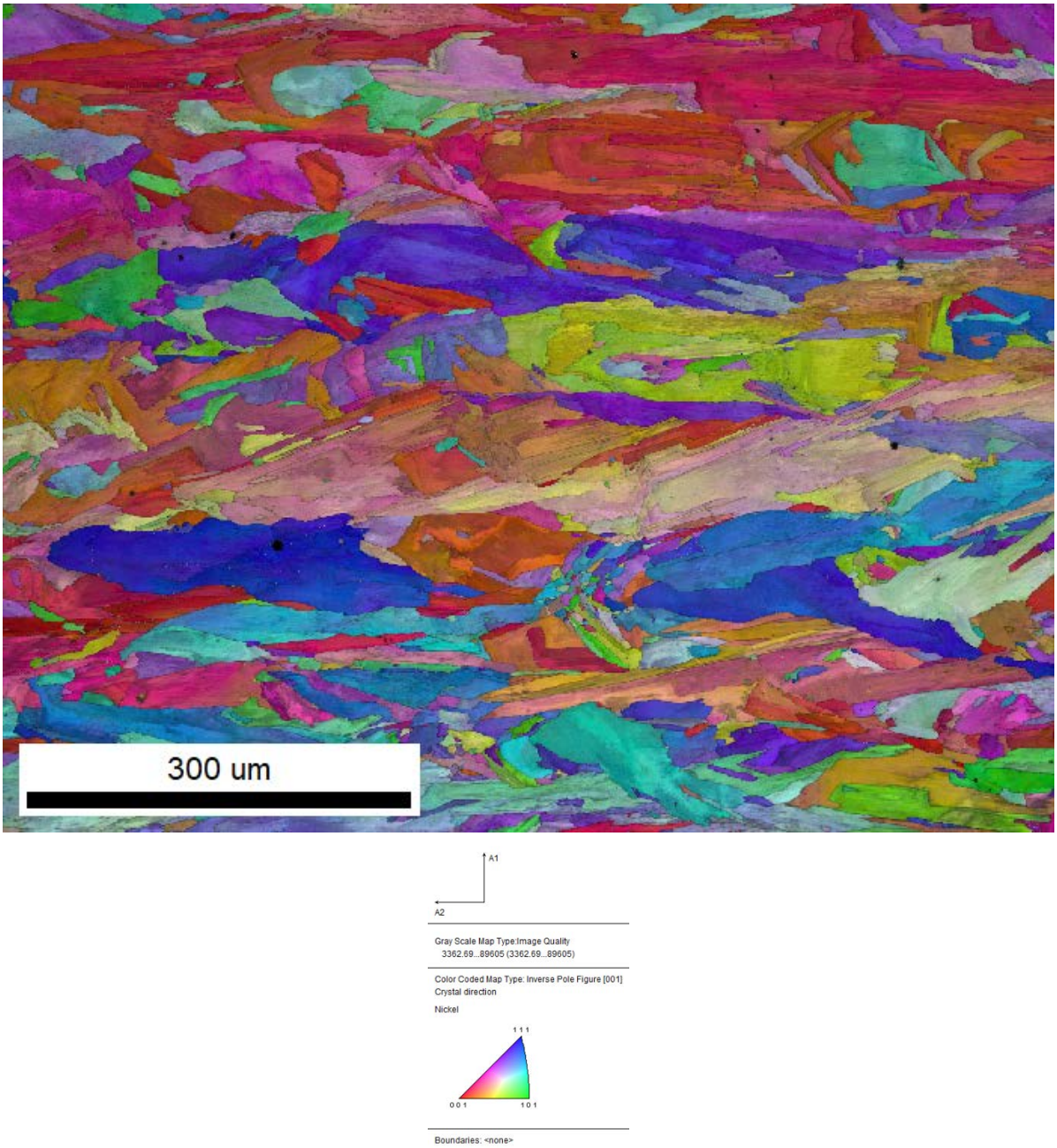

Figure 30. EBSD IPF map of LPBF H282 heat-treated at 1,100°C for 1 h, with the BD going toward the right.

Figure 31 shows an IPF map of LPBF H282 after heat treatment at 1,180°C for 1 h. In this case, the majority of the grains are clearly recrystallized. Some small areas of elongated grains still exist, and some hazy grains indicate varying intragranular orientations characteristic of remnant cellular structure. Annealing twins are also visible in many grains.

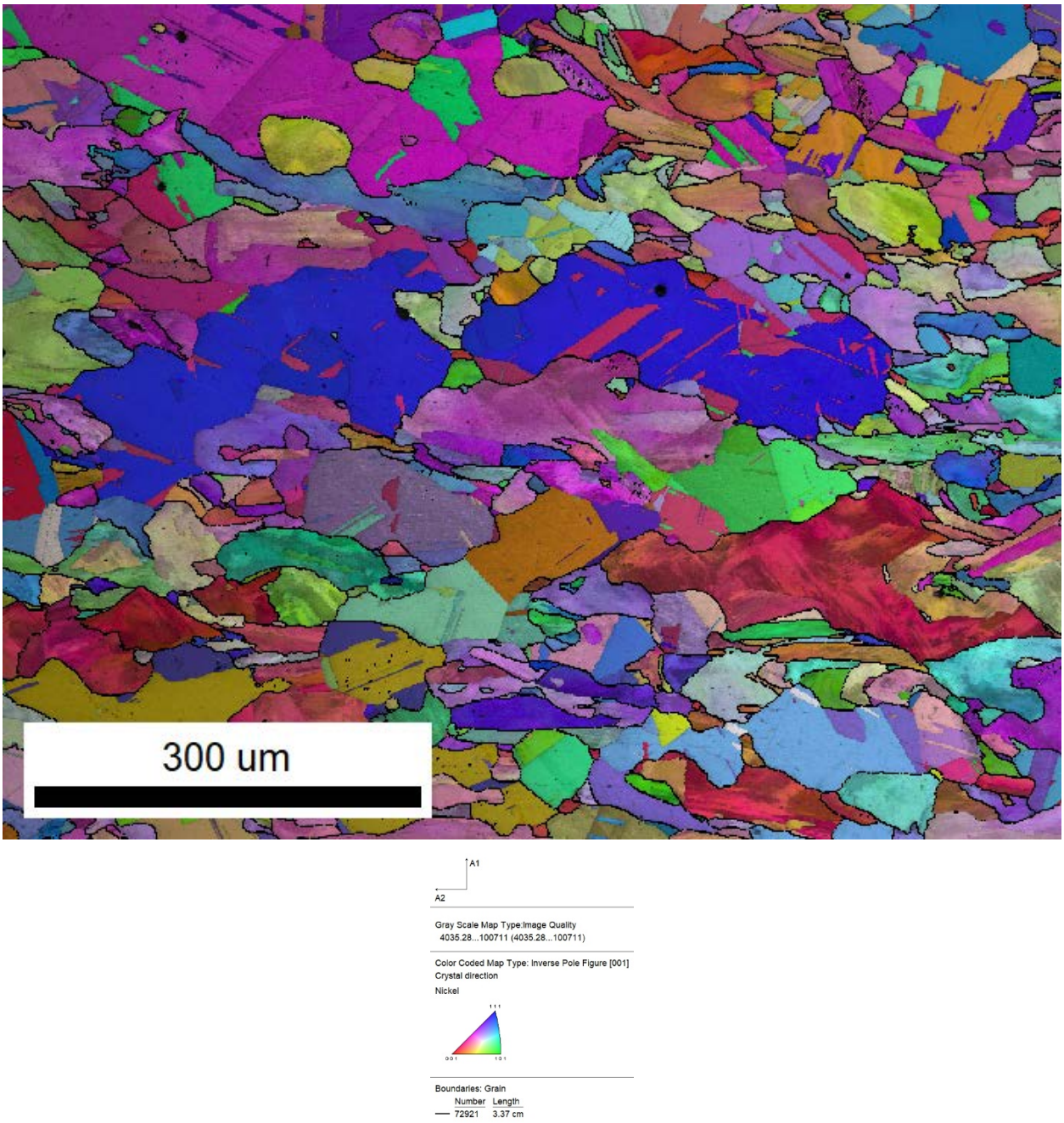

Figure 31. EBSD IPF map of LPBF H282 heat-treated at 1,180°C for 1 h, with the BD going toward the right.

Figure 32 shows an EBSD IPF map of the LPBF H282 sample heat-treated at 1,210°C for 2 h. The grain size is much larger than that after the 1,180°C heat treatment, and much larger annealing twins are also visible. A few hazy grains are still present, indicating remnants of the cellular structure.

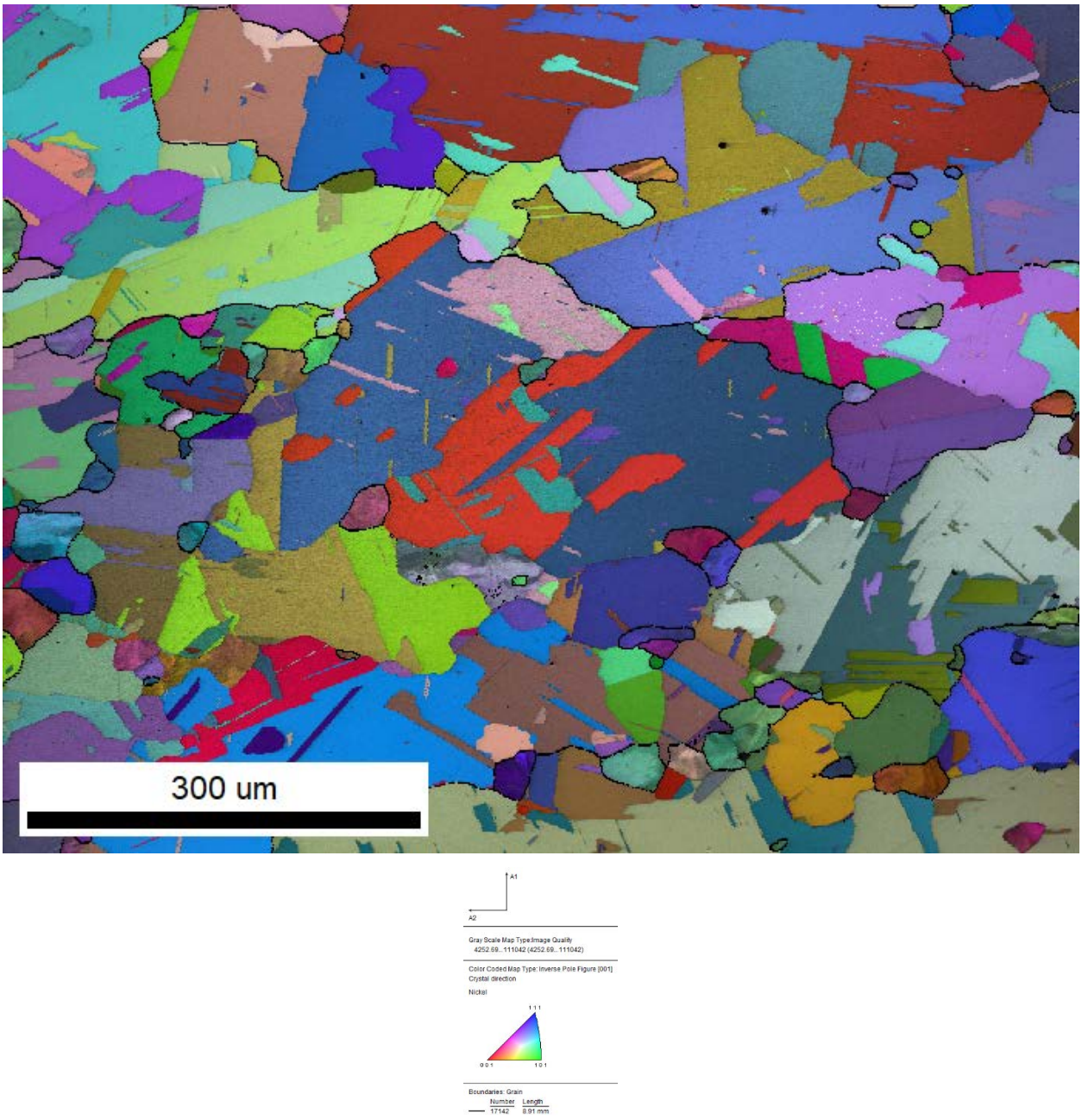

Figure 32. EBSD IPF map of LPBF H282 heat-treated at 1,210°C for 2 h, with the BD going toward the right.

Figure 33 shows an EBSD IPF map of the LPBF H282 sample heat-treated at 1,250°C for 2 h. The grain size is large and similar to the size of the sample heat-treated at 1,210°C for 2 h. The area occupied by annealing twins appears to be larger after the 1,250°C heat treatment. A few small hazy areas, indicating remnant cellular microstructure, are present even after this heat treatment.

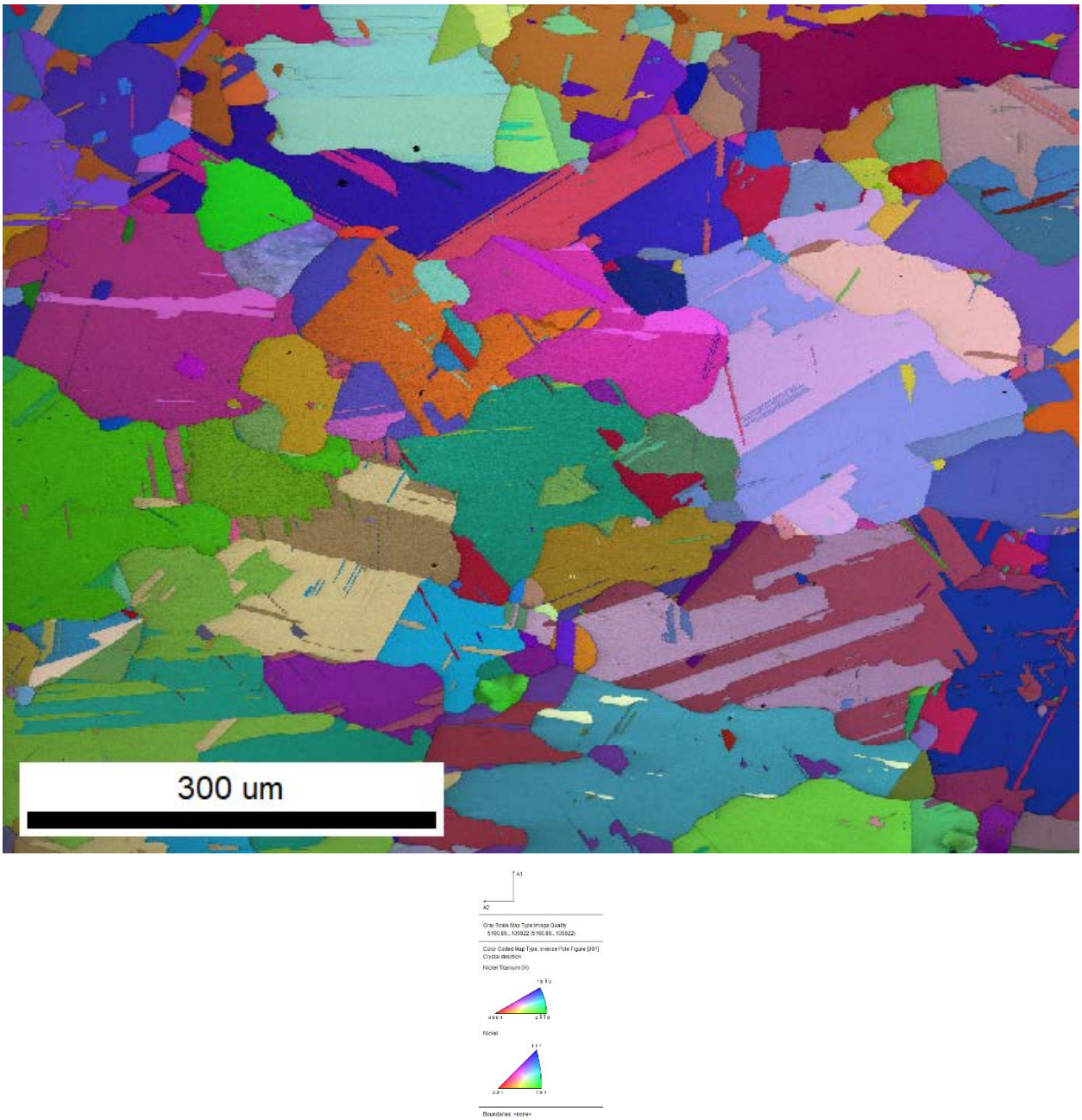

Figure 33. EBSD IPF map of LPBF H282 heat-treated at 1,250°C for 2 h, with the BD going toward the right.

Figure 34 shows the average grain size calculated from the EBSD analysis. Grains are defined by 15° of misorientation, and twin boundaries are excluded from the analysis. Each grain size is an average of four scans, and the area-weighted average grain diameter is used.

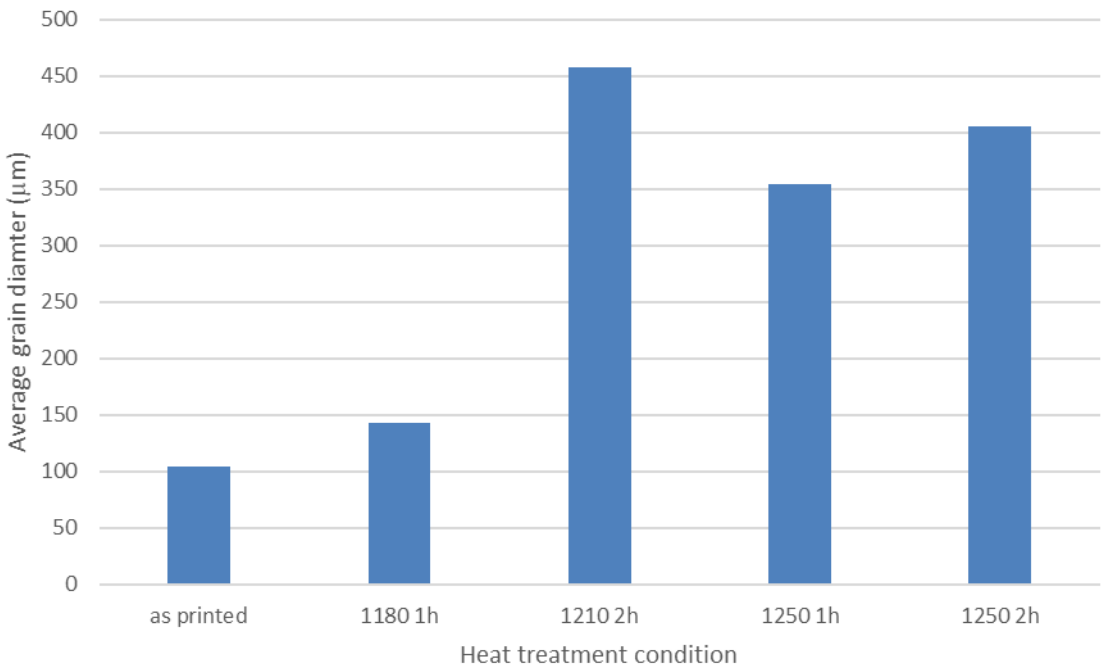

Figure 34. Average grain size calculated from EBSD scans of various heat treatments.

To obtain a good balance of creep and fatigue properties, a grain size of approximately 100 µm was identified as desirable. The heat treatment that produced the closest recrystallized grain size to this value is 1,180°C for 1 h, which produces an average grain size of 144 µm, as shown in Figure 34. In an attempt to produce a smaller recrystallized grain size, two additional heat treatments were performed at 1,180°C for 0.5 h and 1,160°C for 1 h. EBSD IPF maps of the corresponding microstructures in the BD are shown in Figure 35 and Figure 36, respectively. Both microstructures are partially recrystallized. Certain recrystallized grains appeared to nucleate and grew quickly, and large parts of the microstructure remained unrecrystallized. It was therefore decided that 1,180°C for 1 h should be used as the solution heat treatment because it produced nearly complete recrystallization while achieving a slightly larger grain size than what was targeted.

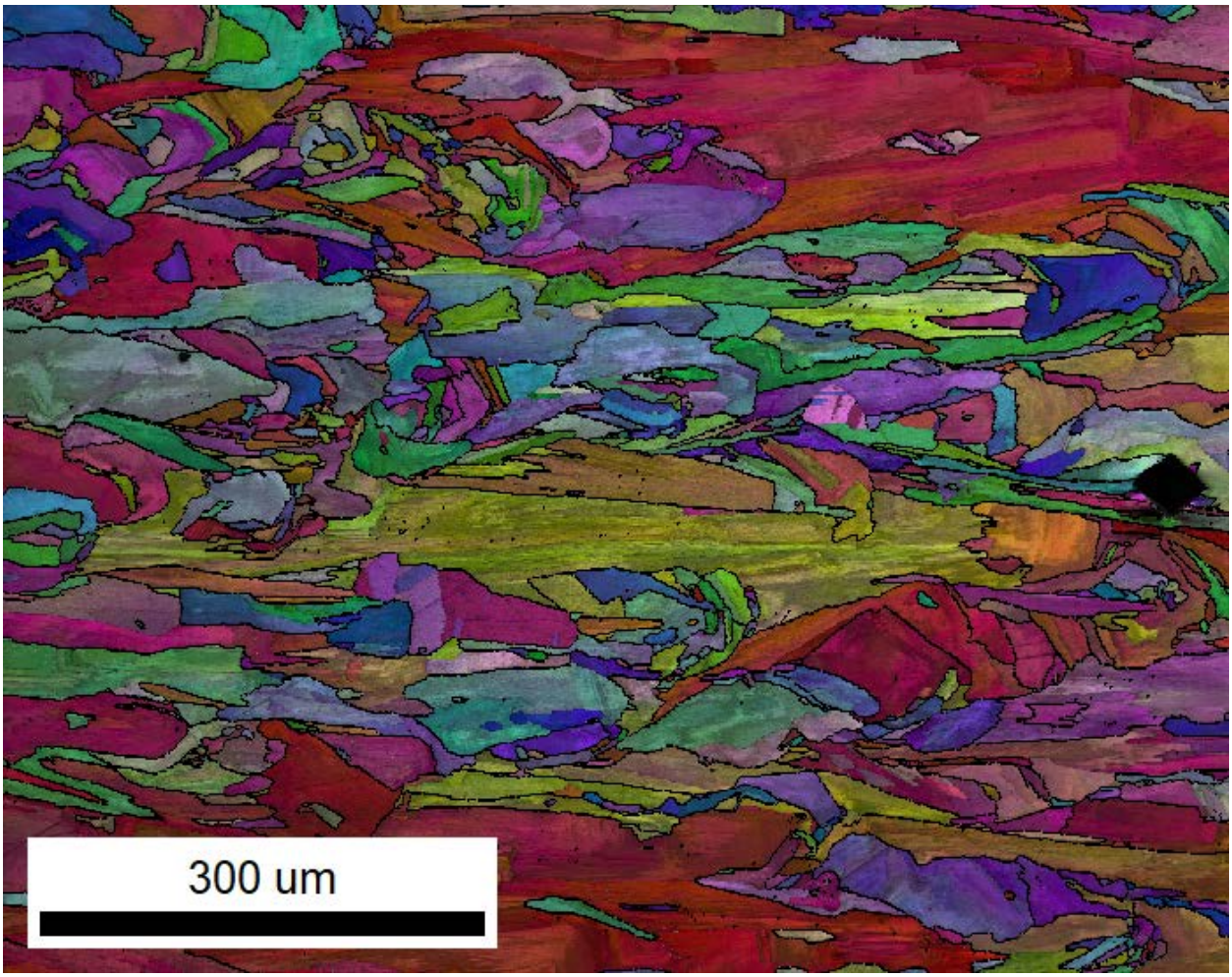

Figure 35. EBSD IPF map of LPBF H282 heat-treated at 1,180°C for 0.5 h, with the BD going toward the right.

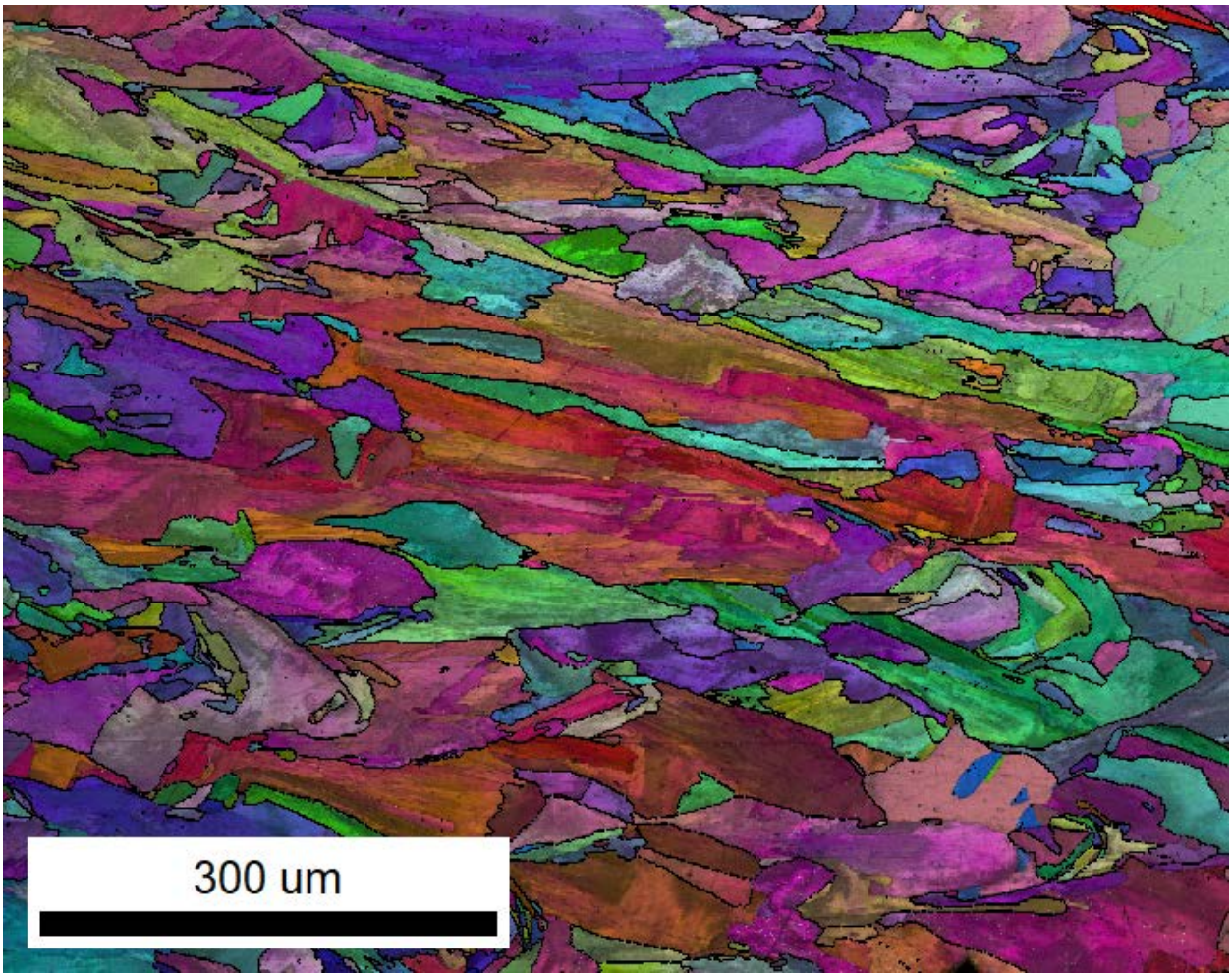

Figure 36. EBSD IPF map of LPBF H282 heat-treated at 1,160°C for 1 h, with BD going toward the right.

5. EVALUATION OF IRON-BASED ALLOYS

A total of six alloys— three austenitic stainless steels (A709, D9, and alumina- forming austenitic [AFA]) and three ferritic/martensitic steels (HT9, Grade 91, Grade 92). —were downselected by ANL and PNNL for printing feasibility studies on 3D printed blocks and microstructural characterization whereas initial single-track experiments were performed on one alloy class each (A709 for austenitic and Grade 91 for ferritic/martensitic) to optimize the process parameters for full 3D printed blocks. The following section gives a brief overview of the alloys considered.

5.1 AUSTENITIC STAINLESS STEELS

5.1.1 A709 (NF 709)

First developed by the British in 1950s, the 20Cr25Ni/Nb SS has been used as a fuel cladding material for the British Advanced Gas-cooled Reactor (AGR) fleet since 1962 [117]. Approximately 90,000 fuel pins were present in each AGR plant, and there were 14 plants constructed and operated. Although the creep strength of 20Cr25Ni/Nb was relatively low, it was sufficient for its intended application. Based off this information, in the 1980s, the Nippon Steel Corporation modified the base chemical composition by adding boron, molybdenum, and titanium to 20Cr25Ni/Nb to strengthen the creep resistance for ultra-

supercritical boilers. The resulting austenitic SS was trademarked *NF 709* [118]. The design criteria for developing the composition of NF 709 were to have a stable austenite devoid of the σ and other intermetallic phases under long-term, elevated-temperature service conditions and creep-strengthened by a metal carbonitride M(CN) precipitated in a stable, fine dispersion. Through a DOE Office of Nuclear Energy Advanced Reactor Technologies material downselection and intermediate term testing program, Alloy 709, an advanced austenitic SS alloy, was recommended as a class A structural material for the sodium-cooled fast reactor because of its overall superior structural strength advantage [119–120]. Although extensive work has been performed on A709 in the wrought form to have it code-qualified, no literature is available on the AM aspect. The scorecard of A709 is given in Table 9.

Table 9. Scorecard for all A709

Category	Criteria and corresponding ranking					
Manufacturing/ powder	Powder availability: 1	Powder properties: 2	Powder chemistry: 2	Cost: 4	Recycling: 1	—
Manufacturing/ components	Printability (LPBF): ND	Defects: ND	Post-treatment: ND	Processing window: ND	Weldability: 2	Surface roughness or finish: 2
History and applications	NE experience: 4	Other industry experience: 4	Data availability: 4	Code data availability: 4	Experience with non-LPBF AM: 2	Scaling up: 2
Mechanical properties	Creep: 4	Fatigue: 2	Creep-fatigue: 4	High-temperature tensile strength: 4	Room temperature: 2	—
Environmental effects	Radiation resistance: 3	Oxidation resistance: 3	Stress corrosion cracking: N3	Molten salt: ND	Liquid metal: ND	—
Physical properties	Thermal properties: 2	Solidification-relevant properties: 2	Other modeling-relevant properties: ND	CT-relevant properties: ND	—	—
Microstructure	Material homogeneity: 2	Microstructure stability: 3	LPBF microstructure specificity: ND	—	—	—
ND: not determined						

5.1.2 D9 (Titanium-Modified Stainless Steel)

The D9 alloy is a titanium-modified, 316 SS that has provided improved resistance to neutron irradiation–induced void swelling as compared with the unmodified 316 SS [121–123]. The addition of titanium in the matrix is crucial for binding a portion of the dissolved carbon in the form of tiny TiC precipitates. It is believed that the TiC matrix interfaces serve as sinks for radiation-induced point defects and enhance the swelling resistance [124]. The formation of chromium carbides is also reduced, thus improving the overall corrosion resistance. Most of the work on the bulk form of D9 was done in the early 1990s. Recently, there have been few publications on the effect of the addition of titanium to SSs via DED. The alloying here was done in situ (i.e., titanium was added independently). The addition of titanium to 316 SS was noted to refine the grains and increase the overall TSs [125–126]. Currently, there are no available data on the LPBF of D9 alloy.

5.1.3 Alumina-Forming Austenitic Stainless Steels

Although ferritic SSs possess excellent corrosion resistance, they fail to maintain the same mechanical strength as austenitic SSs. Introducing hard nano-oxide particles into the ferrite matrix via powder metallurgy routes improves the mechanical properties; such a class of ferritic steels is known as ODS steels [127, 128]. Alternatively, introducing specific alloying elements can enhance the corrosion or oxidation resistance of the austenitic SSs. ORNL successfully developed a new class of austenitic SSs known as alumina-forming austenitic (AFA) SSs, or *AFA alloys* [129–131]. The AFA alloys exhibit excellent high-temperature creep resistance up to 900°C and superior corrosion resistance in dry and humid air environments. Although the creep resistance and corrosion resistance of the AFA alloys are improved by the formation of various strengthening precipitates, including NbC and $M_{23}C_6$ carbides, Laves phase, and γ′, the oxidation resistance is mainly enhanced by the formation of protective aluminum-rich oxide scale. Despite being beneficial, aluminum and chromium additions are kept low as they stabilize the ferritic phase; any precipitation of ferritic phase at operational temperatures might result in poor creep resistance [129]. AFA alloys exhibit complex microstructures with different types of precipitates within the grain interiors and along the grain boundaries. The AFA scorecard is displayed in Table 10.

Table 10. Scorecard for AFA alloy

Category	Criteria and corresponding ranking					
Manufacturing/ powder	Powder availability: 3	Powder properties: 4	Powder chemistry: 4	Cost: 4	Recycling: 4	—
Manufacturing/ components	Printability (LPBF): 4	Defects: 4	Post-treatment: 3	Processing window: 3	Weldability: 3	Surface roughness or finish: 4
History and applications	NE experience: 1	Other industry experience: 3	Data availability: 3	Code data availability: 0	Experience with non-LPBF AM: 2	Scaling up: 3
Mechanical properties	Creep: 4	Fatigue: 4	Creep-fatigue: 4	High-temperature tensile strength: 2	Room temperature: 3	—
Environmental effects	Radiation resistance: 2	Oxidation resistance: 4	Stress corrosion cracking: 4	Molten salt: ND	Liquid metal: ND	—
Physical properties	Thermal properties: 3	Solidification-relevant properties: 4	Other modeling-relevant properties: 2	CT-relevant properties: ND	—	—
Microstructure	Material homogeneity: 3	Microstructure stability: 3	LPBF microstructure specificity: 2	—	—	—
ND: not determined						

5.2 FERRITIC/MARTENSITIC STEELS

5.2.1 HT9

Sandvik HT9 was the first ferritic/martensitic steel considered in the US Fusion Materials Program when the program decided to investigate these steels as structural materials for the first wall and blanket

structures of fusion reactors [132]. The rich, irradiated materials database on HT9 has prompted commercial startup companies such as TerraPower LLC to revitalize the manufacturing of HT9 [133]. The adequate in-core performance of HT9 has also been demonstrated by its successful applications as fuel cladding and ducts in the Fast Flux Test Facility. The most critical issue that may limit the usage of HT9 in future nuclear energy systems is its irradiation embrittlement at low temperatures. A significant shift in ductile-to-brittle transition temperature (DBTT) above 120°C can be observed after neutron irradiation below 400°C [134]. ORNL published a series of papers on the additively manufactured HT9, but all the work they did was on the blown powder technique. The characterization showed that the as-built structure essentially consisted of a martensitic matrix with δ-ferrite present in the reheat zones between each pass during the sample fabrication process [135–137]. The martensitic matrix consisted of an ultrafine dispersion of carbides and carbonitrides. Currently, no literature is available on the LPBF of HT9 alloy.

5.2.2 Grade 91

Grade 91 steel was developed as a second-generation creep-resistant alloy. ORNL modified the composition by adding small amounts of vanadium and niobium to 9Cr–1Mo to form fine carbonitrides [137]. Broadly used in fossil and nuclear power plants in components operating at temperatures up to approximately 650°C, it is the current *workhorse* alloy and the only alloy being studied in the current work package that is included in the ASME *Boiler and Pressure Vessel Code*, Section III, Division 5 [138]. Having a chromium concentration of 9 wt % gives very good creep strength while having a minimal increase in the DBTT. Significant work has been performed recently on the AM of Grade 91 steel. Blown powder, wire DED, and LPBF-based techniques have all been used to fabricate this alloy to understand the microstructural evolution, mechanical behavior, corrosion, and, in some cases, even irradiation behavior [139–142]. In the case of the LPBF sample, as-deposited additively manufactured Grade 91 steel had a microstructure of lower bainitic regions surrounded by martensite. The as-deposited additively manufactured material had excellent tensile properties, with greater strength than the wrought material at room and elevated temperatures, showing excellent promise for nuclear applications. Retention of strength at 300°C and 600°C for the as-deposited additively manufactured material was attributed to transitional carbides in the lower bainitic regions [143–144]. The scorecard for the Grade 91 alloy is given in Table 11.

Table 11. Scorecard for Grade 91 alloy

Category	Criteria and corresponding ranking					
Manufacturing/ powder	Powder availability: 2	Powder properties: 3	Powder chemistry: 4	Cost: 4	Recycling: 2	—
Manufacturing/ components	Printability (LPBF): 4	Defects: 3	Post-treatment: 3	Processing window: 4	Weldability: 4	Surface roughness or finish: 3
History and applications	NE experience: 4	Other industry experience: 3	Data availability: 4	Code data availability: 4	Experience with non-LPBF AM: 2	Scaling up: 3
Mechanical properties	Creep: 4	Fatigue: 3	Creep-fatigue: 4	High-temperature tensile strength: 4	Room temperature: 4	—
Environmental effects	Radiation resistance: 4	Oxidation resistance: 3	Stress corrosion cracking: 4	Molten salt: 3	Liquid metal: 3	—

Table 11. Scorecard for Grade 91 alloy (continued)

Category	Criteria and corresponding ranking					
Physical properties	Thermal properties: 3	Solidification-relevant properties: 3	Other modeling-relevant properties: ND	CT-relevant properties: ND	—	—
Microstructure	Material homogeneity: 4	Microstructure stability: 4	LPBF microstructure specificity: 3	—	—	—
ND: not determined						

5.2.3 Grade 92

To improve the creep properties of second-generation Grade 91 alloy, Grade 92 steel was developed as a third-generation creep-resistant ferritic/martensitic steel with the addition of tungsten and minute amounts of boron. Although Grade 92 has been reported to have better creep properties relative to Grade 91, it has not been code-qualified [138]. In practice, the microstructure is made up of a tempered martensitic lath structure, which is stabilized by chromium-rich $M_{23}C_6$ carbide, an intralath MX-type of niobium and vanadium carbonitrides, martensite phase transformation induced high dislocation density, and solid solution strengthening from tungsten [145–147]. The presence of tungsten in the $M_{23}C_6$ precipitate decreases the growth rate of the precipitate during creep exposure, which in turn increases the stability of the martensitic lath structure of the steel on creep exposure. Currently, no research is available on the AM of Grade 92 steel.

6. ONGOING CHARACTERIZATION OF IRON-BASED ALLOYS

6.1 EXPERIMENTAL DETAILS

6.1.1 Fabrication Technique

A Renishaw AM400 LPBF machine equipped with a reduced build volume was used to fabricate all the samples. The machine is equipped with a ytterbium-fiber pulsed laser with a maximum power of 400 W and a beam diameter of 70 μm. To optimize the process parameters, single-track experiments were performed on two of the alloys: an austenitic SS (A709) and a ferritic/martensitic steel (Grade 91). In total, 72 parameter sets were initially planned for these systems. Laser power, exposure time, and point distance were varied. The parameters of A709 were based on the literature review and from Renishaw (based on SS 316L). The recommended condition from Renishaw is highlighted with a star in Figure 37. The parameters for Grade 91 were based on literature review, experimental evidence from Los Alamos National Laboratory (LANL), and from Renishaw (based on 17-4 PH steel). The process parameters are shown in Figure 37, and a fully processed single-track image is shown in Figure 38. Based on this study, a total of 10 block samples with different processing conditions were built for each of the six alloys depending on the alloy class (i.e., austenitic SSs vs. ferritic/martensitic steels). The process parameters are in Table 12, Table 13, and Table 14. The powders were manufactured by the company Atlantic Equipment Engineers using argon gas atomization in 15–20 kg batches. The compositions of the powders are listed in Table 15 and Table 16. Each sample was printed to be a 10 × 10 × 10 mm cube.

6.1.2 Characterization Technique

Once the samples were printed, they were sectioned along the BD to study the microstructure. Standard metallography techniques were employed to polish the samples for optical and electron microscopes. Samples were polished with 4,000 grit SiC abrasive paper, followed by a diamond suspension (3 μm and 1 μm) and by a 0.05 μm colloidal silica suspension final polish in a Buehler Vibromet. The samples for single-track experiments were etched with a mixture of 30 mL H_2O, 30 mL HCl, and 10 mL HNO_3 to reveal the melt pool. Optical microscopy was done on a Keyence VHX-970F digital microscope. Three micrographs were taken for each sample (60 samples overall) and were analyzed in ImageJ to calculate the porosity. X-ray diffraction (XRD) scans were performed using a D8 Discover equipped with copper Kα radiation, 1.6 W maximum power (40 mA and 40 V), as well as a custom-built sample stage. All the scans were collected in a 10°–105° 2θ range using a 0.005° step size and 0.05 seconds per step scanning rate. JEOL 7500 SEM was used for electron microscopy, EBSD, and EDS. A JEOL Grand Arm scanning transmission electron microscope (STEM) with a Schottky field emission gun operated at 300 keV was used for further characterization of samples microstructure. Conventional bright-field (BF), high-resolution, and high-angle annular dark-field (HAADF) TEM/STEM imaging with selected area electron diffraction were used in this study. High-resolution elemental mapping was also acquired using EDS in STEM mode. Fast Fourier transformation was also used in some instances as another characterization tool. An area representative of lower, middle, and upper parts of samples in their BD was selected for microhardness testing consisting of 64 indents using a test load of 300 gram force (gf) with a duration of 12 s. All microhardness testing was performed using a Micro Hardness Tester CM-802AT from Sun-Tec Corporation.

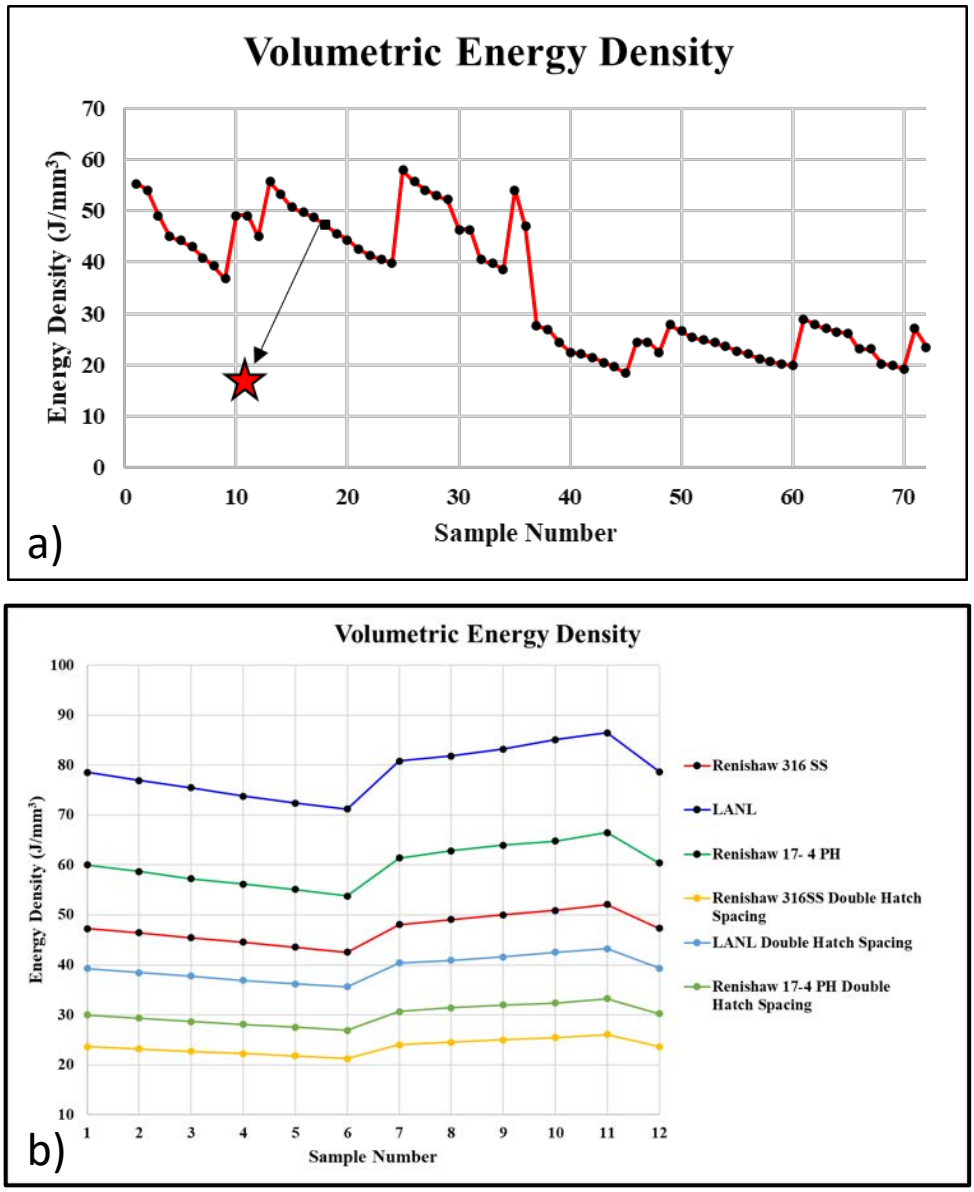

Figure 37. Volumetric energy densities used for single-track experiments for (a) A709 and (b) Grade 91.

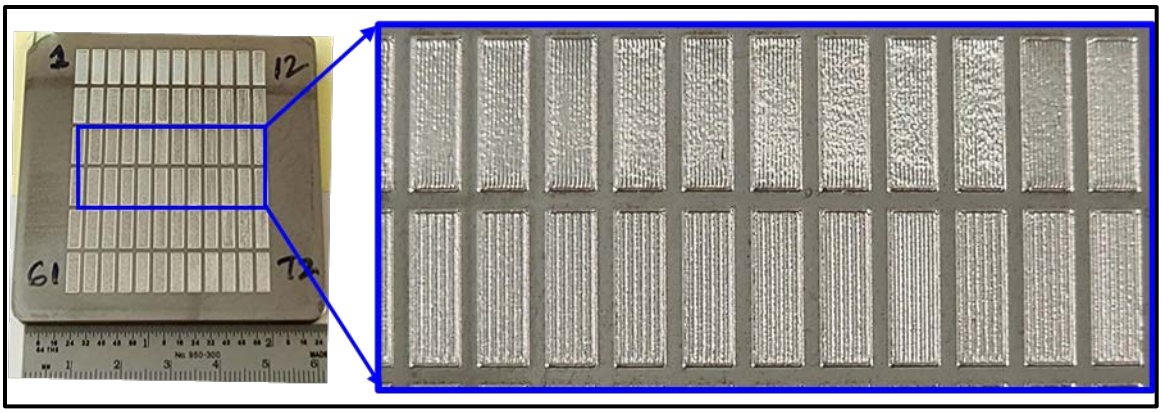

Figure 38. Single-track experiments on A709 alloy. In the highlighted image, the top layer shows single hatch spacing, and the bottom has double hatch spacing.

Table 12. Process parameters for Fe–Cr–Al

Sample number	Laser power (W)	Point distance (µm)	Exposure time (µs)	Hatch spacing (µm)	Energy density (J/mm^3)	Density (g/cm^3)
3	275	80	60	100	82.5	6.99
9	315	80	60	100	94.5	7.15
12	315	160	60	100	178.5	7.16

Table 13. Optimized process parameters for austenitic SSs for the block build

Sample	Laser power (W)	Exposure time (µs)	Hatch space (µm)	Point distance (µm)	Layer thickness (µm)	Energy density (J/mm^3)
1	195	70	110	50	50	49.63
2	195	110	110	80	50	48.75
3	195	80	110	60	50	47.27
4	195	90	110	70	50	45.58
5	195	100	110	80	50	44.31
6	215	90	110	70	50	50.25
7	215	100	110	80	50	48.86
8	215	60	110	50	50	46.90
9	215	70	110	60	50	45.60
10	215	80	110	70	50	44.67

Table 14. Optimized process parameters for ferritic/martensitic steels for the block build

Sample	Laser power (W)	Exposure time (µs)	Hatch space (µm)	Point distance (µm)	Layer thickness (µm)	Energy density (J/mm^3)
1	221	101	110	55	50	73.78
2	185	101	110	45	50	75.49
3	270	80	110	50	50	78.54
4	200	100	110	45	50	80.80
5	305	75	110	50	50	83.18
6	165	105	110	55	50	57.27
7	220	62	110	45	50	55.11
8	180	110	110	60	50	60
9	200	95	110	55	50	62.80
10	225	95	110	60	50	64.77

The final compositions of the powder obtained from the company Atlantic Equipment Engineers are listed in the following tables.

Table 15. Chemical composition of Austenitic SS alloys (wt %)

Alloy	Fe	Cr	Ni	Mn	Mo	C	N	Si	Ti	Nb	Al
D9 Steel	Bal.	13.7	14.9	1.9	2.2	0.04	n/a	0.6	0.26	n/a	n/a
AFA	Bal.	12.7	19.2	0.03	2.18	0.02	n/a	0.4	n/a	0.78	2.3
A709	Bal.	20	25.4	0.91	1.51	0.06	0.16	0.44	0.04	0.26	n/a

Bal.: balanced

Table 16. Chemical composition of ferritic/martensitic alloys (wt %)

Alloy	Fe	Cr	Mo	Mn	W	V	Nb	C	Ni	Si	N
HT9	Bal.	12	1	n/a	0.5	0.25	n/a	0.2	n/a	0.21	n/a
Grade 91	Bal.	8.3	0.9	0.43	n/a	0.2	0.06	0.1	0.17	0.42	n/a
Grade 92	Bal.	8.7	0.5	0.45	1.9	0.2	0.07	0.09	n/a	0.14	n/a

Bal.: balanced

6.2 RESULTS

6.2.1 Single-Track Experiments

The idea behind performing single-track experiments was to optimize the process parameters while waiting on the powders. In total, 72 different processing conditions were used for each of the alloy systems (i.e., A709 for austenitic SSs and Grade 91 for ferritic/martensitic steels). Figure 39 shows the cross section of A709 for one of the ideal conditions given by Renishaw.

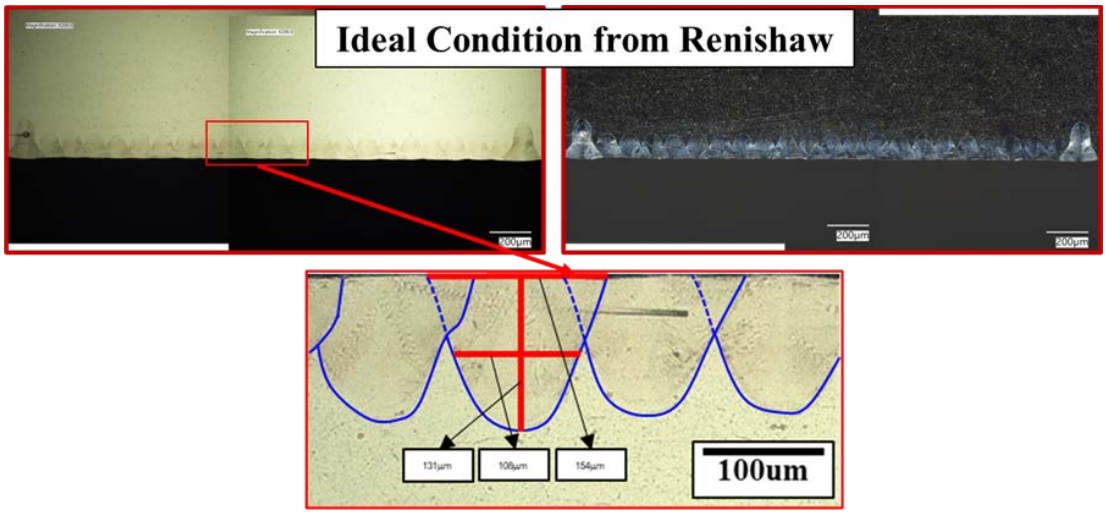

Figure 39. Optical images of cross section showing melt pools in single-track experiments of A709 for recommended processing conditions for 316L SS.

In comparison with the ideal condition for 316L SS provided by Renishaw, another example is shown in Figure 40 where keyhole effects can clearly be observed. Based off these results, processing conditions were narrowed down to 10 for each of the alloy systems.

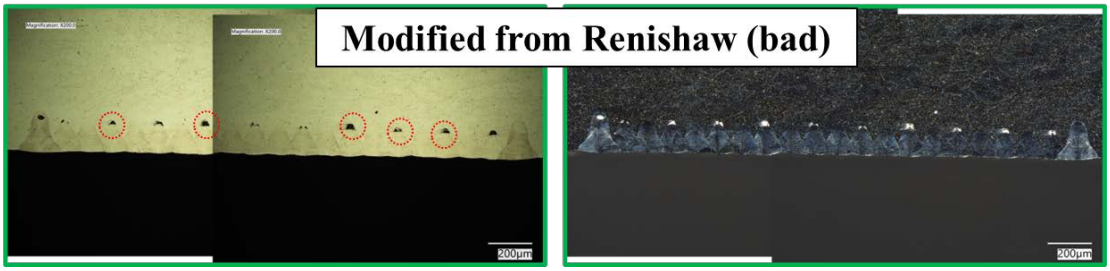

Figure 40. Optical images of cross section showing melt pools in single-track experiments of A709 for modified processing conditions. Red circles show the porosity in the samples.

6.2.2 Full Builds

The results from each alloy will be presented following the same structure. A small introduction about the powders will be followed by optical imaging, showing porosity and other possible defects, and then by scanning electron microscopy showing high magnification microstructures and electron backscattered diffraction images.

6.2.2.1 Austenitic Stainless Steels

D9 (Titanium-Modified Stainless Steel)

Figure 41 shows the as received D9 powder with a higher magnification image shown in the inset. The powder can be seen to be spherical, though a few planetary powders can be seen. This form of powder typically has a high packing density because the small voids in the large particles are filled by the small particles, and it also optimized the fluidity and stacking density, which is very suitable for AM [148].

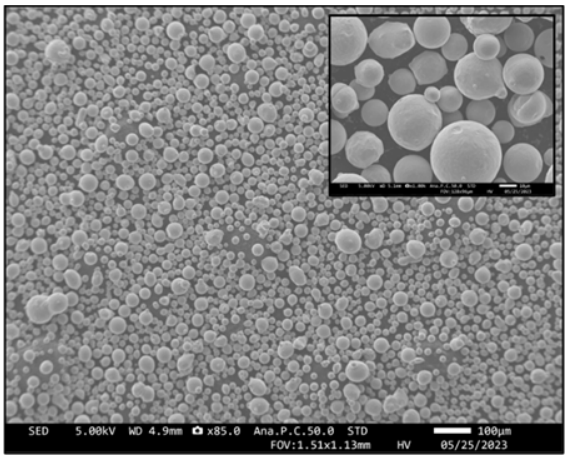

Figure 41. SEM image showing the spherical D9 powder.

Following the deposition, the samples were sectioned in half, and the microstructures were observed along the BD. Although optical imaging was done for all 10 samples, for concision, Figure 42 shows a few select conditions. A high number of cracks exist along the grain boundaries parallel to the BD. Most of the cracking observed here is along the grain boundaries, with a very minimal amount noted in the interiors. Notably, during the deposition of D9 and AFA (which will be discussed in next section), a vacuum leak occurred in the Renishaw system, which possibly led to the defects observed in the current microstructures. Researchers are currently investigating further to isolate the issue.

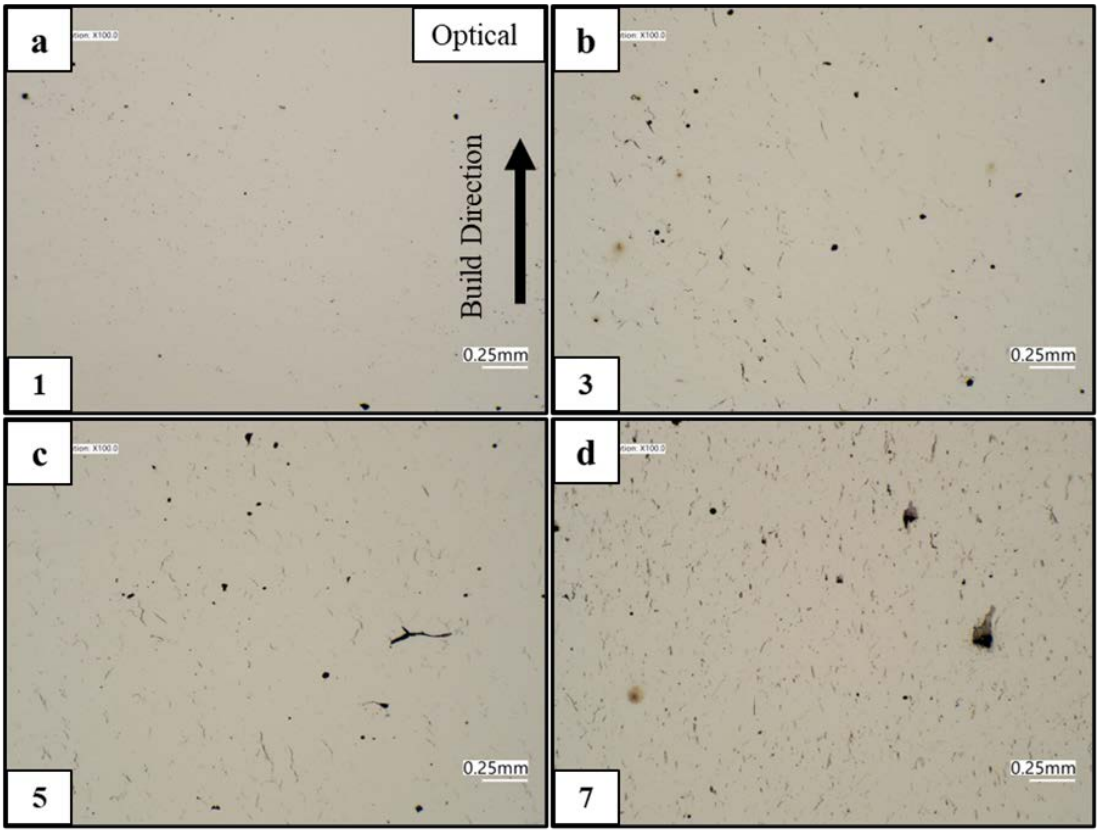

Figure 42. Optical images of four different processing conditions used for D9 alloy. Extensive cracking and other defects can be observed in all the conditions.

Although more work could not be performed owing to the sample conditions, further analysis was still completed via SEM to look at the finer features of the samples. Figure 43 shows the BSE images of sample 3. As expected, the microstructures look very similar to as-deposited SS 316L [149]. At this level of magnification, no TiC was noticed. Figure 43d shows cell structures, which have also been noted in previous works on AM 316L.

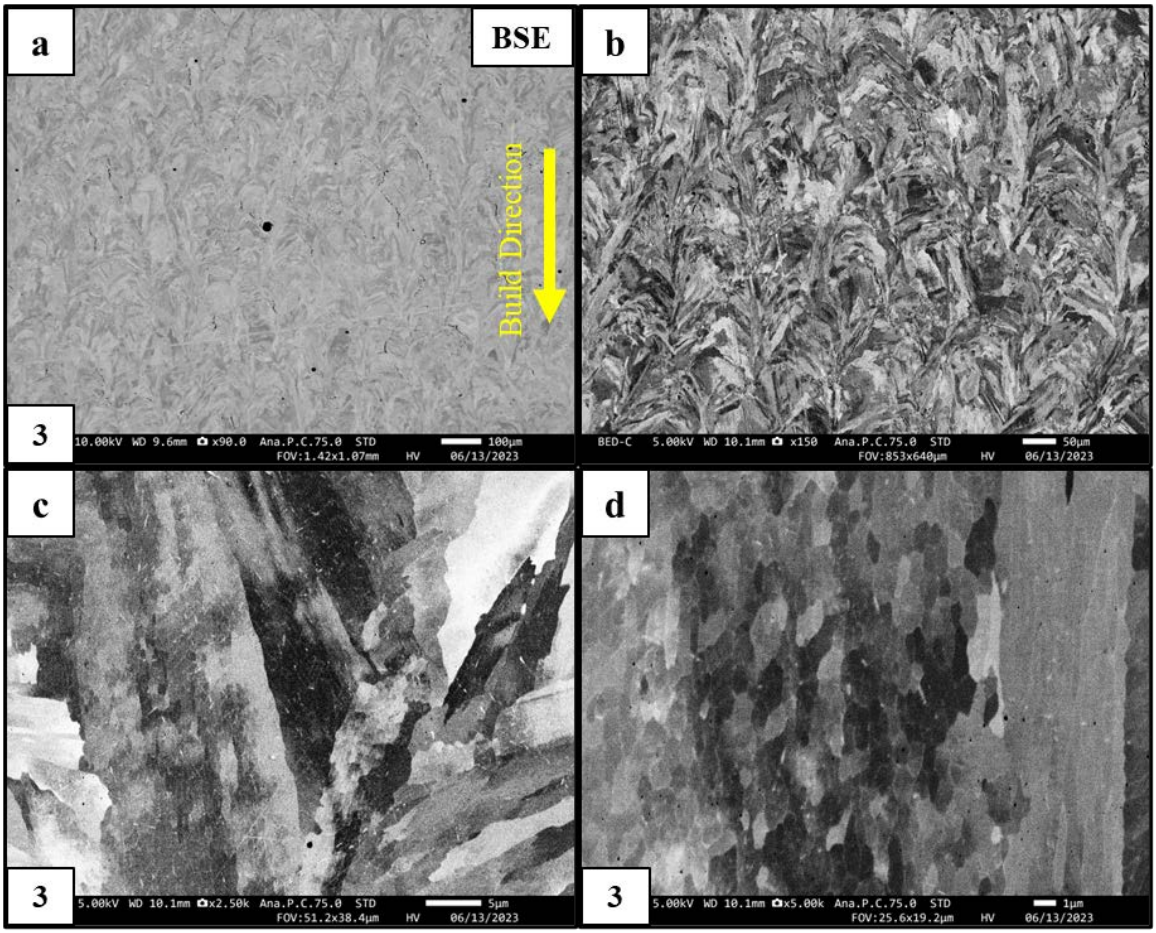

Figure 43. BSE-SEM image showing different features of sample condition 3 for D9 alloy. High-magnification image in (d) shows cell structures noticed in other SS 316 alloys.

The EBSD IPF map (Figure 44) also shows the curved columnar grains. These grains are mostly well-resolved, with a mean grain size of 10.0 ± 10.0 µm within 2.1–74 µm grain size distribution. IPF shows no significant texture (maximum of only ~3× random) in the overall sample area scanned, but slight texture can be observed in isolated areas owing to the pockets of grains present in some areas of the sample. The sample also does not have any significant strain according to the kernel average misorientation (KAM) map.

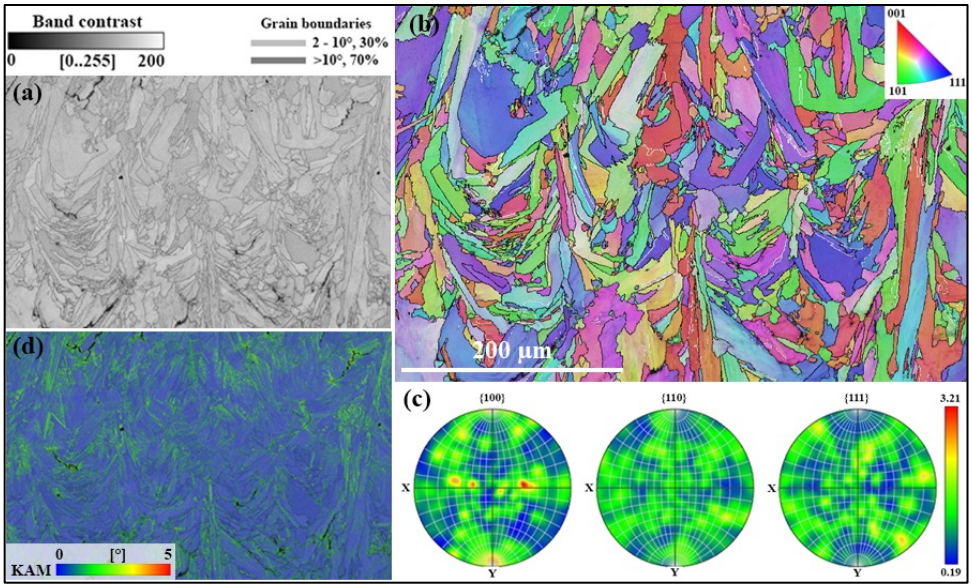

Figure 44. (a) Band contrast (BC), (b) BC + IPF + grain boundary (GB) maps, (c) pole figures (PFs), and (d) KAM + BC map of a center area of the BD surface of D-9 sample #3.

The distribution of the microhardness of the BD surface of D-9 sample #3 is shown in Figure 45, and the optical image of the sample shows the indent locations. As it is observed in the contour and 3D surface maps, hardness values are greater in the center of the sample compared with the sides of the 27.4 mm^2 area tested. A maximum hardness value of 224.7 HV (Vickers hardness) was obtained (indent #36 at $x = 4.7$ and $y = 3.8$ mm) as the highest hardness value, and the average value of the sample is 189.3 ± 16.8 HV.

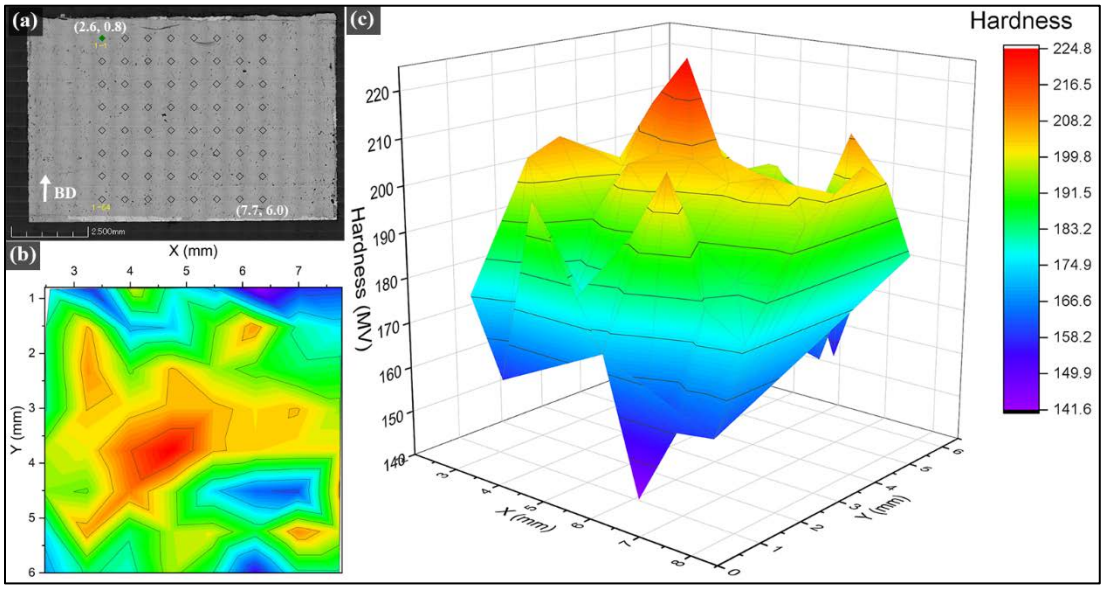

Figure 45. (a) Optical image and microhardness of D9 Sample#3: (b) contour and (c) 3D surface presentations of hardness.

Alumina-Forming Austenitic Alloys

Similar to the D9 steel, AFA powder was also very spherical. Higher magnification imaging on individual powder particles, shown in Figure 46, reveals some artefacts on the powder. More work is currently underway to investigate these particles.

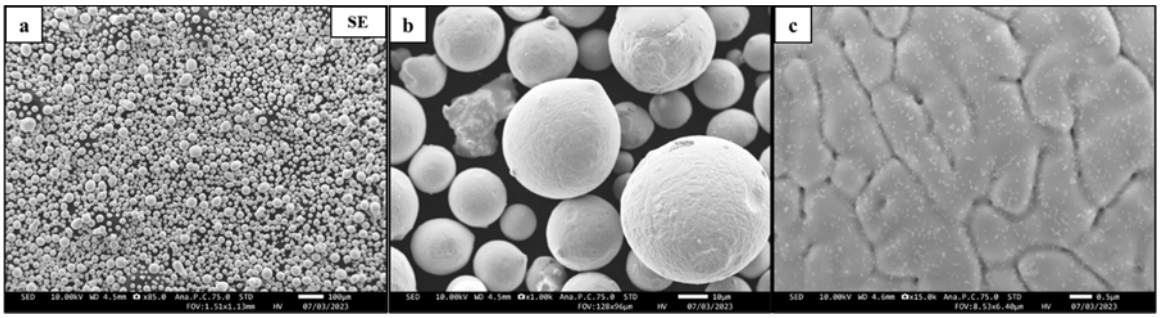

Figure 46. SEM image showing the spherical AFA powders. High-magnification image showing artefacts.

As mentioned previously, significant cracking of the samples was also noted in AFA samples. A few images are shown in Figure 47. The optical images clearly show the cracking along grain boundaries.

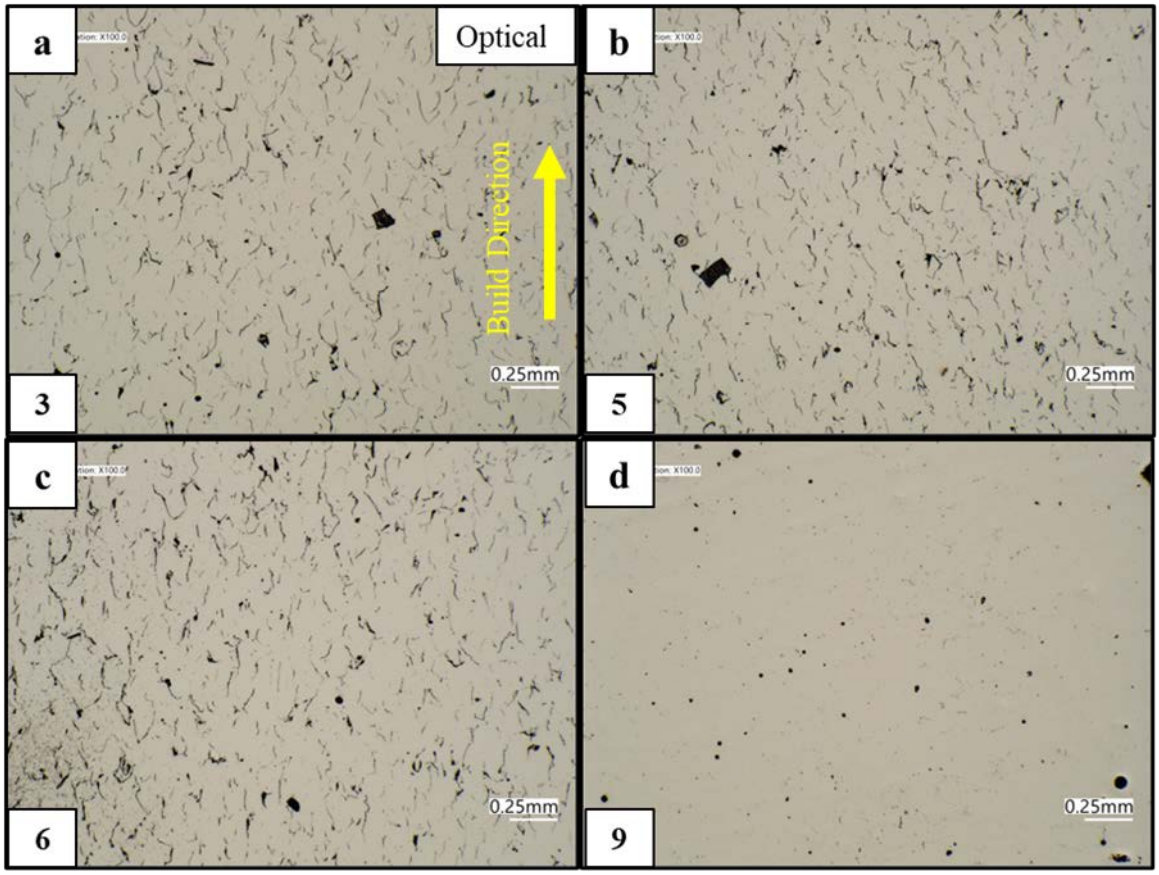

Figure 47. Optical images of four different processing conditions used for AFA alloy. Extensive cracking and other defects can be observed in all the conditions.

AFA sample #9 consisted of randomly distributed columnar grains. Because of some issues with the 3D printer, AFA samples have some microcracks, as highlighted in Figure 48. At high resolution, some randomly distributed dark-contrast precipitates on grains and bright-contrast precipitates along grain boundaries can be observed. EDS analysis was not successful in identifying the elements of these precipitates because they are too small (<1 μm).

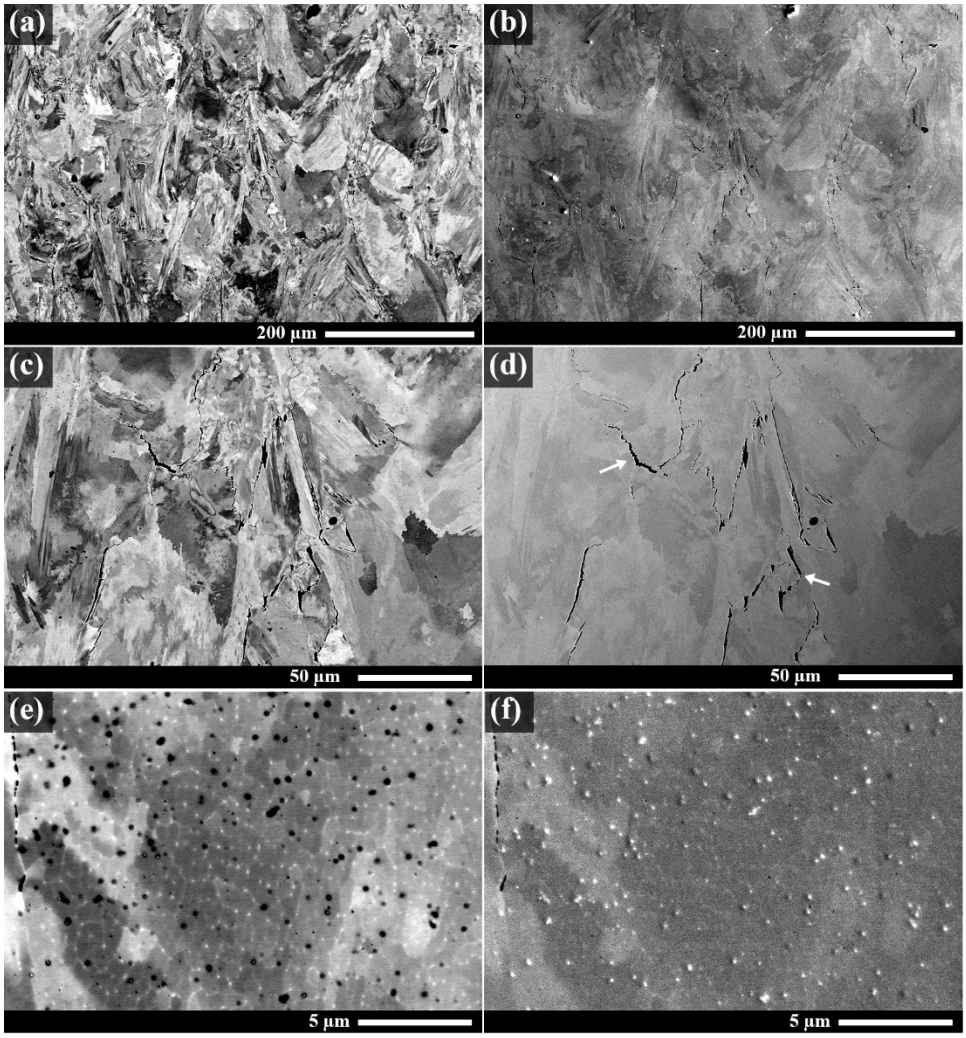

Figure 48. SEM images near the center of the BD surface of AFA sample #9: (a, c, d) BSE-SEM images at a few different resolutions and (b, d, f) their corresponding BSE images. A few microcracks are highlighted by arrows in (d).

The IPF map (Figure 49) also shows the laths observed in the SEM images. A slight texture (maximum of ~7× random) can be observed, especially parallel to {100} planes, as depicted in pole figures (PFs). Some strain, especially in the narrow grains, is also observed in the sample according to the KAM map. A mean grain size of 16.7 ± 17.8 μm with a minimum and maximum of 3.6 and 125.9 μm, respectively, was obtained using EBSD analysis of the sample.

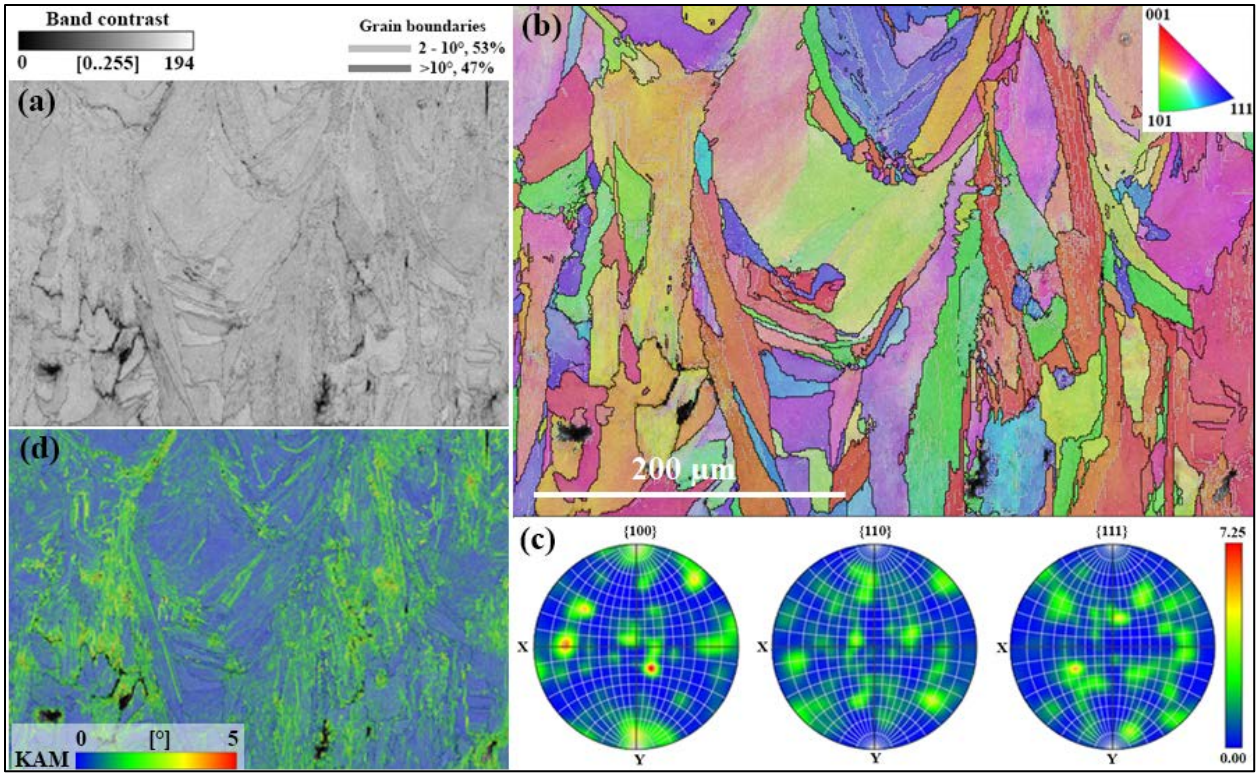

Figure 49. (a) Band contrast (BC) + grain boundary (GB), (b) BC + IPF + GB maps, (d) PFs, (d) KAM + BC maps of a center area of the BD surface of AFA Sample #9.

Because of the small area of AFA sample #9, only an area of 15.3 mm^2 was used in microhardness testing. The minimum and maximum hardness values of the area tested were 150.9 and 205.7 HV, respectively, and the average value was 55.2 ± 13.2 HV. The highest hardness values were observed close to the center of the sample, and hardness was also high compared with the lower part of the BD surface of the sample (Figure 50). Lower hardness values were observed mainly in the upper part of the sample in the BD surface.

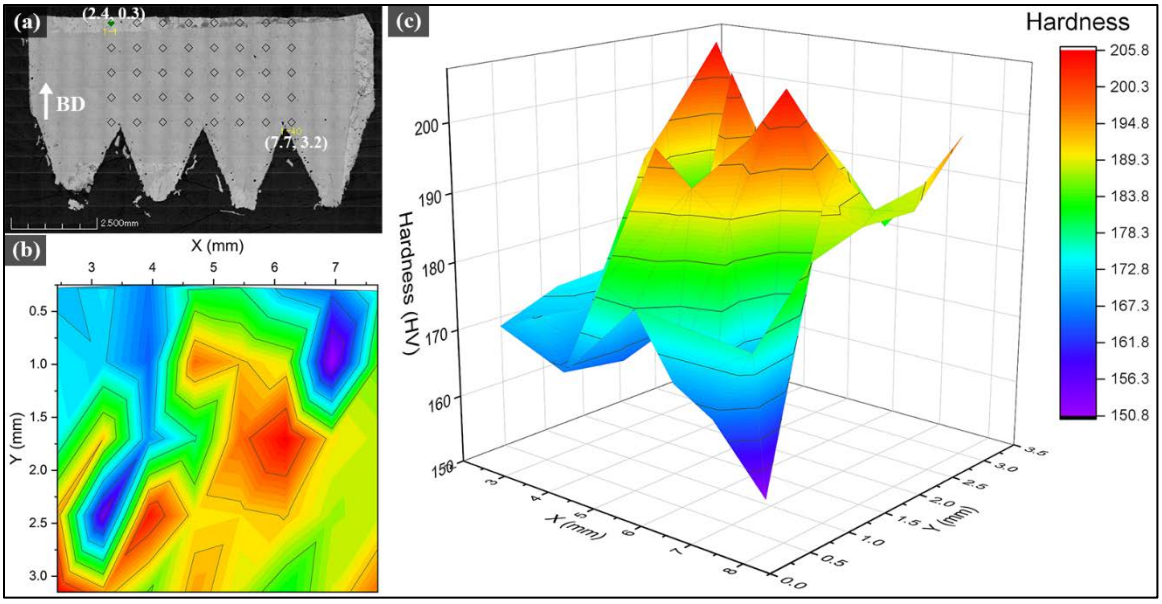

Figure 50. (a) Optical image, (b) contour of microhardness, and (c) 3D surface of microhardness of AFA sample #9.

A709 (NF 709)

Figure 51 shows the as-received A709 powder with a higher-magnification image shown in the inset. The powder is shown to be spherical, though a few planetary powders exist. Some irregularly shaped particles can also be observed in the high-magnification image, although their volume fraction seems to be very low.

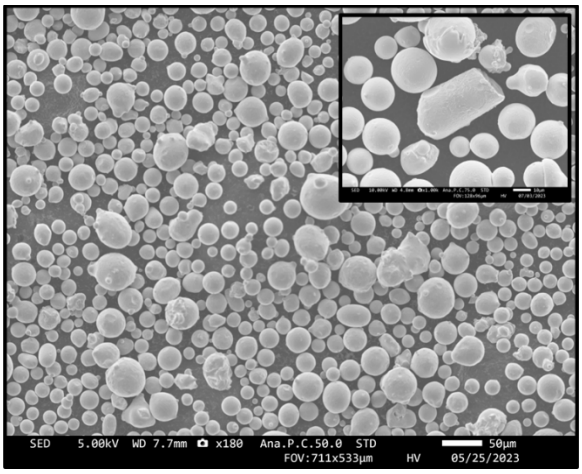

Figure 51. SEM image showing the spherical A709 powders.

Figure 52 shows the optical images of A709. The porosity values calculated using ImageJ are also displayed in these images. For the calculation of porosity, in total, five optical images at 100× magnification were taken, and the values obtained from ImageJ were averaged and shown here. As shown in these results for sample 3, which used the recommended condition by Renishaw for 316L SS, almost 99.997% density was achieved. Further investigation is being carried out to verify these values via Archimedes density measurements. Based on the optical images, sample 3 was chosen for further microstructural analysis.

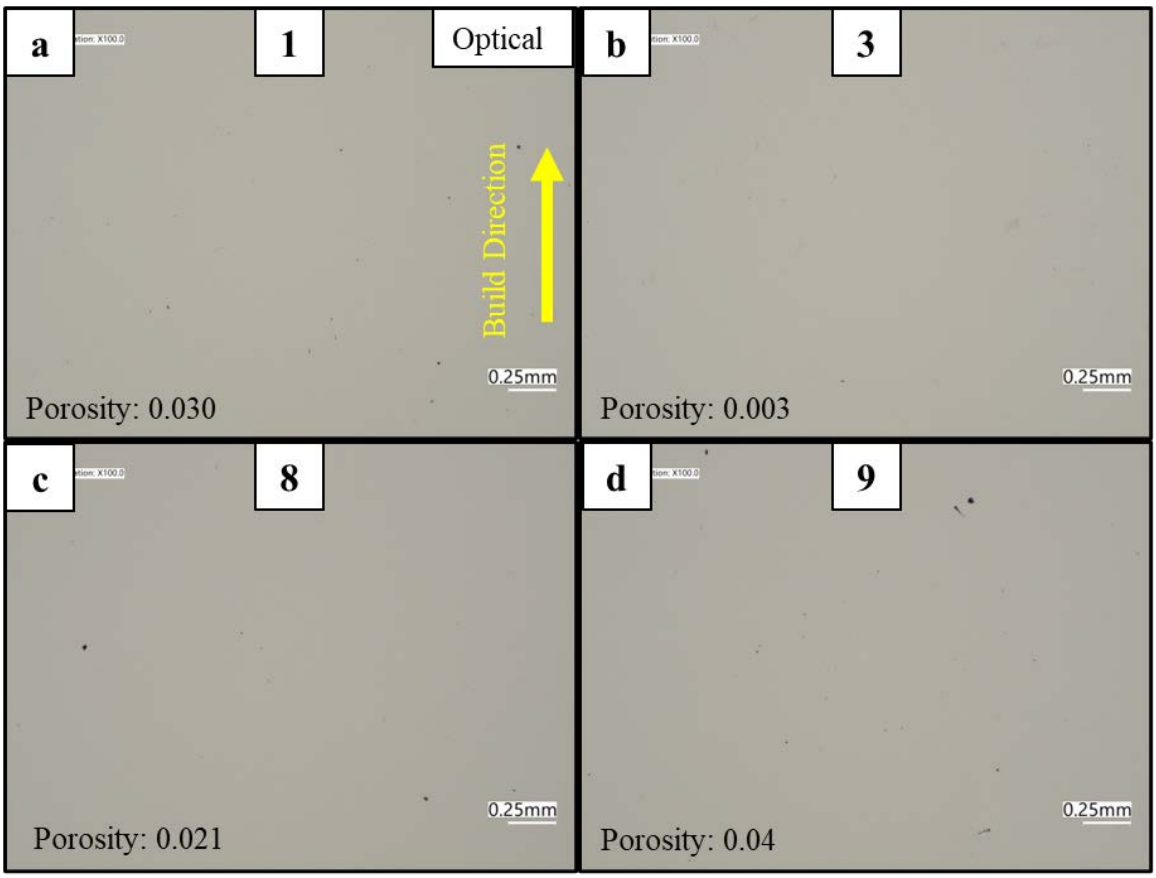

Figure 52. Optical images of four different processing conditions used for A709 alloy. More than 99.5% density was achieved in all conditions.

Figure 53 shows the BSE images of sample 3. Initial image analysis did not reveal the presence of any secondary phases. Interestingly though, at higher-magnification, cell structures similar to the ones in D9 steel were also noted in A709 alloy. Some of these cells looked very elongated, as shown in Figure 53b, and the other cells were more equiaxed.

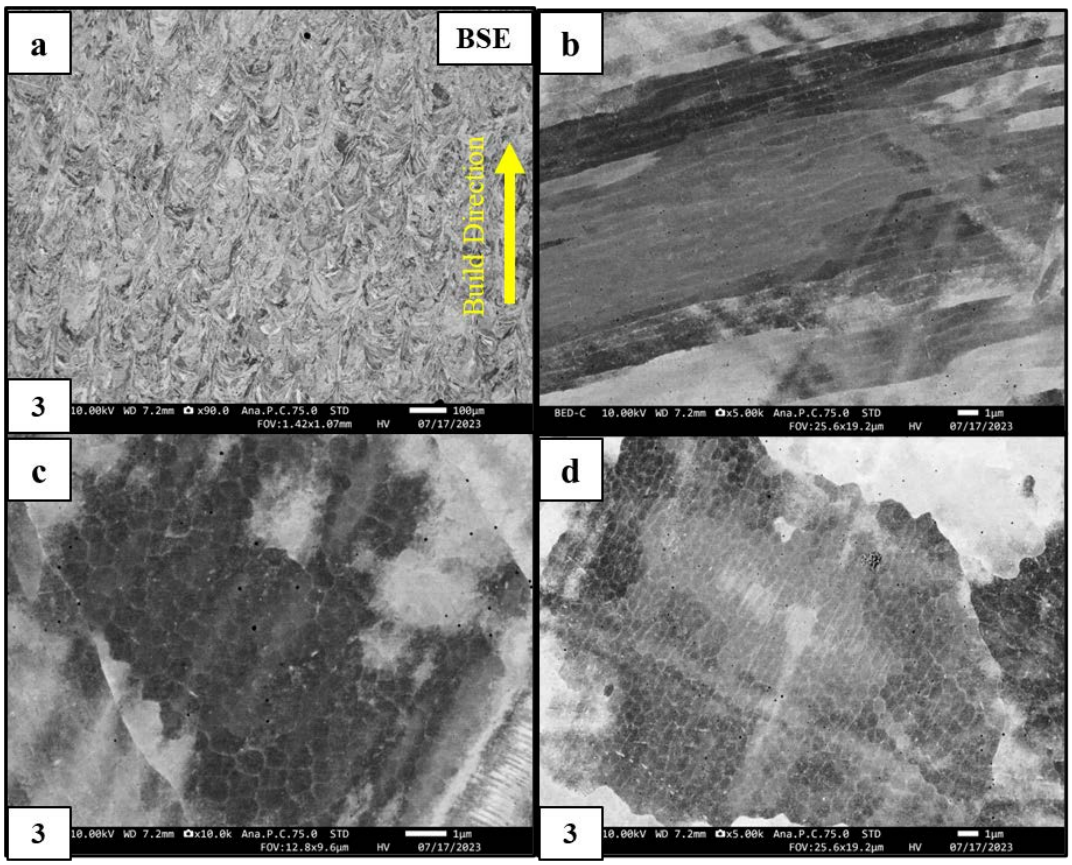

Figure 53. BSE-SEM image showing different features of sample A709 alloy. High-magnification images show cell structures noticed in other SS 316 alloys.

Similar to the other austenitic SSs, face-centered cubic (fcc) grains are clearly noted in the EBSD data shown in Figure 54. No obvious texture was noted in the sample. The melt pool direction is clearly shown in the high-magnification EBSD images. No other phases were noted.

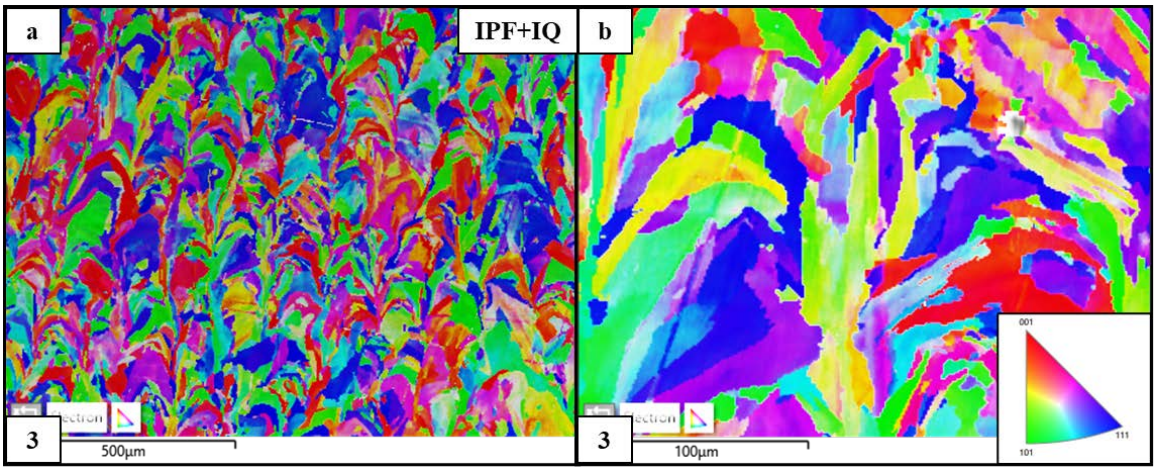

Figure 54. EBSD IPF + Image Quality (IQ) map showing grain size and orientation of A709 alloys. No second phase was detected.

6.2.2.2 Ferritic/Martensitic Steels

Notably, as mentioned in the experimental section, the energy densities (i.e., process parameters) used for ferritic/martensitic steels are higher when compared with austenitic steels. This information was based on a literature review, which was further corroborated by single-track experimental evidence.

HT9

Figure 55 shows the powder for HT9. Although most of the particles are spherical, considerably more difference exists in morphology compared with the D9 powder.

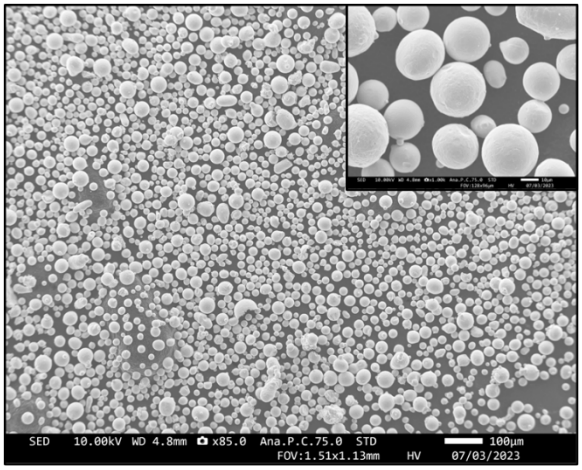

Figure 55. SEM image showing the spherical HT9 powders.

The selected optical images are shown in Figure 56. The microstructures clearly show very little porosity in all the conditions. This result proves that the knowledge from single-track experiments can potentially be deployed into full-scale builds. No other significant features could be seen at this scale. As such, electron microscopy was performed on sample 3.

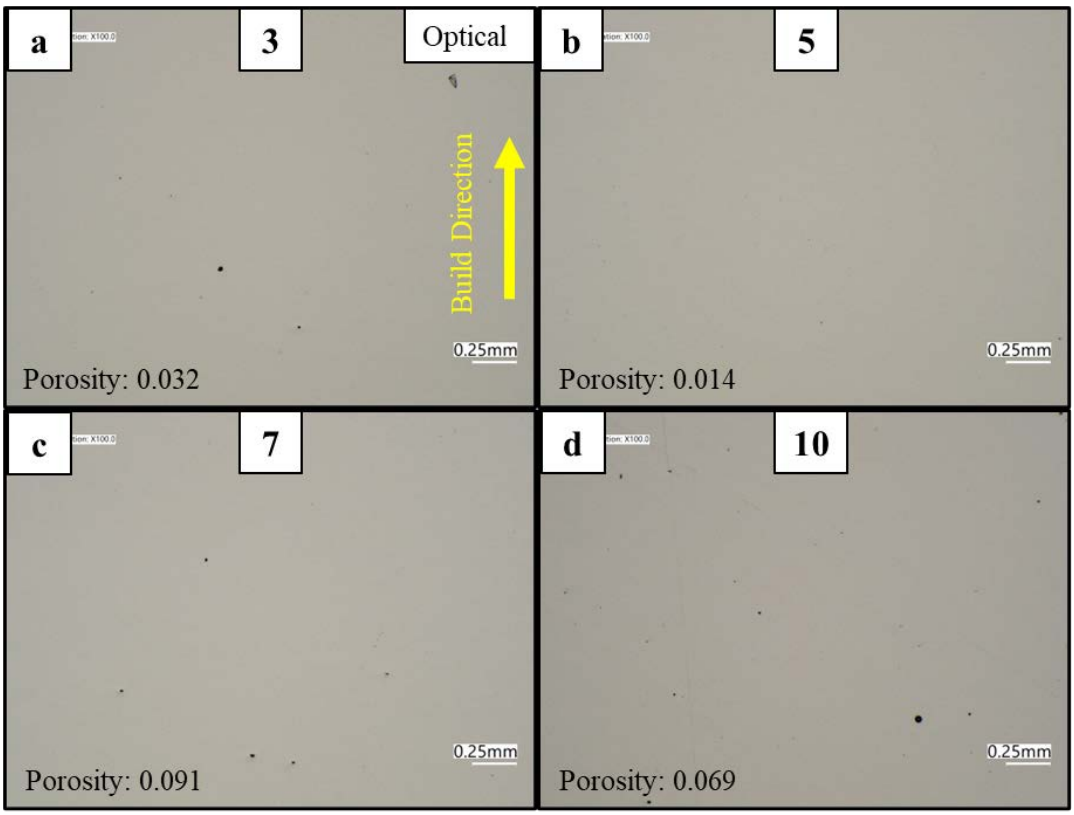

Figure 56. Optical images of four different processing conditions used for HT9 alloy. More than 99.5% density was achieved in all conditions.

The SEM images of sample 3 in Figure 57 show very interesting features in the HT9 alloy. These images show higher-magnification images of the same features. Clear evidence of the presence of martensite is noted in this system. Interestingly, the presence of martensite was only observed next to the darker flower-like features. Further investigation needs to be done to better understand this phenomenon.

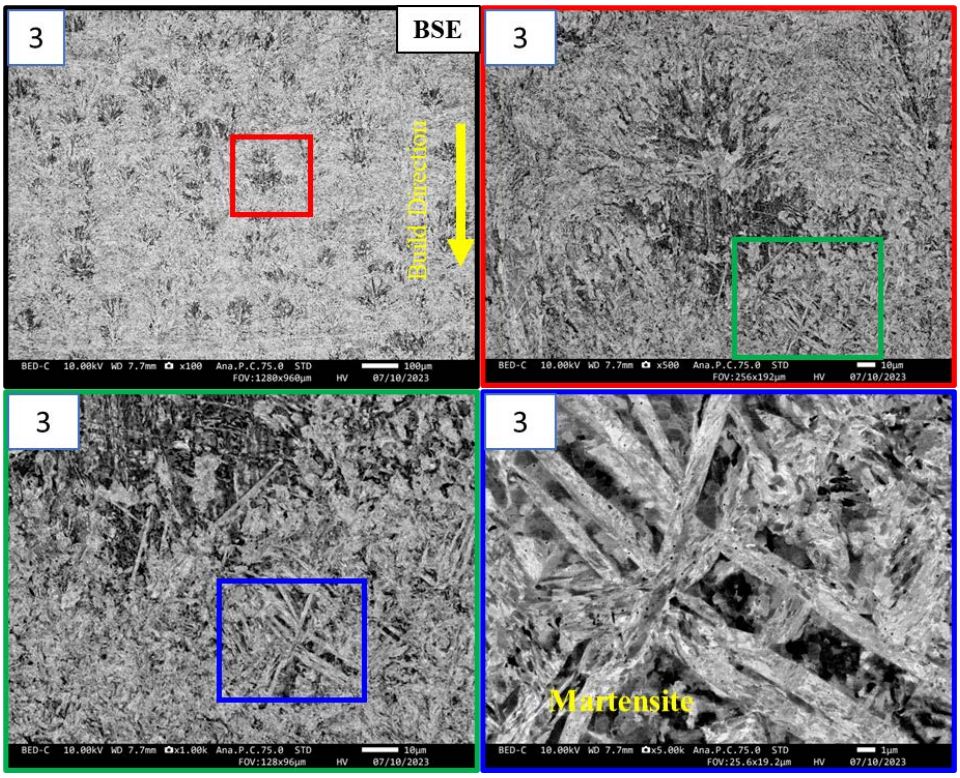

Figure 57. BSE-SEM image showing different features of sample condition 3 for HT9 alloy. High-magnification image shows clear presence of martensitic laths present in body-centered cubic matrix.

Very high-magnification EBSD was done on sample 3 to capture the martensite features. Laths in the bottom grain, shown in Figure 58's different colors, are possibly martensitic laths, but more work needs to be done to confirm this result. Notably, the matrix here is body-centered cubic (bcc), and the IPF map indicates as such.

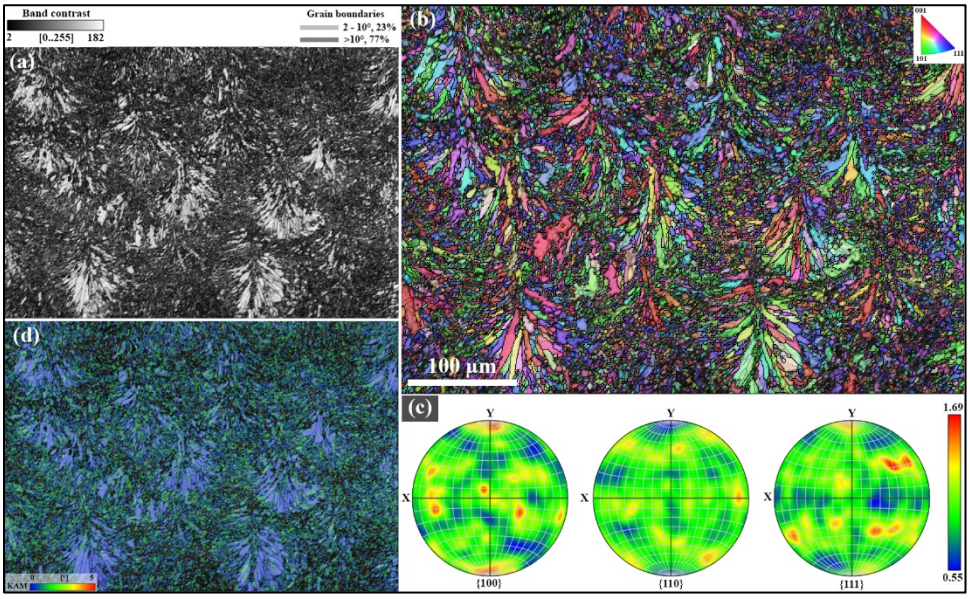

Figure 58. (a) Band contrast (BC), (b) BC + IPF + grain boundary (GB) maps, (c) PFs, and (d) KAM + BC map of a center area of the BD surface of HT-9 sample #5.

STEM imaging of HT-9 sample #5 (Figure 59) shows the presence of a considerable number of dislocations. Some nanoparticles or precipitates are also along grain boundaries, and some are within grains. These particles also interact with dislocations, as shown well in the high-resolution image in Figure 59c. Elemental mapping shows that at least two types of particles/precipitates are present. One type is rich with chromium, vanadium, and carbon, suggesting a mixed metal carbide. The second type consists of mostly aluminum. Iron is absent in both of these precipitates.

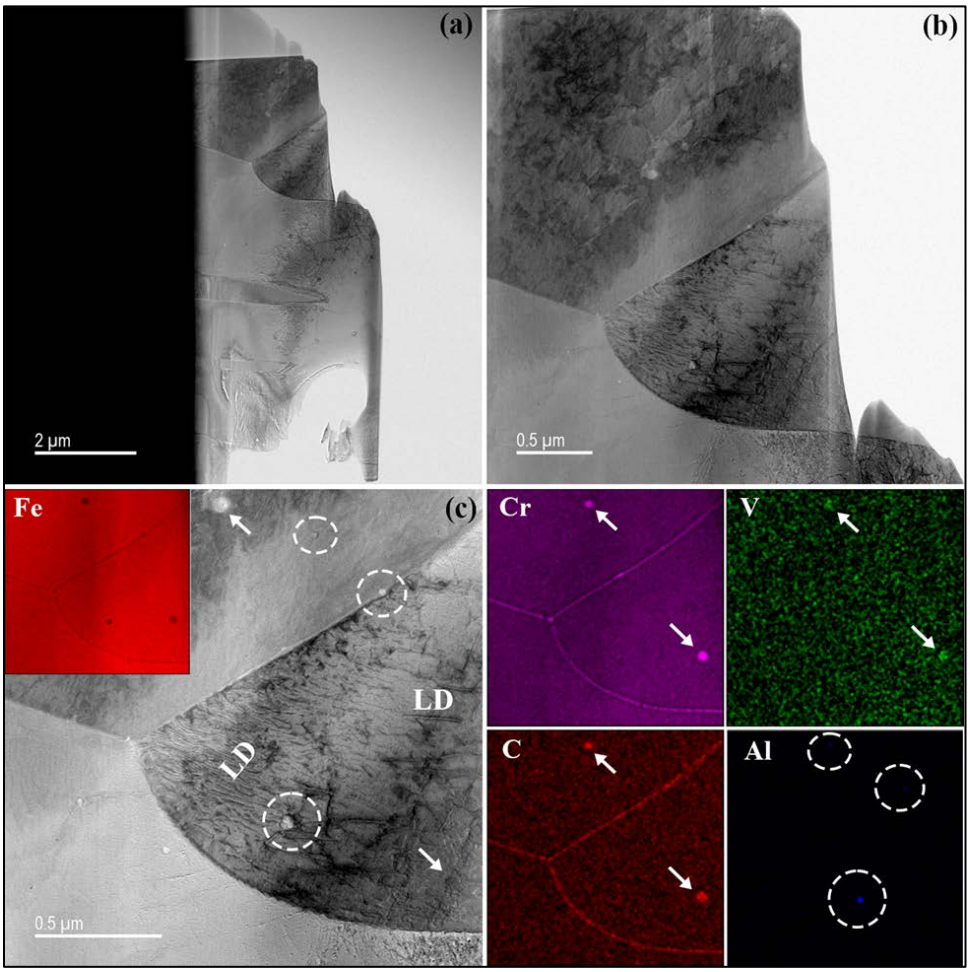

Figure 59. BF STEM images of HT-9 sample #5 at (a–c) three different resolutions and elemental maps of region shown in (c). Arrows, circles, and *LD* indicate (Cr, V) carbon-type phase particles, aluminum-rich particles, and line dislocations, respectively.

STEM images and elemental maps of another area of the sample are shown in Figure 60. In the BF STEM images, secondary precipitates and line dislocation interactions are clearly shown, and some dislocation clusters are also present. A closer look into the precipitate shows the presence of a second nanoprecipitate within it. Although chromium, molybdenum, vanadium, and carbon concentrations are high in the bulk precipitate shown in Figure 60e, the nanoprecipitate within it is high in manganese, aluminum, and oxygen concentrations. These elemental maps suggest the precipitates to be $(Cr, Mo, V)_xC_y$- and $(Mn, Al)_xO_y$-type phases.

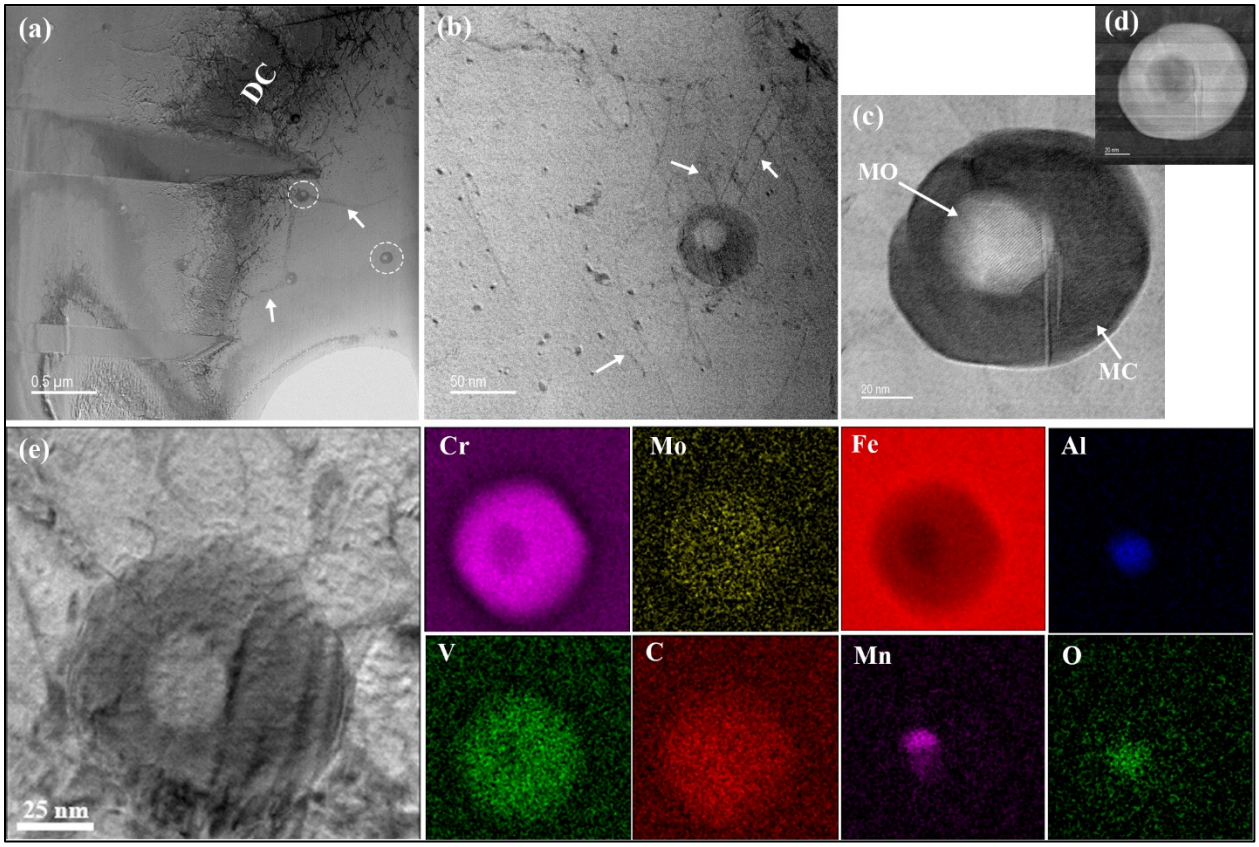

Figure 60. STEM and elemental maps of another area of HT-9 sample #5. (a) BF STEM at a lower resolution, (b) BF STEM at a high resolution, and (c) BF and (d) HAADF STEM images of a particle/precipitate. (e) STEM image of a nanoparticle and its corresponding elemental maps. *DC*, *MO*, and *MC* denote dislocation cluster, metal oxide, and metal carbide, respectively.

A considerably high microhardness (320–464 HV, Table 17) with an average value of 411.6 ± 24.7 HV was acquired for HT-9 sample #5. High microhardness can be observed near the sample edge of the four sides, and mid- and lower hardness values are present in the middle of the sample (Figure 61).

Table 17. Dimension and hardness measurements for HT-9 sample 5

Sample #	Selected sample area dimensions			Microhardness values (HV)			
	Length (mm)	Height (mm)	Area (mm^2)	Min.	Max.	Average	Std. dev.
5	5.2	5.2	27.3	320.2	464.1	411.6	24.7

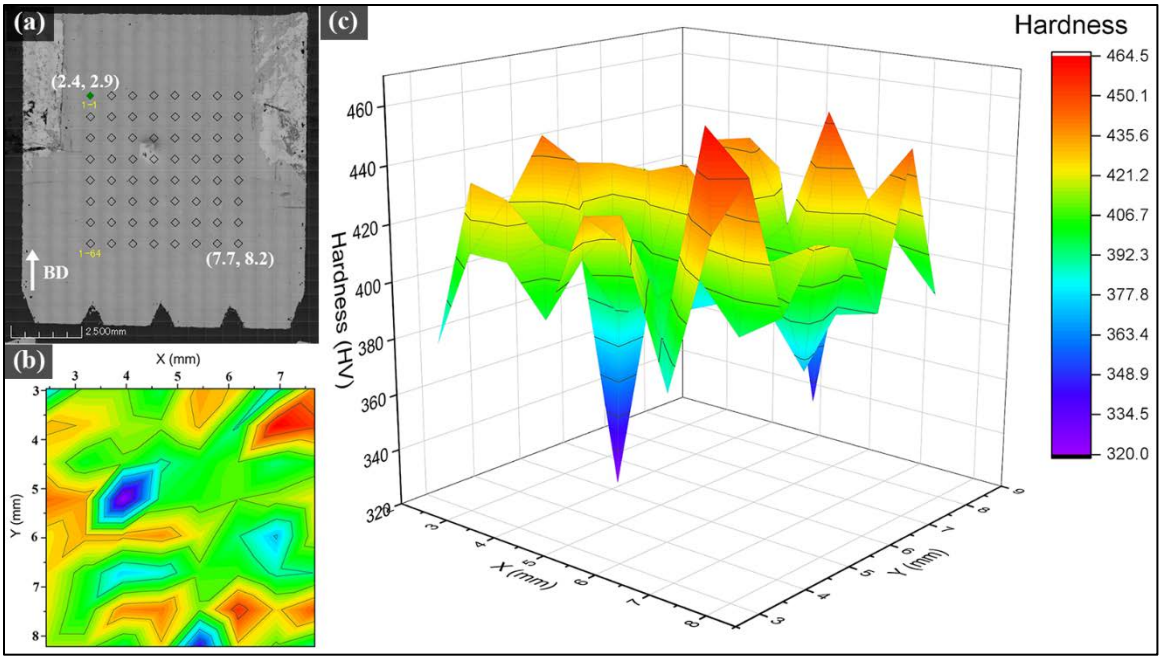

Figure 61. (a) Optical image with indent locations, (b) microhardness contour map, and (c) the corresponding 3D surface of HT-9 sample #5. *BD* denotes the BD of the sample.

Grade 91

Figure 62 shows the Grade 91 powder. Similar to the D9 sample, more planetary particles appear to be in this powder.

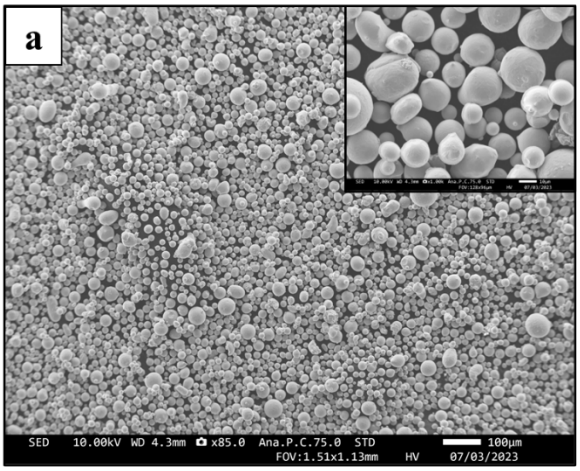

Figure 62. SEM image showing the spherical Grade 91 powders.

For the case of Grade 91, the optimized process parameters yielded almost fully dense microstructures, as shown in the optical images in Figure 63. Sample 3, which is the optimized condition from LANL [143], shows a volume fraction of porosity of only 0.055%.

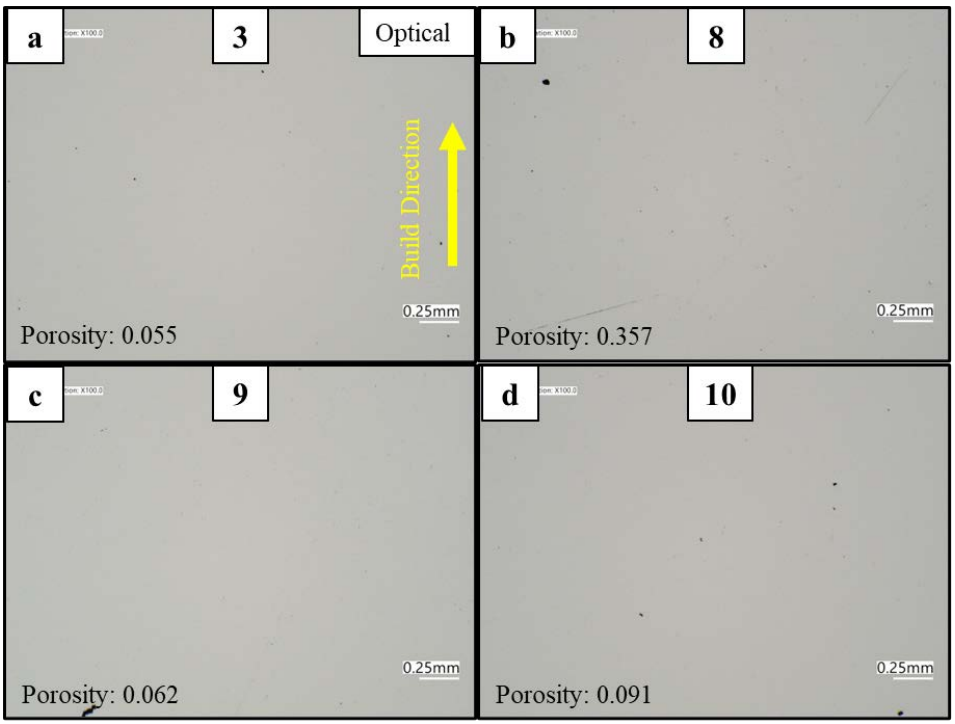

Figure 63. Optical images of four different processing conditions used for Grade 91 alloy. More than 99.5% density was achieved in all conditions.

Similar to all other samples, five different optical images were taken for each condition, and porosity was analyzed via ImageJ; the average is represented here.

The SEM images obtained from sample 9 do not show clear evidence of martensite—at least, not at this length scale (Figure 64). Similar observations were noted by Eftink et al. [144]. Higher magnification images show very fine cell structures, different from the dislocation cells observed in the austenitic steels, approximately 500 nm in size. Further investigation is necessary to fully understand the microstructure evolution of this alloy in the as-fabricated condition. The presence of single-phase bcc is confirmed via EBSD analysis, which is shown in Figure 65.

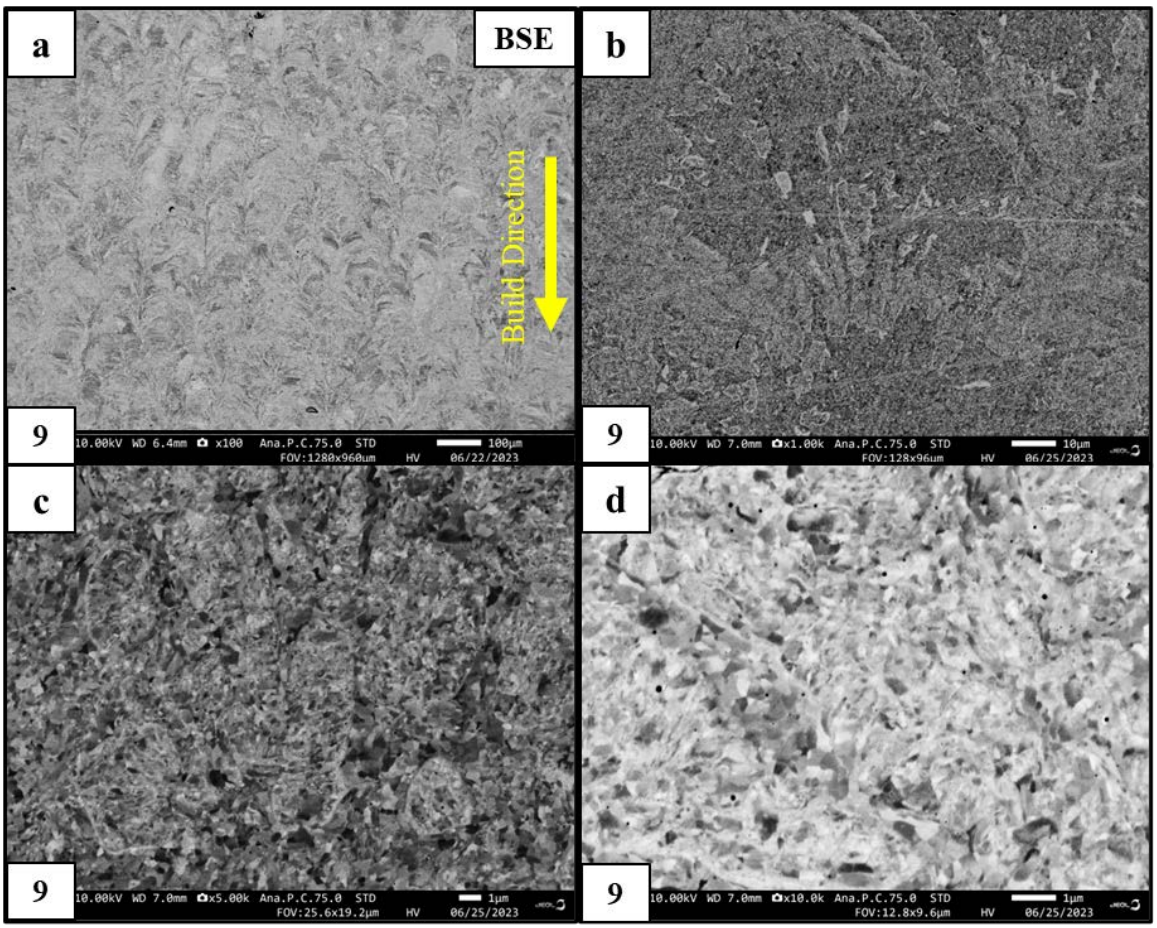

Figure 64. BSE-SEM image showing different features of sample condition 9 for Grade 91 alloy. No martensite was noted in this alloy, although very small cells were present throughout.

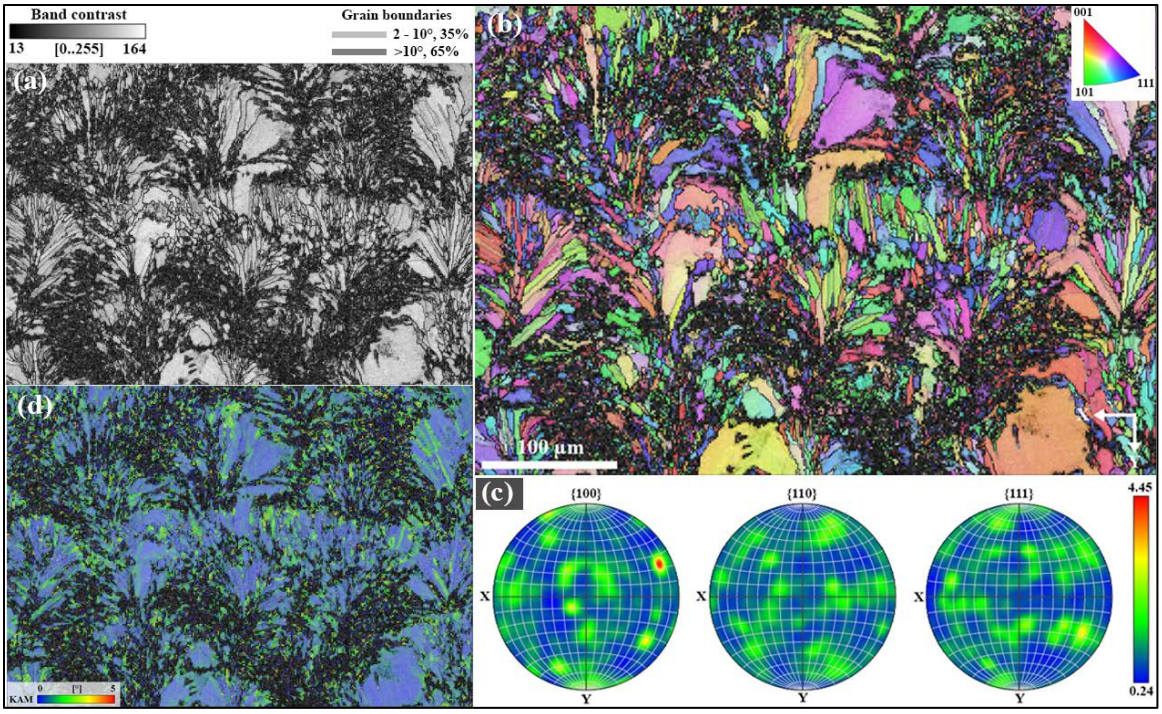

Figure 65. High-magnification EBSD IPF + Image Quality (IQ) map of sample condition 9 for Grade 91 alloy showing grain size and orientation. No secondary phase was detected.

Compared with HT9, Grade 91 (sample #9) reported lower average microhardness (281.4 ± 21.1 HV) with a minimum of 237.3 HV and maximum of 334.6 HV (Table 18). In this sample, variation of hardness is mostly random. However, high hardness values can be observed near the edges of the lower, left, and right sides with respect to the BD of the sample (Figure 66).

Table 18. Dimensions and hardness measurements for Grade 91 sample 9

Sample #	Selected sample area dimensions			Microhardness values (HV)			
	Length (mm)	Height (mm)	Area (mm^2)	Min.	Max.	Average	Std. dev.
9	5.2	5.2	27.5	237.3	334.6	281.4	21.1

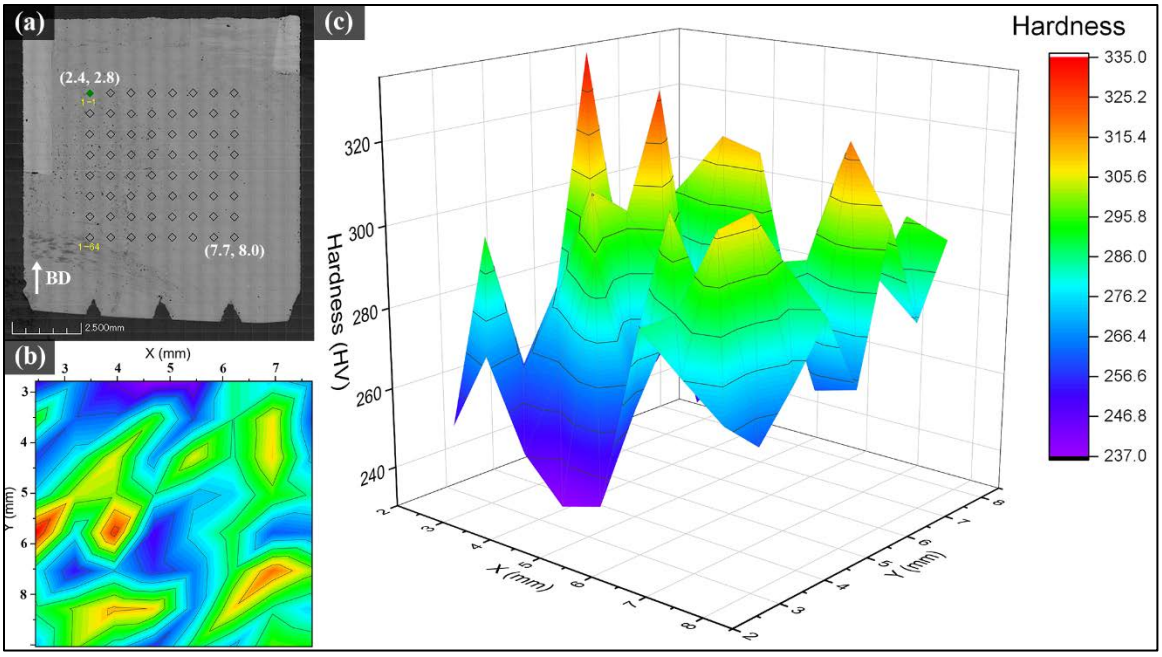

Figure 66. (a) Optical image and microhardness data of Grade 91 sample #9 using a (b) contour and (c) 3D surface maps. *BD* denotes the BD of the sample.

Grade 92

The last alloy discussed in the present work is Grade 92. Figure 67 shows the powder of Grade 92.

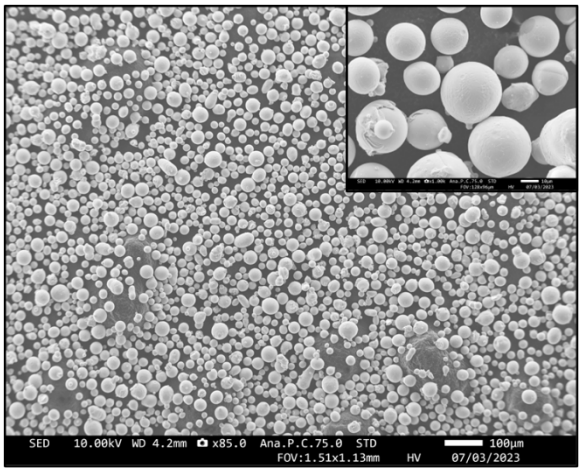

Figure 67. SEM image showing the spherical Grade 92 powder.

For the case of Grade 92, the optimized process parameters yielded almost fully dense microstructures, as shown in the optical images in Figure 68.

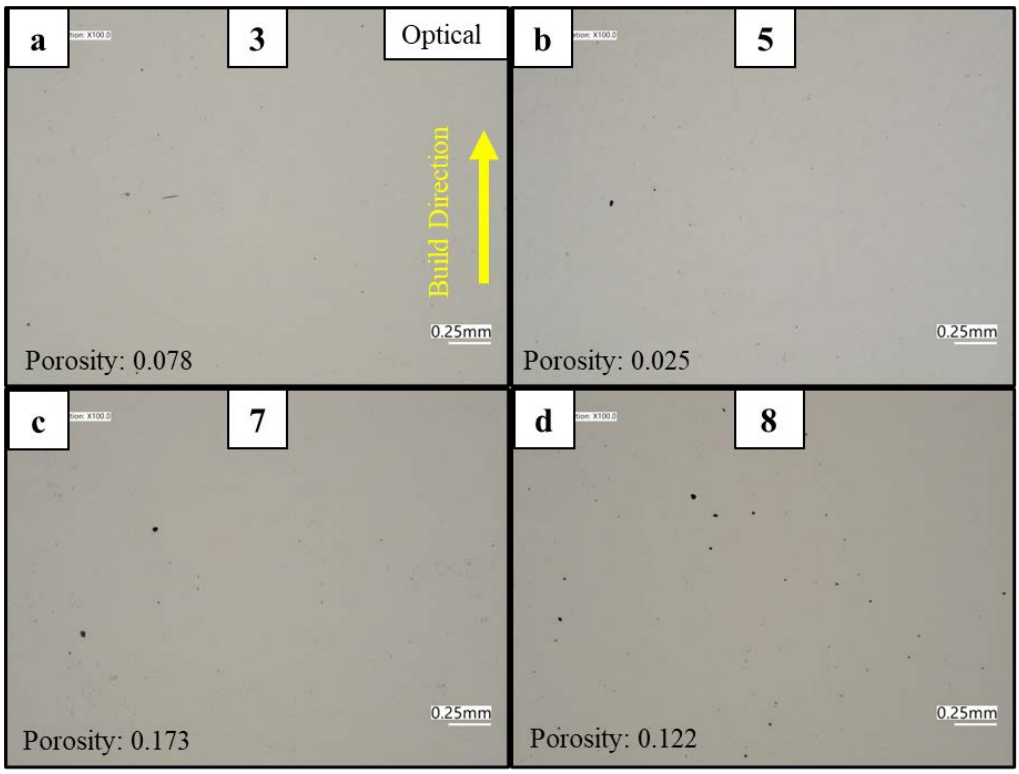

Figure 68. Optical images of four different processing conditions used for Grade 92 alloy. More than 99.5% density was achieved in all conditions.

The SEM images (Figure 69) obtained from sample 7 do not show the presence of any evidence of martensite—at least, not at this length scale—similar to Grade 91. A clear overlap of melt pool boundaries along the BD is shown in the images, and a change in grain contrast can be observed along the interface. Again, similar to Grade 91, higher-magnification images show very fine cell structures approximately 500 nm in size.

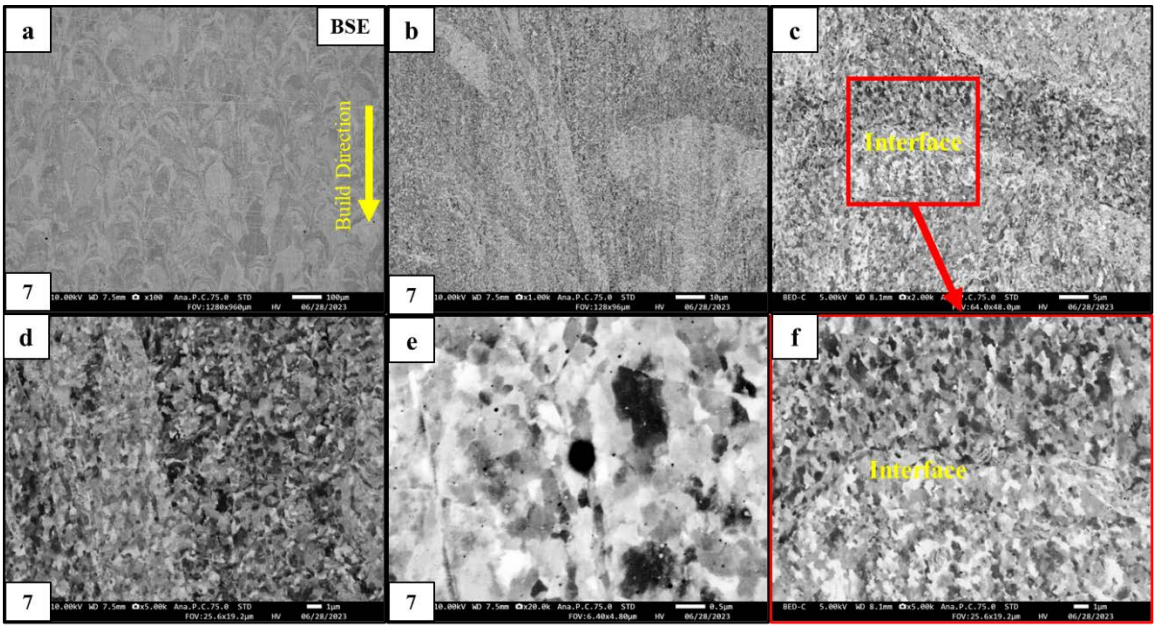

Figure 69. BSE-SEM image showing different features of sample condition 7 for Grade 92 alloy. No martensite was noted in this alloy, although very small cells were present throughout.

Oxide Dispersion–Strengthened Fe–Cr–Al

Optical micrographs of the three Fe–Cr–Al samples collected using a BX51 optical microscope are shown in Figure 70. As observed in Figure 70a, there is considerable amount of porosity, and some crack propagation started at the side edges of Sample #3. Microsized pore spaces also can be observed in samples #9 and #12, but sample #12 had less. The pattern of the change in density of these samples also matches well with the pattern of the level of defects; that is, samples with a higher level of defects have lower density. As shown in Figure 71, columnar grains are mostly observed in the surface of the sample along the AM BD of Fe–Cr–Al sample #12. No significant change in the grain microstructure is observed in the sample with respect to the region (i.e., lower, center, and upper parts) scanned along the sample's BD. Some microsized pore spaces are also observed in these SEM micrographs. As observed in the

optical microscopic images, sample #3 consists of larger pore spaces and microcracks, as depicted in BSE-SEM images in Figure 71d and confirmed by the corresponding BSE-SEM image in Figure 71e.

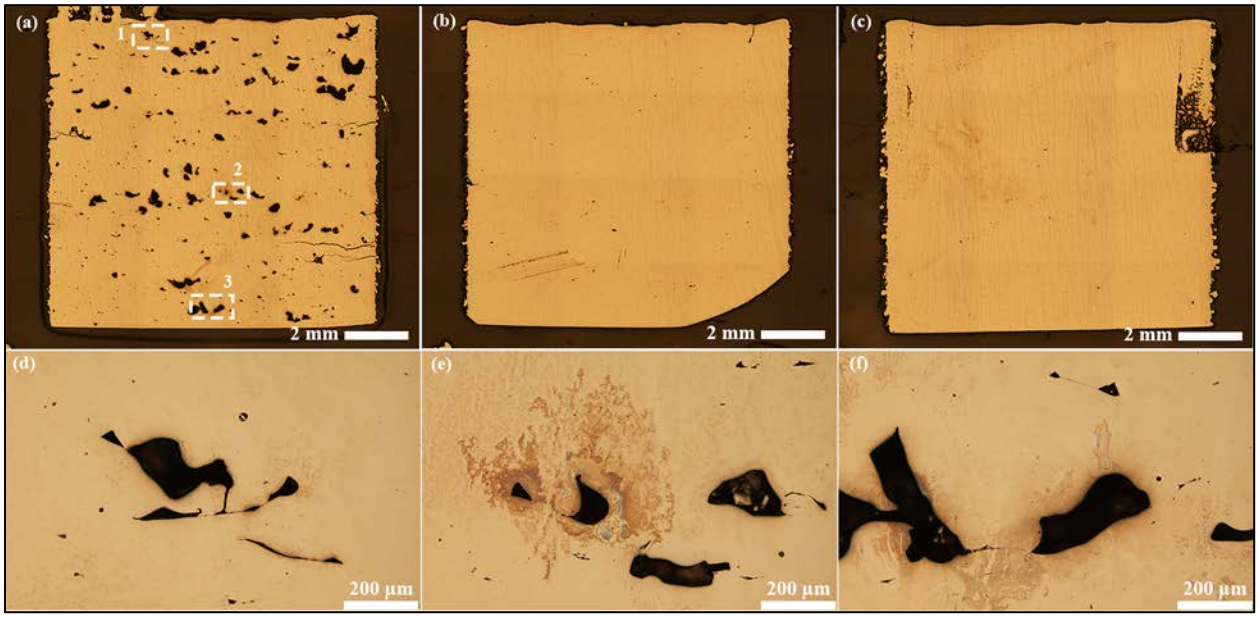

Figure 70. Optical micrographs of the three Fe–Cr–Al samples. High-resolution images in (d), (e), and (f) are from the areas 1, 2, and 3, respectively, in (a).

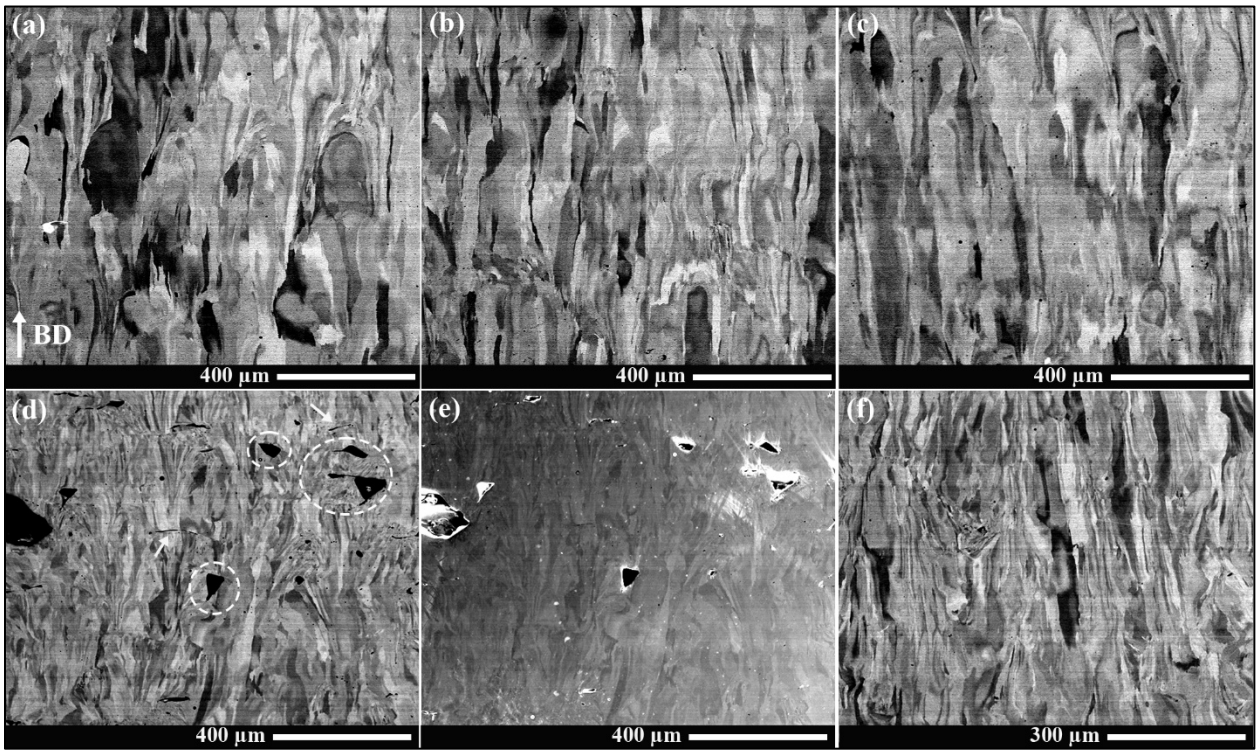

Figure 71. BSE-SEM images of Fe–Cr–Al sample #12 at the (a) lower, (b) center, and (c) upper parts of the BD surface. *BD* indicates the AM BD of the sample. (d) and (e) BSE-SEM images of the center of sample #3. (f) BSE-SEM image of the center of sample #9.

The bcc structure with a space group of Im-3m was successfully used in solving the crystal structure of the sample area analyzed using EBSD. A maximum band contrast of 205 was achieved for the pattern quality, as shown in Figure 72, with a considerably high structure solution. As was observed using BSE-SEM imaging, the columnar grains show a texture (maximum of ~13× random) and is identified to be parallel to the {100} plane, as observed by IPF and PF images. EBSD analysis also showed a mean grain size of 27.1 ± 12.2 µm, with minimum and maximum grain sizes of 17.8 and 153.8 µm, respectively.

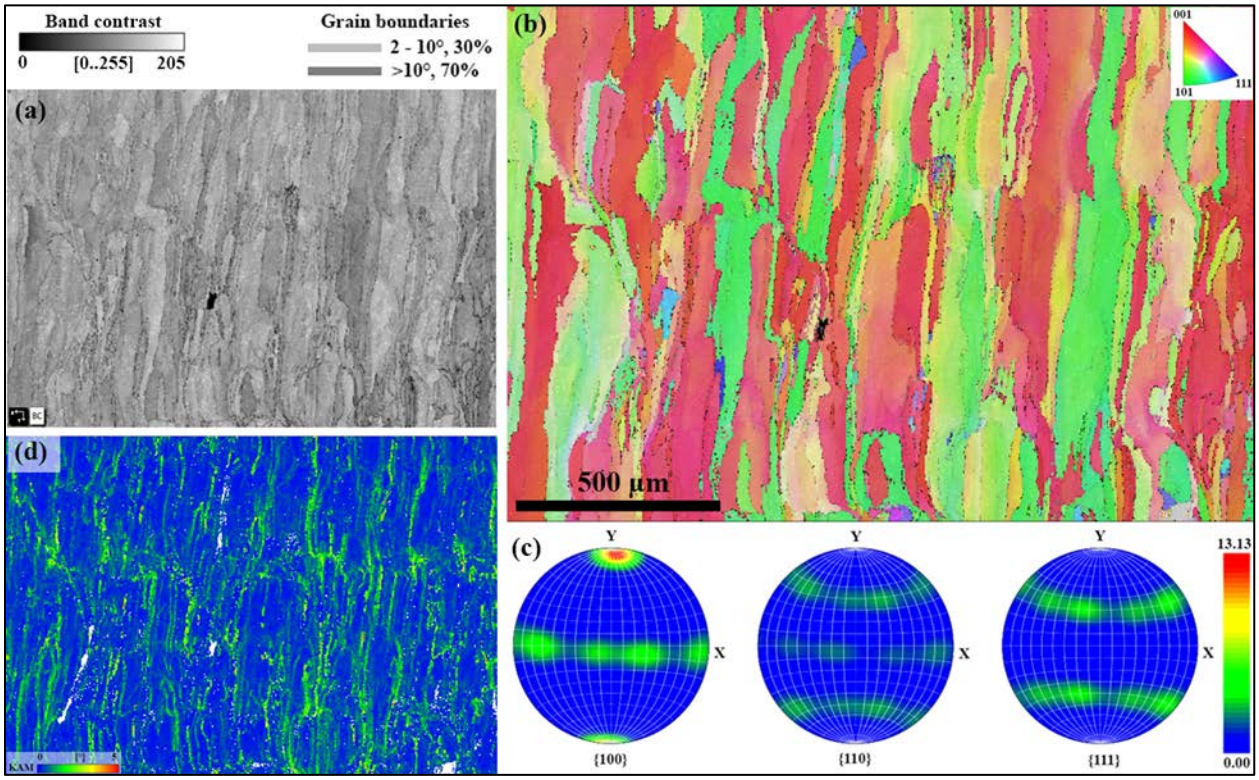

Figure 72. EBSD data collected from the center of the BD surface of the Fe–Cr–Al sample #12. (a) Band contrast (BC) + grain boundary (GB) map, (b) BC + IPF + GB map, (c) PFs, and (d) KAM map.

The dark-contrast areas in the BF STEM image in Figure 73 shows secondary precipitate in Fe–Cr–Al sample #12. These precipitates or particles are observed in bright contrast in the corresponding HAADF STEM image, indicating the secondary precipitates to have high-*Z*, or high–atomic number, element(s). These high-resolution images further verify the presence of secondary precipitates. This sample also consists of dislocations (line and loop-type) and nanosized pore spaces, as highlighted in these figures. Some of these line dislocations interact with nanoparticles or precipitates, suggesting possible interference in the mechanical properties of the sample.

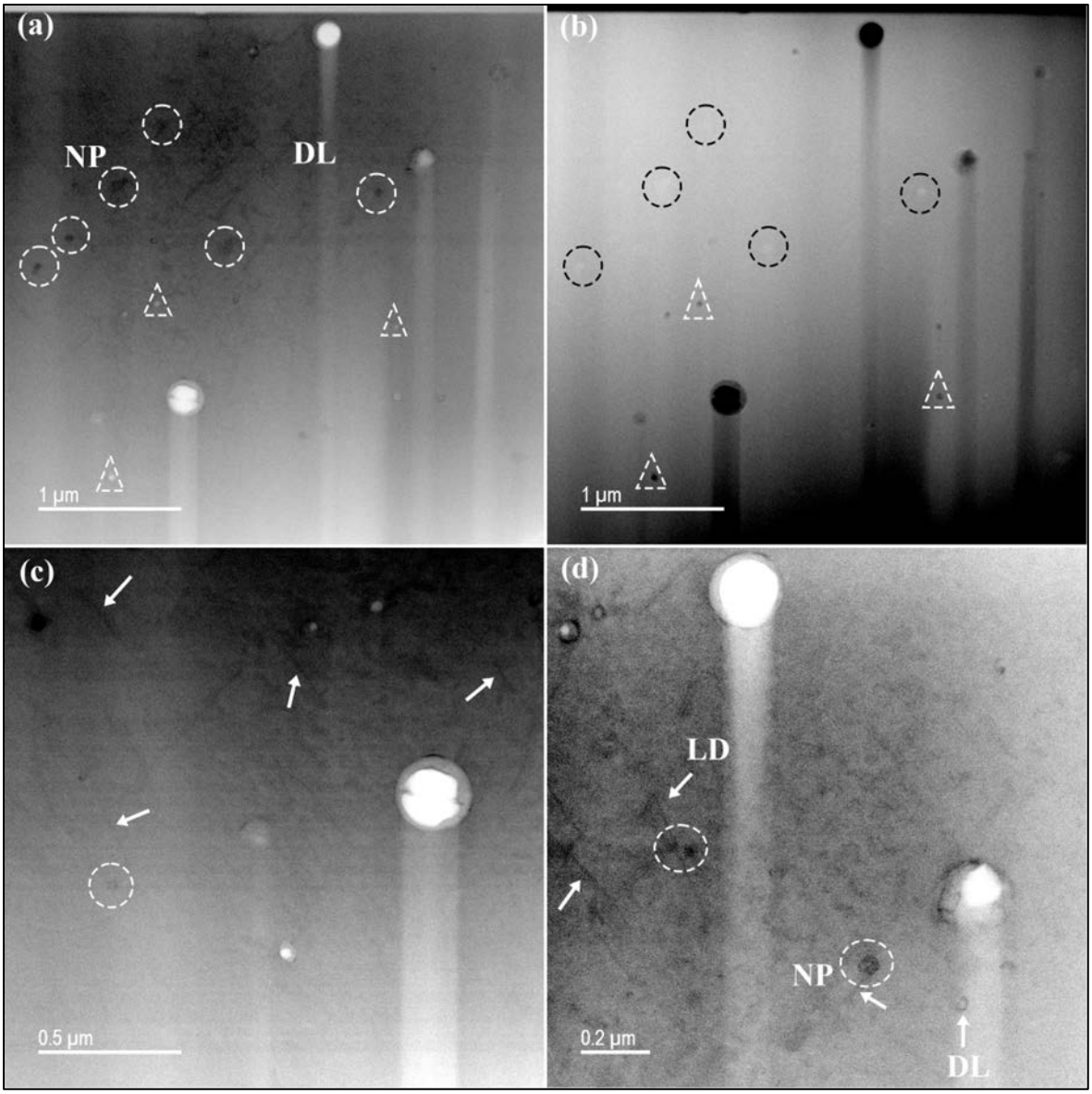

Figure 73. STEM images of Fe–Cr–Al sample #12. (a) BF and (b) HAADF STEM images. (c) and (d) BF STEM images at high resolution. Circles, triangles, and arrows highlight nanoparticles, pore spaces, and dislocations (LD: line dislocations, DL: dislocation loop, NP: nanoparticle).

An area of 23.3 mm^2 of Fe–Cr–Al sample #12 was selected for microhardness testing consisting of 64 indents using a test load of 300 gf, as shown in Figure 74. The lowest hardness values are observed in the upper part of the BD. Average hardness values are mostly observed in the lower-to-center region of the BD surface.

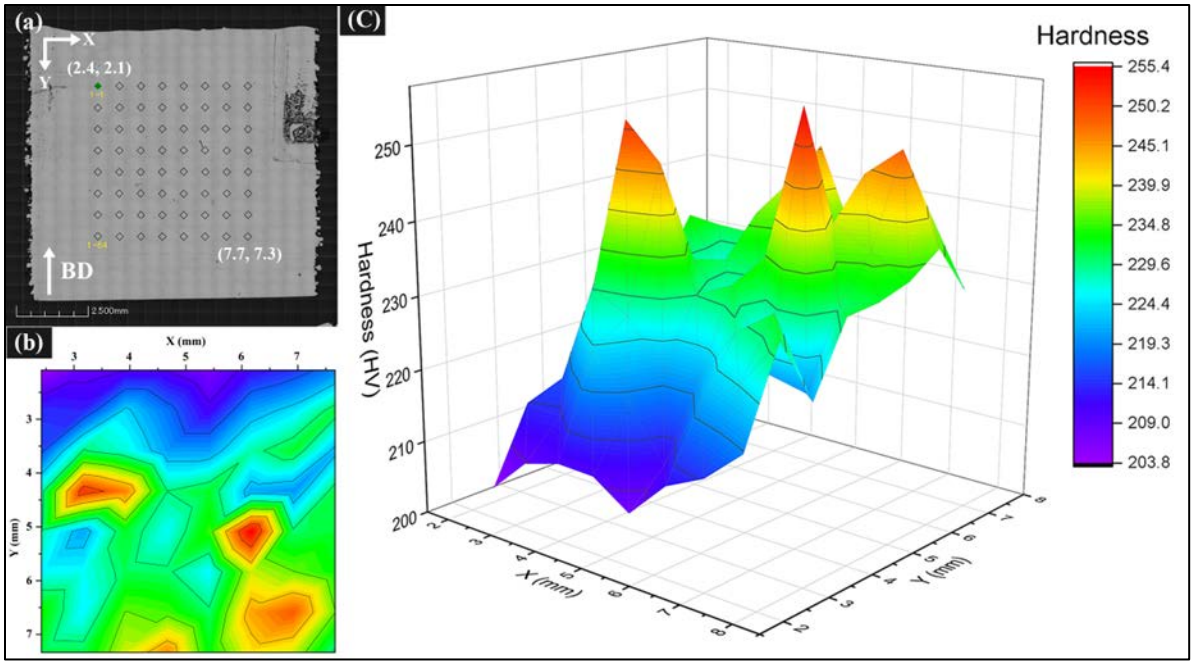

Figure 74. (a) Optical micrograph indicating indents used for microhardness testing of Fe–Cr–Al sample #12 and representations of microhardness using (b) contour and (c) 3D surface plots.

6.3 DISCUSSION

6.3.1 Single-Track Experiments

To optimize the process parameters for the 3D printing of the alloys, single-track experiments with 72 different processing conditions were done for each alloy class (i.e., austenitic SSs and ferritic/martensitic SSs). The dimensions, morphology, overlap, and more of the melt pools created by the laser track are used to understand whether the process conditions employed are successful good. A schematic showing the melt pool overlap and effects of energy density is shown in Figure 75 [149]. For a normal condition, adequate penetration and overlap to the previous layers and adjacent melt pools was noted. For conditions that have lower energy density, smaller melt pools were formed, which may lead to a lack of fusion between the adjacent melt pools and between the layers. If a higher energy density is used, especially with higher powers and lower lasing speeds, these conditions could lead to penetration through many layers, causing keyhole issues [149]. A disrupted melt pool occurs when there is spatter or other inclusions.

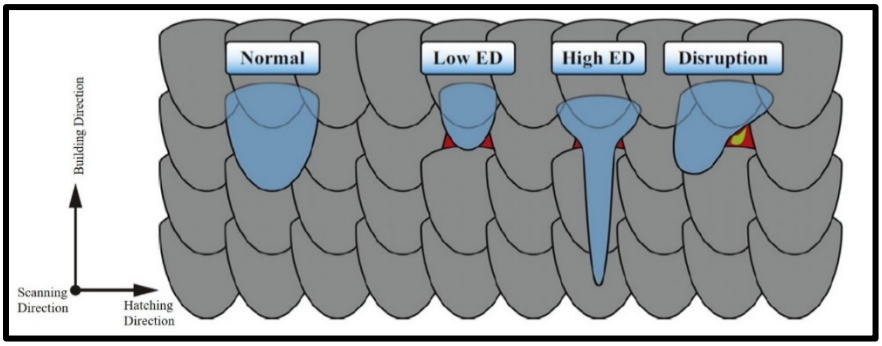

Figure 75. Schematic showing the melt pool overlap and effects of energy density (ED) [149].

The sample with the ideal condition, shown in Figure 39, satisfies the criteria for a normal condition. The modified condition, shown in Figure 40 which has an energy density approximately 50% higher than the ideal condition, shows porosity. Based on these results, a set of parameters to be used for final prints was narrowed down to 10 for each alloy class, with the energy density variation <6.5% for austenitic SSs. The energy density variation was maintained for ferritic/martensitic steels.

6.3.2 Block Build: Austenitic Stainless Steels

The process parameters chosen for printing the three austenitic SSs (D9, AFA, and A709) were based off the ideal conditions provided by Renishaw for SS 316L. Extensive cracking was noted in D9 and AFA alloys on the initial prints. Considering the composition difference between SS 316 and D9 is just the minute addition of titanium, it was surprising to see the microstructure of the as built condition. Further inspection revealed that the cracking and other defects observed in the sample were not because of the processing conditions but because of internal issues within the machine. In spite of the cracking, a preliminary assessment was performed on the D9 sample. The SEM backscattered images, at this level of magnification, did not reveal the presence of any titanium carbides. Further investigation is necessary and is underway to look at the samples in TEM to look for these carbides. The SEM images show single-phase microstructure with cell structures within the grains. This structure is very commonly reported among SS 316 prints. EBSD analysis was done for phase identification and grain size analysis, and as expected, it shows single-phase fcc with grains between 40 and 120 μm. No obvious texture was noted in the samples.

A709 alloy was printed once the machine issues were fixed, and as can be seen from the optical images, almost full density was obtained in some processing conditions. Similar to D9 samples, in the BSE-SEM images, no obvious secondary phases were revealed. Cell structures of different sizes and shapes were noted across different grains, and this result is shown in Figure 53. EBSD analysis revealed the alloy to have single-phase fcc with grains between 40 and 120 μm in size.

6.3.3 Block Build: Ferritic/Martensitic Stainless Steels

The processing conditions for ferritic/martensitic steels were based off the work LANL performed on Grade 91 steel in an EOS M290 machine and conditions provided by Renishaw company for 17-4 PH steels. The energy densities used for printing ferritic/martensitic steels were much more varied compared with the austenitic steels, ranging between 50 and 80 J/mm^3. In spite of the variation in terms of energy density, all processing conditions yielded almost fully dense parts for all the three alloys. Grade 91 and Grade 92 in the as-deposited condition show single-phase bcc, with grains approximately 22–70 μm in size. The presence of martensite was not noted in either of the alloys. This result is consistent with the previous work published by El-Atwani et al. and Eftink et al. [143–144]. HT9, on the other hand, showed the presence of martensite within the bcc matrix. It was more prominent along the reheat zones, where a flowery feature is noted. More work needs to be done to understand the microstructure evolution of all three alloy systems. Finite element or Comsol-based techniques could potentially be used to understand the heat cycles to justify the microstructures formed in these alloys.

6.3.4 Block Build: Oxide Dispersion–Strengthened Fe–Cr–Al

All three Fe–Cr–Al–0.3Zr samples consisted of a single iron-based bcc phase according to powder XRD. Micro-XRD point scans conducted on one sample also showed no secondary phases present in the whole sample, and no significant change in the unit cell was observed. However, TEM/STEM studies showed the presence of nano- to microsize particles/precipitates in Fe–Cr–Al sample (#12). These precipitates were rich with yttrium, zirconium, oxygen, and carbon, suggesting the presence of metal oxide MO_x- and metal carbide MC_y-type phase compositions, where M represents the cations. Optical micrographs

showed that Fe–Cr–Al sample #3 contained a significant amount of microcracks, porosity, and some other defects, but sample #12 contained minimum defects. This observation was comparable with the maximum and minimum densities obtained for Fe–Cr–Al sample #12 and sample #3, respectively. At SEM imaging resolution, zirconium-, oxygen-, and/or carbon-rich particles were also identified. SEM micrographs also showed that the Fe–Cr–Al samples consist of columnar grains that elongate or distribute along the BD of the samples; this result was further confirmed using EBSD analysis that showed a texture parallel to {100} planes. EBSD analysis also showed a mean grain size of 27.1 ± 12.2 µm (min = 17.8 µm and max = 153.8 µm) for sample #12. The sample was also free of a significant level of residual strain according to the EBSD KAM map analysis. Sample #12 also had a considerably high microhardness value (227.9 ± 11.0 HV) tested over an area of 23.3 mm^2 using a 300 gf test load. It was also observed that the hardness is greater at the lower part of the sample along the BD compared with the upper part of it.

7. ADVANCED METHODOLOGIES TO ASSESS ALLOY PRINTABILITY

7.1 PRINTABILITY EVALUATION

A framework for evaluating printability is vital to obtain defect-free AM components with a reduced number of experiments to optimize parameters such as laser power and scan speed so that cost and time are saved. The key to creating this framework is to obtain printability maps indicating processing zones of defect-free and defected regions as a function of laser power and scan speed (Figure 76a) [150]. Various methods are used to obtain the printability of various alloys, such as normalized process maps with equivalent energy density (Figure 76b) [151] and universal scaling laws for keyholing (Figure 76c and d) [152, 153].

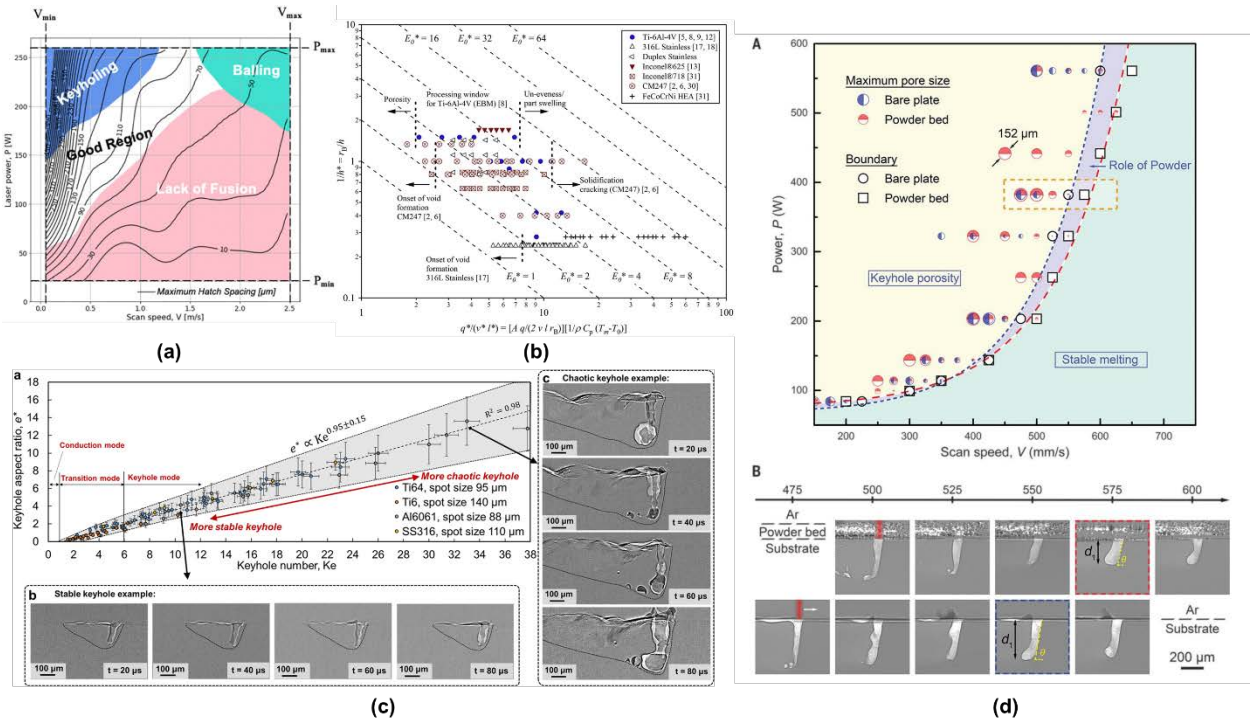

Figure 76. (a) An example of a printability map [154], (b) normalized process maps with equivalent energy density [155], and (c and d) maps related to keyholing defect [154, 156].

Although machine learning (ML) has been widely used for AM problems for the classification of defects, majority of the ML efforts [150-161] have focused on image-based learning and classifying the build quality as defective or acceptable. The literature survey of these methods and findings has been summarized in Table 19.

Table 19. List of ML efforts on AM defect identification summarizing the data set, ML models, and accuracy obtained in the identification of defects

Ref.	Data set size and nature	Target application	AM process	Material	Models used	Performance metric (%)
[154]	1,200 image data of part slices, 160 × 160 pixels each	Defect condition pattern recognition on scan tracks	Selective laser melting	Inconel 780	1	99.4
[155]	10,071 patches from 89 images of 14 builds	Defect type recognition: recoater hopping, recoater streaking, debris, super-elevation, part damage, incomplete spreading	LPBF	AlSi10Mg, bronze, Inconel 625, Inconel 718, SS 316 L, SS 17-4 PH, and Ti–6Al–4V	2	97
[157]	~14,200 image data	% of porosity	LPBF	Sponge titanium powder	3	91.2
[156]	~6,000 image data	Defect type recognition: overheating, normal, irregularity, balling	LPBF	316 L	3	99.7
[158]	462 images	Defect type recognition: Critical stripes, degradation due to faulty powder bed, overmelting,	Selective laser melting	—	3	Critical stripes recognition = 87.5 Degradation owing to faulty bed = 79.2 Overmelting = 86.1 Recoating defect = 97
[159]	4,314 RGB color images	Defect type classification: Delamination, Metal splatters, Ok	LPBF	H13 steel	4	96.8
[160]	1,454 images with defect, 241 without defect	Geometrical anomalies	Fused filament fabrication	—	3	85
[161]	100,000 original images augmented to 1 million images	Bended layers vs non bended	Contour crafting	—	3	97.5
[162]	9,724 good quality, 2,431 defects	Lack of fusion flaws	LPBF	Ti–6Al–4V	3	93.5

Table 19. List of ML efforts on AM defect identification summarizing the data set, ML models, and accuracy obtained in the identification of defects (continued)

Ref.	Data set size and nature	Target application	AM process	Material	Models used	Performance metric (%)
[163]	162 images converted into 5,805 training and 1,161 testing samples	Undermelt, overmelt, and good melt	Laser welding	ASTM F75 I Co–Cr–Mo	3	95
[164]	2,824 images for training, 942 for testing	Melt pool quality characterization: anomalous, noisy, and normal	LPBF	Inconel 625	5	95
[165]	9,426 images	cracks, ditches, foreign bodies	Selective laser sintering	Polyamide 12	3	95.8

7.2 CHEMICAL COMPOSITION–BASED ML MODEL TO PREDICT PRINTABILITY

With a goal of exploiting AM to improve the manufacturing of existing reactor materials, PNNL developed a chemical composition–based ML model to predict the printability of any given alloy in LPBF using experimental data from peer-reviewed literature. This NN model predicts the tendency of balling defect formation for a given composition under a given set of processing conditions, as shown in Figure 77. The NN model developed in this work has an accuracy of 92%, although it can only predict balling. The model takes material composition and laser parameters as inputs and calculates the probability of balling at those conditions. A manuscript has been submitted recently with the described work.

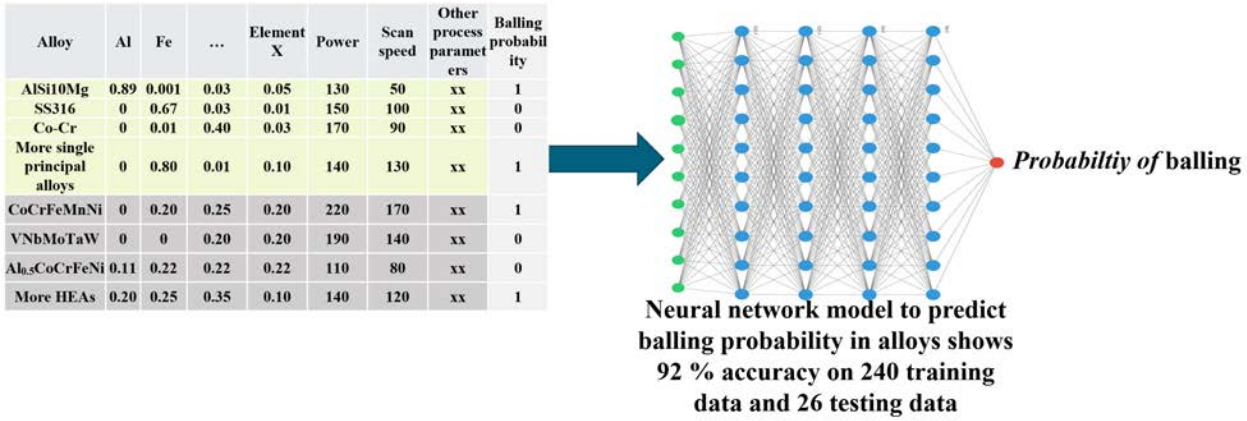

Figure 77. A general overview of the data set and the descriptors used to predict balling defect formation.

The further improvement of such a model is currently underway with the inclusion of porosity prediction in the ML model. Porosity data have been obtained from ANL, and more data are being added from literature.

7.3 LIMITATIONS OF APPROACH

The development of these ML models face two primary challenges. First, notably, experimental data for the occurrence of balling remain limited to approximately 15–20 different alloys. For this reason, it is unclear how effective these models can be at predicting defect occurrence for novel compositions using

only empirical data. Second, balling as a defect is simple to observe and is a binary phenomenon. To predict the frequency of more complex defects (e.g., the size and frequency of pores within a deposit), ML models require access to rich data sets of composition vs. process parameters and deposit quality. Acquiring this volume of data is not feasible to achieve through experimentation, but it is possible by using multiscale, physics-based models.

7.4 PROPOSED FUTURE WORK

The proposed work will demonstrate a methodology for the rapid prediction of alloy printability as a function of composition. To achieve this goal, simulation methodologies will be integrated in the following way, as illustrated schematically in Figure 78.

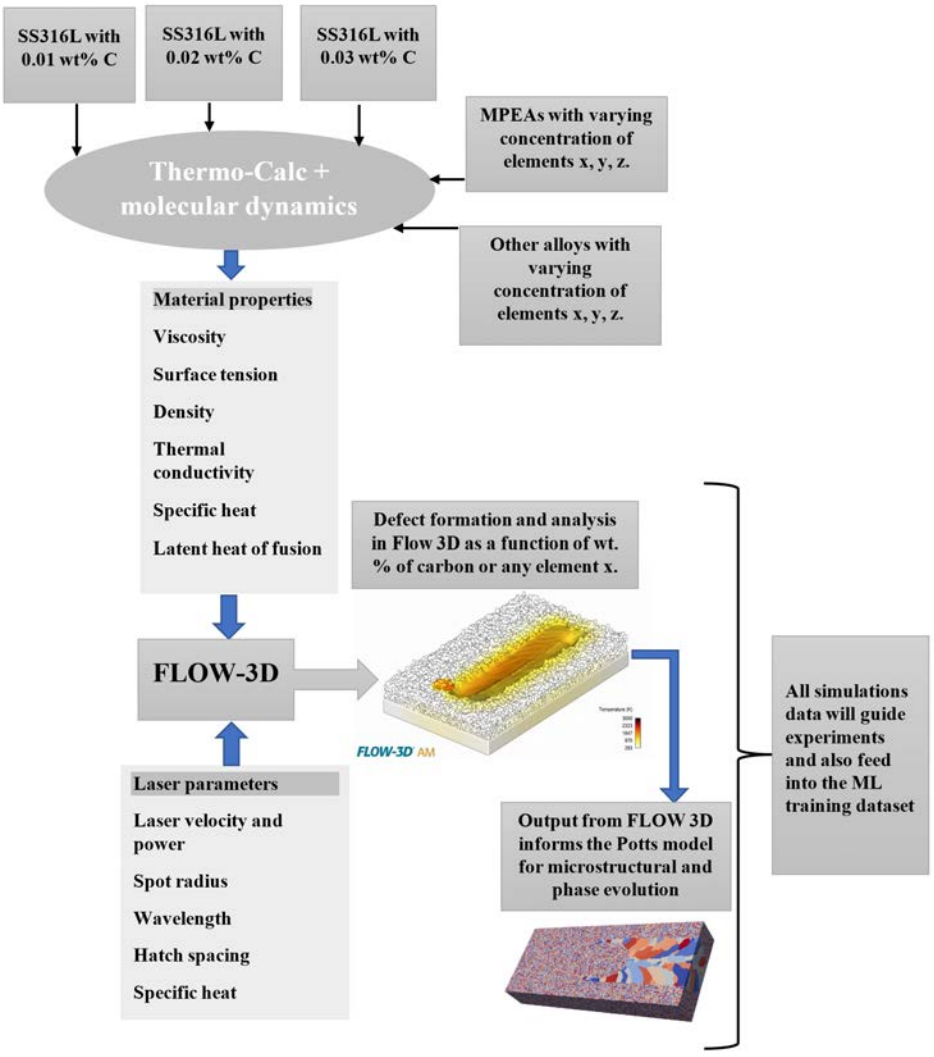

Figure 78. A schematic of the workflow explaining the properties generation from Thermo-Calc + molecular dynamics and informing the FLOW-3D software with the calculated properties to simulate the laser melting process.

The work will harness the potential of two computational tools: Thermo-Calc [166] and FLOW-3D (Version 2023R1; 2023; https://www.flow3d.com; Flow Science, Inc.) to study the effect of composition change on the printability of an alloy using laser melting. Thermo-Calc is a thermodynamic

calculation software package that can be used to predict phase equilibria, phase diagrams, and other thermodynamic properties of materials. Figure 79 shows an example of this type of simulation result. In this case, a FLOW3D-AM simulation is able to predict the formation of pores because of keyholing during deposition.

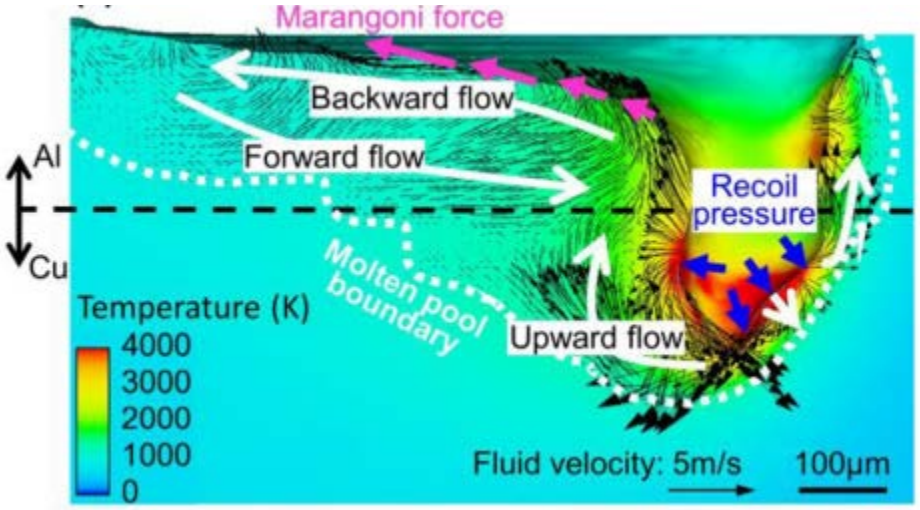

Figure 79. An example FLOW3D simulation performed by Huang et al., which reproduces the occurrence of keyholing in an Al–Cu laser weld [167].

To study the effect of the composition change of an alloy on its printability using laser melting, Thermo-Calc will be used to determine the thermodynamic properties of the alloy at different compositions and temperatures. This software will provide necessary information about the phase stability and solidification behavior of the alloy. With Thermo-Calc, phase diagrams, solidification paths, and other relevant thermodynamic properties can be obtained. For other properties not obtainable from Thermo-Calc, molecular dynamics simulations will be employed to calculate them. Once the thermodynamic data from Thermo-Calc have been obtained, FLOW-3D will be used to simulate the laser melting process. FLOW-3D allows researchers to model the fluid flow, heat transfer, and solidification phenomena that occur during laser melting. By inputting the thermodynamic data obtained from Thermo-Calc into FLOW-3D, it is possible to study how changes in alloy composition affect the heat transfer, melt pool dynamics, and solidification behavior during the laser melting process.

All the obtained compositions will then be studied as elaborated on in Figure 78. This information will allow researchers to make direct linkages between the macroscale process parameters simulated, the selected composition, and the emergent solidified microstructures.

7.5 MICROSTRUCTURAL SIMULATION

Computational fluid dynamics software such as FLOW3D-AM are capable of evaluating the evolving temperature and flow of molten material during deposition but typically do not efficiently account for the evolution of the solidified microstructure, which, in additively manufactured systems, can potentially melt and solidify multiple times. The associated evolution often has a great effect on fabricated material properties. Therefore, microstructural simulations of defect evolution under AM conditions will be studied using the Potts model. The Potts model, a q-state generalization of the Ising model, was first demonstrated as a computer simulation in 1983 to study grain growth in two dimensions [157]. Typical Potts model simulations are described as an evolving cellular grid of grain orientations. The total energy of such a system E is described by the generalized Equation 5:

$$E = \sum_{i=0}^{N} \left(U_i + \frac{1}{2} \sum_{j=0}^{NN} \gamma_{ij} \left[1 - \delta_{s_i s_j} \right] \right). \quad (5)$$

In this equation, each of the N cells, i, has an interfacial energy with each of its j nearest neighbors, γ_{ij}, and an internal energy U_i, which can be a function of atomic structure, composition, temperature, and other factors. For a given iteration of the Potts model algorithm, the probability of reorientation is calculated for a given cell based on the change of energy associated with the reorientation.

Nominally, the Potts model can be used to simulate the progression of grain growth as a function of various effects, such as grain boundary anisotropy and the effect of second phase pinning [168]. However, the Potts model has increasingly been used as a practical tool for the simulation of grain structure evolution during processes such as AM of metallic materials [169] and recrystallization response to mechanical deformation [170]. For example, this approach has been adapted into the software SPPARKS, which is capable of efficient parallel Potts model simulations in brute-force or hybrid kinetic Monte Carlo implementations [171].

Recently, PNNL has developed and tested a modification to the Potts model capable of simulating grain growth in systems containing an arbitrary number of phases. This approach resembles that of Graner and Glazier, who used a similar modification to the Potts model to simulate the behavior of cells in living tissues [171]. This method can be used to capture the evolution of pores within a deposited material by treating each pore formed within the solidifying melt as a separate phase.

8. CONCLUSION

Collaboration between ANL, INL, ORNL, and PNNL on the prioritization of current reactor materials for advanced manufacturing has led to the definition of a decision criteria matrix, allowing the systematic evaluation of nuclear candidate materials based on their technological readiness levels and their relevance to the nuclear industry and AMMT Program. ANL and PNNL focused on iron-based alloys, and INL and ORNL evaluated nickel-based alloys.

This report evaluated three nickel-based alloy categories: low-cobalt, high-temperature, and molten salt–compatible alloys. In-depth analysis of Alloy 718 highlighted the high potential of LPBF 718, with the routine fabrication of complex components using commercial 718 powder, and mechanical properties comparable with the properties of wrought 718. This study performed creep testing at 600°C–650°C on as-printed and annealed LPBF 718 specimens and obtained lifetimes similar to the lifetimes of wrought 718, with properties slightly greater in the annealed recrystallized conditions. The presence of stable, nanosize γ′ and γ″ precipitates after the aging treatments explains the excellent strength of the alloy, and reducing the volume fraction of deleterious Laves and δ phases in the grain and at grain boundaries could lead in creep ductility improvement. In-depth analysis of Alloy 625 was also conducted, and it was concluded that both alloys could be of great interest to the AMMT Program because of the alloy printability, significant experience from industry, and available data indicating that AM properties similar to the properties of wrought alloys can be achieved as long as the appropriate heat treatment is carried out. The γ′strengthened Alloy 282 was also evaluated in depth because of its superior creep strength at high temperature compared with Alloys 617 and 282 and their powder availability as a commercial product. Although the alloy is not currently considered for nuclear applications, fabrication of complex LPBF 282 components has been achieved owing to the great printability of the alloy when compared with other γ′ superalloys. The alloy was produced at ORNL's MDF using a Renishaw AM250 machine, and a central composite design approach was employed to determine the optimum printing parameters. Sufficient material has been produced to conduct tensile, creep, and fatigue testing at ORNL and INL.

The Renishaw machine was equipped with new cameras, and the in situ data generated during printing were integrated into the AMMT digital manufacturing framework using the Peregrine software.

An extensive study of LPBF 282 microstructure evolution during annealing at high temperatures was performed by INL on material provided by EOS. Recrystallization of the as-printed structure was achieved, which is desirable to reduce or remove the anisotropy in the mechanical properties. The 1,180°C, 1 h recrystallization heat treatment is considered the most promising because it resulted in a near-fully recrystallized structure, and the grain size had not grown significantly. Higher-temperature heat treatments resulted in overly large grains, which are a concern for the high-temperature fatigue properties.

There are a number of additional likely useful candidates for LPBF-printed nickel alloys; however, currently, high-temperature property data are currently available in limited amounts for these LPBF materials. Except for Alloys 718, 625, and 282, the other alloys considered in this report are not readily available in powder form for use in LPBF manufacturing. Some of the alloys that are not readily available in powder form, such as Hastelloy N and Haynes 244, are still of interest because of their specific properties (i.e., superior molten salt corrosion resistance).

A total of six alloys—three austenitic SSs and three ferritic/martensitic steels—were downselected. Once the alloys were selected based on the matrix, obtaining powders for 3D printing proved to be the biggest bottleneck in terms of advancing the work. The powder availability will be of primary concern in the future, although obtaining smaller quantities of powders for research will not be financially advisable to industrial scale-up work.

Single-track experiments were performed on one alloy class each (A709 for austenitic and Grade 91 for ferritic/martensitic) to optimize the process parameters for full 3D printed blocks. In total, 72 conditions were used for each of the alloy classes. Characterizing via optical imaging helped narrow down the process parameters for each class.

In total, 60 blocks were printed for the initial assessment. Ten different conditions were printed for each of the six alloys to see if defect-free, high-density parts could be produced. Initial assessment using optical imaging, SEM, and EBSD showed that four out of six alloys had good, consistent microstructures with density >99%. The prints of the AFA and the D9 showed extensive cracking likely owing to the lack of control of the chamber atmosphere because of a leaking issue. These alloys will be printed again using the same parameters to isolate the issue and better understand the effect of process parameters on microstructures. Martensite was observed in HT9 but was not observed in Grade 91 and Grade 92, which needs to be further studied.

This exercise proves that the AM of the selected current iron-based reactor materials, either austenitic SS or ferritic/martensitic steels, is very feasible, and more work needs to be done to understand the microstructure evolution during the depositions and to further optimize the final microstructures. In particular, large-scale samples of optimized conditions need to be built for mechanical, corrosion, and irradiation testing, and postbuild treatment and thermal stability of the microstructures needs to be studied.

9. ACKNOWLEDGEMENTS

The authors would like to thank K. Carver, J. Moser, D. Newberry, and T. Lowe at ORNL for their help with the experimental work, as well as K. Woodbury at INL for assistance in encapsulating the additively manufactured Alloy 282 specimens. H. Hyer and P. Fernandez-Zelaia are acknowledged for carefully reviewing the manuscript. EOS Sweden provided additively manufactured Alloy 282 for the preliminary studies discussed within this report, and Haynes International and Special Metals Inc. are acknowledged

for their useful discussions on potential nickel alloys of interest for this study. This research was funded by the US Department of Energy, Office of Nuclear Energy, Advanced Materials and Manufacturing Technologies Program, with programmatic guidance provided by Meimei Li at Argonne National Laboratory, Ryan Dehoff at Oak Ridge National Laboratory, and Dirk Cairns-Gallimore at the US Department of Energy.

10. REFERENCES

1. I. Gibson, D. Rosen, B. Stucker, M. Khorasani, "Additive Manufacturing Technologies", Vol. 17 Springer (2021).
2. A. Ben-Ner and E. Siemsen, "Decentralization and Localization of Production: The Organizational and Economic Consequences of Additive Manufacturing (3D Printing)", Managing Technology, 59, 5-23 (2017).
3. B. R. Betzler, B. J. Ade, P. K. Jain, A. J. Wysocki, P. C. Chesser, W. M. Kirkland, M. S. Cetiner, A. Bergeron, F. Heidet & K. A. Terrani, "Conceptual Design of the Transformational Challenge Reactor, Nuclear Science and Engineering", 196, 1399-1424 (2022).
4. J. Haley, C. Leach, B. Jordan, R. Dehoff and V. Pacquit, "In-situ digital image correlation and thermal monitoring in directed energy deposition additive manufacturing", Optics express, 29, 7, 9927-9941 (2021).
5. A. Huning. A. Smith, L. Scime, M. Russell, A. Coates, V. Paquit, R. Dehoff, "Advancement of Certification Methods and Applications for Industrial Deployments of Components Derived from Advanced Manufacturing Technologies", ORNL report, ORNL/TM-2022/2654 (2022).
6. Z. Chen, C. Han, M. Gao, S. Y. Kandukuri and K. Zhou, "A review on qualification and certification for metal additive manufacturing", Virtual and Physical Prototyping, 17:2, 382-405 (2022).
7. M. Li, D. Andersson, R. Dehoff, A. Jokisaari, I. Van Rooyen, and D. Cairns-Gallimore, "Advanced Materials and Manufacturing Technologies (AMMT), 2022 Roadmap", ANL report, ANL-23/12 (2022).
8. T. Hartmann, S. Maloy and M. Komarasamy, "Materials Scorecards, Phase 2, Advanced Materials and Manufacturing Technology", PNNL report, PNNL-32744 (2022).
9. ASTM E139 – 11, Standard Test Methods for Conducting Creep, Creep-Rupture, and Stress-Rupture Tests of Metallic Materials (2018).
10. ASTM E606/E606M – 21, Standard Test Method for Strain-Controlled Fatigue Testing (2021).
11. ASTM E466 – 21, Standard Practice for Conducting Force Controlled Constant Amplitude Axial Fatigue Tests of Metallic Materials (2021).
12. ASTM E2714 – 13, Standard Test Method for Creep-Fatigue Testing (2020).
13. ASTM E8/E8M – 22, Standard Test Methods for Tension Testing of Metallic Materials (2022).
14. ASTM E21 – 20, Standard Test Methods for Elevated Temperature Tension Tests of Metallic Materials (2020).
15. M. Griffiths, Chapter 9, "Ni-based alloys for reactor internals and steam generator applications", Structural Alloys for Nuclear Energy Applications, Edited by G. R. Odette and S. J. Zinkle (2019).

16. A. F. Rowcliffe, L. K. Mansur, D. T. Hoelzer, and R. K. Nanstad, “Perspectives on radiation effects in nickel-base alloys for applications in advanced reactors”, Journal of Nuclear Materials, vol. 392, 341-352 (2009).

17. M. Griffiths and R. Boothby, “Radiation Effects in Nickel-Based Alloys,” in Comprehensive Nuclear Materials, 2nd ed, 334-371 (2020).

18. T. Yonezawa, “Nickel-Based Alloys,” in Comprehensive Nuclear Materials, 7, 319-354 (2020).

19. N.J. Harrison, I. Todd, K. Mumtaz, Reduction of micro-cracking in nickel superalloys processed by Selective Laser Melting: A fundamental alloy design approach, Acta Materialia, 94, 59-68 (2015).

20. Y.B.T. Tang, C. Panwisawas, J.N. Ghoussoub, Y.L. Gong, J.W.G. Clark, A.A.N. Nemeth, D.G. McCartney, R.C. Reed, Alloys-by-design: Application to new superalloys for additive manufacturing, Acta Materialia, 202, 417-436 (2021).

21. K.A. Mumtaz, P. Erasenthiran, N. Hopkinson, High density selective laser melting of Waspaloy I, Journal of Materials Processing Technology, 195, 77-87 (2008).

22. M. Salarian, H. Asgari, M. Vlasea, Pore space characteristics and corresponding effect on tensile properties of Inconel 625 fabricated via laser powder bed fusion, Mat Sci Eng a-Struct, 769 (2020).

23. D. Tomus, P.A. Rometsch, M. Heilmaier, X.H. Wu, Effect of minor alloying elements on crack-formation characteristics of Hastelloy-X manufactured by selective laser melting, Additive Manufacturing, 16, 65-72 (2017).

24. R. Engeli, T. Etter, S. Hovel, K. Wegener, Processability of different IN738LC powder batches by selective laser melting, Journal of Materials Processing Technology, 229, 484-491 (2016).

25. A. Kracke, “Superalloys, the most successful alloy system of modern times – Past, Present and future”, Proceedings of the 7th International Symposium on Superalloy 718 and its derivatives, Edited by E.O Ott et al., TMS (The Minerals, Metals & Material Society), 13-50 (2010).

26. H. L. Eiselstein and D. J. Tillack, “The invention of and definition of alloy 625”, Superalloys 1992, Edited by E.A. Loria et al., 1-14 (1991).

27. https://www.additivemanufacturing.media/news/senvol-commercializes-siemens-energys-material-databases

28. https://www.makepartsfast.com/shell-and-ge-additive-show-joint-design-and-engineering-project-at-formnext/

29. https://www.ge.com/additive/press-releases/turn-larger-lighter-additive-parts

30. S. Taller, A. Le Coq, C. Massey, J. Werden, M. Lynch and K. Linton, “ Report on Evolution of Inconel 718 Following HFIR Irradiation”, ORNL report, ORNL/TM-2022/2600 (2022).

31. https://www.praxairsurfacetechnologies.com/en/materials-and-equipment/materials/additive-manufacturing-powders?tab=truform-product-portfolio

32. https://www.carpenteradditive.com/metal-powders/high-temperature-nickel-base

33. S. Sanchez, P. Smith, Z. Xu, G. Gaspard, C. J. Hyde, W. W. Wits, I.A. Ashcroft, H. Chen, A. T. Clare, “Powder Bed Fusion of nickel-based superalloys: A review”, International Journal of Machine Tools & Manufacture, 165, 103729 (2021).

34. S. Catchpole-Smith, N. Aboulkhair, L. Parry, C. Tuck, I.A. Ashcroft, A. Clare, “Fractal scan strategies for selective laser melting of ‘unweldable’ nickel superalloys”, Additive Manufacturing 15, 113-122 (2017).

35. K. Moussaoui, W. Rubio, M. Mousseigne, T. Sultan, F. Rezai, “Effects of Selective Laser Melting additive manufacturing parameters of Inconel 718 on porosity, microstructure and mechanical properties”, Mater. Sci. Eng. A 735, 182-190 (2018).

36. A. Hilaire, E. Andrieu, X. Wub, “High-temperature mechanical properties of alloy 718 produced by laser powder bed fusion with different processing parameters”, Additive Manufacturing, 26, 147-160 (2019).

37. K. Gruber a, W. Stopyra, K. Kobiela, B. Madejski, M. Malicki, T. Kurzynowski, “Mechanical properties of Inconel 718 additively manufactured by laser powder bed fusion after industrial high-temperature heat treatment”, Journal of Manufacturing Processes, 73, 642-659 (2022).

38. E. M. Fayed, M. Saadati, D. Shahriari, V. Brailovski, M. Jahazi, & M. Medraj, “Effect of homogenization and solution treatments time on the elevated-temperature mechanical behavior of Inconel 718 fabricated by laser powder bed fusion”, Scientific Reports, 11, 2020 (2021).

39. X. Li, J.J. Shi, C.H. Wang, G.H. Cao, A.M. Russell, Z.J. Zhou, C.P. Li, G.F. Chen, “Effect of heat treatment on microstructure evolution of Inconel 718 alloy fabricated by selective laser melting”, Journal of Alloys and Compounds, 764, 639-649 (2018).

40. S. Taller and T. Austin, “Using post-processing heat treatments to elucidate precipitate strengthening of additively manufactured superalloy 718”, Additive Manufacturing”, 60, 103280 (2022).

41. L. Huang, Y. Cao, J. Zhang, X. Gao, G. Li, Y. Wang, “Effect of heat treatment on the microstructure evolution and mechanical behaviour of a selective laser melted Inconel 718 alloy”, Journal of Alloys and Compounds 865, 158613 (2021).

42. E. Hosseini and V.A. Popovich, “A review of mechanical properties of additively manufactured Inconel 718”, Additive Manufacturing, 30, 100877 (2019).

43. Y. Gao, D. Zhang, M. Cao, R. Chen, Z. Feng, R. Poprawe, J.H. Schleifenbaum, S. Ziegler, “Effect of δ phase on high temperature mechanical performances of Inconel 718 fabricated with SLM process”, Mater. Sci. Eng. A. 767, 138327 (2019).

44. M. Komarasamy, S. Shukla, S. Williams, K. Kandasamy, S. Kelly, R.S. Mishra, “Microstructure, fatigue, and impact toughness properties of additively manufactured nickel alloy 718”, Additive Manufacturing 28, 661-675, (2019).

45. Kevinsanny, S. Okazaki, O. Takakuwa, Y. Ogawa, Y. Funakoshi, H. Kawashima, S. Matsuoka, H. Matsunaga, “Defect tolerance and hydrogen susceptibility of the fatigue limit of an additively manufactured Ni-based superalloy 718”, International Journal of Fatigue 139, 105740 (2020).

46. S. Sanchez, C. Hyde, I. Ashcroft, G. Ravi, A. Clare, “Multi-laser scan strategies for enhancing creep performance in LPBF”, Additive Manufacturing 41, 101948 (2021).

47. M. Chang, A.K. Koul, P. Au, and T Terada, “Damage Tolerance of Wrought Alloy 718 Ni.Fe-Base Superalloy”, Journal of Materials engineering and Performance, 3, 356-366 (1994).

48. C. R. Brinkman’, M. K. Booke, and J. L. Ding, “Creep and Creep-rupture behavior of alloy 718”, Proceedings of Superalloys 718,625 and Various Derivatives, Edited by Edward A. Iaria, The Minerals, Metals & Materials Society, 519-536 (1991).

49. Y.-L. Kuo, S. Horikawa, K. Kakehi, “Effects of build direction and heat treatment on creep properties of Ni-base superalloy built up by additive manufacturing”, Scripta Materialia 129, 74-78 (2017).

50. Y.-L. Kuo, T. Nagahari, K. Kakehi, “The effect of post-processes on the microstructure and creep properties of Alloy718 built up by selective laser melting”, Materials 11, 6, 996 (2018).

51. S. Wu, H.Z. Peng, X. Gao, P.D. Hodgson, H.Y. Song, Y.M. Zhu, Y. Tian, A.J. Huang, “Improving creep property of additively manufactured Inconel 718 through specifically-designed post heat treatments”, Materials Science & Engineering A 857, 144047 (2022)

52. M.M.Kirka, F. Medinac,R. Dehoff, A. Okello, “Mechanical behavior of post processed Inconel 718 manufactured through the electron beam melting process”, Materials Science & Engineering A 680, 338-346 (2017).

53. S. Pratheesh Kumar, S.Elangovan, R.Mohanraj, J.R.Ramakrishna, “A review on properties of Inconel 625 and Inconel 718 fabricated using direct energy deposition”, Materials Today: Proceedings 46, 7892-7906 (2021).

54. X. Xu, J. Ding, S. Ganguly, S. Williams, “Investigation of process factors affecting mechanical properties of INCONEL 718 superalloy in wire + arc additive manufacture process”, Journal of Materials Processing Tech., 265 201-209 (2019).

55. P. Nandwana,A. M.Elliott, D. Siddel, A. Merriman,W. H.Peter, S., S. Babu, “Powder bed binder jet 3D printing of Inconel 718:Densification, microstructural evolution and challenges”, Current Opinion in Solid State and Materials Science 21, 207-218 (2017).

56. Inconel 625, in, Special Metals Corporation (2013).

57. H. Wong, K. Dawson, G.A. Ravi, L. Howlett, R.O. Jones, C.J. Sutcliffe, Multi-Laser Powder Bed Fusion Benchmarking-Initial Trials with Inconel 625, International Journal of Advanced Manufacturing Technology, 105, 2891-2906 (2019).

58. G. Marchese, M. Lorusso, S. Parizia, E. Bassini, J.W. Lee, F. Calignano, D. Manfredi, M. Terner, H.U. Hong, D. Ugues, M. Lombardi, S. Biamino, Influence of heat treatments on microstructure evolution and mechanical properties of Inconel 625 processed by laser powder bed fusion, Mat Sci Eng a-Struct, 729, 64-75 (2018).

59. Z.H. Tian, C.Q. Zhang, D.Y. Wang, W. Liu, X.Y. Fang, D. Wellmann, Y.T. Zhao, Y.T. Tian, A Review on Laser Powder Bed Fusion of Inconel 625 Nickel-Based Alloy, Appl Sci-Basel, 10 (2020).

60. I. Yadroitsev, M. Pavlov, P. Bertrand, I. Smurov, Mechanical properties of samples fabricated by selective laser melting, 14èmes Assises Européennes du Prototypage & Fabrication Rapide, 24-25 (2009).

61. J. Lee, M. Terner, S. Jun, H.U. Hong, E. Copin, P. Lours, Heat treatments design for superior high-temperature tensile properties of Alloy 625 produced by selective laser melting, Mat Sci Eng a-Struct, 790 (2020).

62. K.S. Kim, T.H. Kang, M.E. Kassner, K.T. Son, K.A. Lee, High-temperature tensile and high cycle fatigue properties of inconel 625 alloy manufactured by laser powder bed fusion, Additive Manufacturing, 35 (2020).

63. K.T. Son, T.Q. Phan, L.E. Levine, K.S. Kim, K.A. Lee, M. Ahlfors, M.E. Kassner, The creep and fracture properties of additively manufactured inconel 625, Materialia, 15 (2021).

64. N. Ramenatte, A. Vernouillet, S. Mathieu, A.V. Put, M. Vilasi, D. Monceau, A comparison of the high-temperature oxidation behaviour of conventional wrought and laser beam melted Inconel 625, Corrosion Science, 164 (2020).

65. E.R. Lewis, M.P. Taylor, B. Attard, N. Cruchley, A.P.C. Morrison, M.M. Attallah, S. Cruchley, Microstructural characterisation and high-temperature oxidation of laser powder bed fusion processed Inconel 625, Materials Letters, 311 (2022).

66. M. Andurkar, J. Gahl, B. Prorok, T. Keya, G. Harvill, S. Thompson, Effects of Build Orientation and Heat Treatment on Neutron Irradiation Hardening in Inconel 625 Fabricated via Laser Powder Bed Fusion, in: 2021 International Solid Freeform Fabrication Symposium, University of Texas at Austin, Austin (2021).

67. T. Keya, V' O'Donnell, J. Lieben, A. Romans, G. Harvill, M. Andurkar, J. Gahl, S.M. Thompson, B.C. Prorok, Effects of Heat Treatment and Fast Neutron Irradiation on the Microstructure and Microhardness of Inconel 625 Fabricated via Laser-Powder Bed Fusion, in: 2021 International Solid Freeform Fabrication Symposium, University of Texas at Austin (2021).

68. I. Cieslik, M. Duchna, T. Plocinski, E. Wyszkowska, A. Azarov, M. Zieniuk, Ion irradiation effect on the microstructure of Inconel 625 obtained by Selective Laser Melting and by the metallurgical process, Surf Coat Tech, 396 (2020).

69. J. Yang, X. Liu, M. Song, L. He, S. Bankson, M. Hamilton, B. Prorok, X. Lou, "Sensitization, desensitization, and carbide evolution of Alloy 800H made by laser powder bed fusion", Additive Manufacturing 50, 102547 (2022).

70. J. Yang, M. Song, L.R. Hawkins, X. Liu, L. He, X. Lou, "Effects of heat treatment on corrosion fatigue and stress corrosion crack growth of additive-manufactured Alloy 800H in high-temperature water", Corrosion Science, 191, 109739 (2021).

71. Haynes 282 Alloy, in, Haynes International Corporation (2021).

72. Haynes 244 Alloy, in, Haynes International Corporation (2022).

73. Inconel Alloy 617, in, Special Metals Corporation (2005).

74. Inconel Alloy 740H, in, Special Metals Corporation (2014).

75. T.M. Smith, C.A. Kantzos, N.A. Zarkevich, B.J. Harder, M. Heczko, P.R. Gradl, A.C. Thompson, M.J. Mills, T.P. Gabb, J.W. Lawson, A 3D printable alloy designed for extreme environments, Nature (2023).

76. R.W. Swindeman, The mechanical properties of INOR-8, ORNL report, ORNL-2780 (1961).

77. Haynes 230 Alloy, in, Haynes International Corporation (2023).

78. Haynes 718 Alloy, in, Haynes International Corporation (2023).

79. R. Wright, "Draft ASME Boiler and Pressure Vessel Code Cases and Technical Bases for Use of Alloy 617 for Constructions of Nuclear Component Under Section III, Division 5", INL report, INL/EXT-15-36305 Revision 2 (2021).

80. Haynes 233 Alloy, in, Haynes International Corporation (2022).

81. A. S. Shaikh, F. Schulz, K. Minet-Lallemand, E. Hryh, "Microstructure and mechanical properties of Haynes 282 superalloy produced by laser powder bed fusion", Materials Today Communications, 26, 102038 (2021).

82. Lee, M. Terner, S. Jun, H.U. Hong, E. Copin, P. Lours, Heat treatments design for superior high-temperature tensile properties of Alloy 625 produced by selective laser melting, Materials Science and Engineering A, 790, 139720 (2020).

83. B.A. Pint, Performance of Wrought Superalloys in Extreme Environments, in: Proceedings of th^{e} 9th International Symposium on Superalloy 718 & Derivatives: Energy, Aerospace, and Industrial Applications, 165-178 (2018).

84. L.M. Pike, “Development of a fabricable gamma-prime strengthened superalloy”, in: R.C. Reed, K.A. Green, P. Caron, T.P. Gabb, M.G. Fahrmann, E.S. Huron, Shiela A. Woodard (Eds.), In Superalloys 2008, 191–200 (2008).

85. R. Viswanathan, J. Shingledecker, and R. Purgert, “Evaluating Materials Technology for Advanced Ultrasupercritical Coal-Fired Plants,” Power, 154, 41-45 (2010).

86. Jablonski, P.D., Hawk, J.A., Cowen, C.J., Maziasz, P.J., “Processing of Advanced Cast alloys for A-USC Steam Turbine Applications”, JOM, 64, 271-279 (2012).

87. Shen C., “Modeling Creep-Fatigue-Environment Interactions in Steam Turbine Rotor Materials for Advanced Ultra-supercritical Coal Power Plants”, GE Global Research Final Report, DOE/NETL Cooperative Agreement DE-FE0005859 (2014).

88. B. A. Pint, Hong Wang, C. Shane Hawkins, Kinga A. Unocic, “Technical Qualification of New Materials for High Efficiency Coal-Fired Boilers and Other Advanced FE Concepts: Haynes® 282® ASME Boiler and Pressure Vessel Code Case”, ORNL report, ORNL/TM-2020/1548 (2020).

89. B. A. Pint and J. R. Keiser, “Effect of Pressure and Thermal Cycling on Long-Term Oxidation in Supercritical CO_2,” NACE Paper C2019-12750, Houston, TX, presented at NACE Corrosion 2019, Nashville, TN (2019).

90. V. P. Deodeshmukh and B. A. Pint, “Long-Term Performance of High Temperature Alloys in Oxidizing Environments and Supercritical CO_2,” in Proceedings of the Joint EPRI – 123HiMAT International Conference on Advances in High Temperature Materials, J. Shingledecker and M. Takeyama eds., ASM International, Materials Park, OH, 953-966 (2020).

91. T. Dudziak, K. Jura, A. Polkowska, V. Deodeshmukh, M. Warmuzek, M. Witkowska, W. Ratuszek, K. Chrusciel, Steam Oxidation Resistance of Advanced Steels and Ni-Based Alloys at 700 degrees C for 1000 h, Oxidation of Metals, 89, 755-779 (2018).

92. B.A. Pint and R. Pillai, Lifetime Model Development for Supercritical CO2 CSP Systems, ORNL report, ORNL/SPR-2019/1134 (2019).

93. B.A. Pint, R. Pillai M. J. Lance and J. R. Keiser, Effect of Pressure and Thermal Cycling on Long-Term Oxidation in CO2 and Supercritical CO2, Oxidation of metals, 94, 505-526 (2020).

94. R. Pillai, M. Romedenne and S. Lee, “Development of an Open-source Alloy selection and Lifetime assessment tool for structural components in CSP”, ORNL report, ORNL/TM-2021/2365 (2021).

95. R. Rajan, Raytheon Technologies Research Center “Developing an Ultra-Compact, Topology-Optimized Heat Exchanger using Additive Manufacturing”, ARPA-E project.

96. C. Magnin, Z. Islam, M. Elbakhshwan, A. Brittan, D. J. Thoma. M. H.Anderson, “The performance of additively manufactured Haynes 282 in supercritical CO_2”, Materials Science & Engineering A 841, 143007 (2022).

97. Z. Islam, A. Kumar, A.B. Rankouhi, C. Magnin, M.H. Anderson, F.E. Pfefferkorn and D.J. Thoma, “A High-Throughput Method to Define Additive Manufacturing Process Parameters: Application to Haynes 282”, Metallurgical and Materials Transactions A, 53, 250-263 (2022).

98. J. Boswell, J. Jones, N. Barnard, D. Clark, M. Whittaker, R. Lancaster, “The effects of energy density and heat treatment on the microstructure and mechanical properties of laser additive manufactured Haynes 282”, Materials & Design 205, 109725(2021).

99. K.A. Christofidou, H.T. Pang, W. Li, Y. Pardhi, C.N. Jones, N.G. Jones, H.J. Stone, “Microstructural control and optimization of Haynes 282 manufactured through laser powder bed

fusion", in: S. Tin, M. Hardy, J. Clews, J. Cormier, Q. Feng, J. Marcin, C. O'Brien, A. Suzuki (Eds.), Superalloys 2020, Springer International Publishing, Cham, 1014-1023 (2020).

100. K.A. Unocic, D. Shin, X. Sang, E. Cakmak, P.F. Tortorelli, "Single-step aging treatment for a precipitation-strengthened Ni-based alloy and its influence on high-temperature mechanical behavior", Scripta Materialia 162, 416-420 (2019).

101. M. Romedenne, P. Stack, R. Pillai, S. Dryepondt, Isothermal and Cyclic Oxidation of Haynes 282 Processed by Electron Beam Melting (EBM) and Laser Powder Bed Fusion (LPBF) in Dry Air at 800 and 950 degrees C, JOM, 74, 1707-1718 (2022).

102. K.A. Unocic, M.M. Kirka, E. Cakmak, D. Greeley, A.O. Okello, S. Dryepondt, "Evaluation of additive electron beam melting of Haynes 282 alloy", Materials Science & Engineering A 772, 138607 (2020).

103. S. Dryepondt, M. M. Kirka, P. Fernandez-Zelaia and K. A. Unocic, "Microstructure and mechanical properties of Haynes 282 Fabricated by Electron Beam Melting", Joint EPRI-123HiMAT International Conference on Advances in High-Temperature Materials, edited by John Shingledecker and Masao Takeyama (2019).

104. P. Fernandez-Zelaia, J. O. Rojas, J. Ferguson, S. Dryepondt, and M. M. Kirka, "Fatigue crack growth resistance of a mesoscale composite microstructure Haynes 282 fabricated via electron beam melting additive manufacturing", Journal of Materials Science, 57, 9866-9884 (2022).

105. T. Hassel1 & T. Carstensen, "Properties and anisotropy behaviour of a nickel base alloy material produced by robot-based wire and arc additive manufacturing", Welding in the World, 64, 1921-1931 (2020).

106. B. Avinash , K. Manikanda Subramanian, and V. Rajkumar, "Microstructure, Mechanical Properties and Corrosion Behavior of Inconel 617 Superalloy Fabricated by Wire Arc Additive Manufacturing", Journal of Materials Engineering and Performance, 32, 6270-6280 (2023).

107. K. Momeni, "Sensitivity of laser powder bed fusion additive manufactured HAYNES230 to composition and print parameters", Journal of materials research and technology, 15, 6453-6463 (2021).

108. Y. Zhao, Z. Ma, L. Yu, Y. Liu, "New alloy design approach to inhibiting hot cracking in laser additive manufactured nickel-based superalloys", Acta Materialia 247, 118736 (2023).

109. X. Liu, R. Hu, X. Luo, C. Yang, X. Gao, " A high-strength Ni–Cr–W based superalloy prepared by laser powder bed fusion: printability, microstructure and tensile properties", Materials Science & Engineering A, 853, 143744 (2022).

110. Haynes 233 Alloy, in, Haynes International Corporation (2023).

111. T. K. Roche, The Influence of Composition Upon the 1500°F Creep-Rupture Strength and Microstructure of Molybdenum-Chromium-Iron-Nickel-Base Allovs, ORNL report 2524 (1958).

112. R. Pillai, Q.Q. Ren, Y-F. Su, R. Kurfess, T. Feldhausen, S. Nag, "Leveraging additive manufacturing to fabricate high temperature alloys with co-designed mechanical properties and environmental resistance", Proceedings of ASME Turbo Expo 2023, Boston MA, GT2023-103009 (2023).

113. F. Bachmann, R. Hielscher, H. Schaeben, "Texture analysis with MTEX- Free and open-source software toolbox", Solid State Phenom, 160, 63-68 (2010).

114. L. Scime J. Haley V. Paquit, "Summary of Methodology for Mitigating Risks Associated with Licensing and Qualifying AM Nuclear Materials", ORNL report, ORNL/SPR-2019/1355 (2019).

115. H. C. Hyer, D. C. Sweeney Christian M. Petrie, “Summary of Methodology for Mitigating Risks Associated with Licensing and Qualifying AM Nuclear Materials”, ORNL report, ORNL/TM-2023/2851 (2023).

116. A. Deshpande, S.D. Nath, S. Atre, K. Hsu, Effect of Post Processing Heat Treatment Routes on Microstructure and Mechanical Property Evolution of Haynes 282 Ni-Based Superalloy Fabricated with Selective Laser Melting (SLM), Metals, 10 (2020).

117. D. R. Harries, J. Standring, W. D. Barnes, and G. J. Lloyd, “U. K. Fast Reactor Materials Programme.,” ASTM Special Technical Publication, 1197-1217 (1982).

118. T.-L. Sham, Y. Wang, R. Bass, and X. Zhang, “A709 Qualification Plan Update and Mechanical Properties Data Assessment” (2022).

119. “Report on the Initial Loading of SS3 Specimens from the First Commercial Heat of Alloy 709 in Sodium Materials Test Loops for Long-term Exposure Applied Materials Division.”

120. Y. Wang, P. Hou, R. E. Bass, X. Zhang, and T.-L. Sham, “Interim Mechanical Properties Data from FY22 ORNL Testing of A709 with Precipitation Treatment for ASME Code Case Data Package”, ORNL report, TM-2022/2593 (2022).

121. F. A. Garner, M. L. Hamilton, C. R. Eiholzer, M. B. Toloczko, and A. S. Kunfar, Influence of cold worklevel on Ti4E irradiation creep and creep rupture of Titanium-modified austenitic stainless steels”, report PNNL-SA-19959 (1992).

122. S. Venkadesan, A. K. Bhaduri, P. Rodriguez, and K. A. Padmanabhan, “Effect of ageing on the microstructural stability of cold-worked titanium-modified 15Cr-15Ni-2.5Mo austenitic stainless steel”, Journal of Nuclear Materials, 186, 177-184 (1992).

123. N.S. Cannon, F.H. Huang, M.L. Hamilton, “Transient and Static Mechanical Properties of D9 Fuel Pin Cladding and Duct Material Irradiated to High Fluence”, report WHC-SA-0757 (1990).

124. A. Banerjee, S. Raju, R. Divakar, E. Mohandas, G. Panneerselvam, and M. P. Antony, “Thermal property characterization of a titanium modified austenitic stainless steel (alloy D9),” Journal of Nuclear Materials, 347, 20-30 (2005).

125. W. Zhai, W. Zhou, and S. M. L. Nai, “Grain refinement of 316L stainless steel through in-situ alloying with Ti in additive manufacturing,” Materials Science and Engineering: A, 840, 142912 (2022).

126. S. Bin Han, Y. S. Lee, S. H. Park, and H. Song, “Ti-containing 316L stainless steels with excellent tensile properties fabricated by directed energy deposition additive manufacturing,” Materials Science and Engineering*: A*, 862, 144414 (2023).

127. A. Alamo, H. Regle, G. Pons, and J. L. Béchade, “Microstructure and Textures of ODS Ferritic Alloys Obtained by Mechanical Alloying,” Materials Science Forum, 88-90, 183-190 (1992).

128. S. Ukai *et al.*, “Alloying design of oxide dispersion strengthened ferritic steel for long life FBRs core materials,” Journal of Nuclear Materials, 204, 65-73 (1993).

129. M. P. Brady, Y. Yamamoto, M. L. Santella, and B. A. Pint, “Effects of minor alloy additions and oxidation temperature on protective alumina scale formation in creep-resistant austenitic stainless steels,” Scripta Materialia, 57, 1117-1120 (2007).

130. Y. Yamamoto, G. Muralidharan, and M. P. Brady, “Development of L12-ordered Ni3(Al,Ti)-strengthened alumina-forming austenitic stainless steel alloys,” Scripta Materialia, 69, 816-819 (2013).

131. M. P. Brady, J. Magee, Y. Yamamoto, D. Helmick, and L. Wang, “Co-optimization of wrought alumina-forming austenitic stainless steel composition ranges for high-temperature creep and oxidation/corrosion resistance,” Materials Science and Engineering: A, 590, 101-115 (2014).

132. R. L. Klueh and A. T. Nelson, “Ferritic/martensitic steels for next-generation reactors,” Journal of Nuclear Materials, 371, 37-52 (2007).

133. N. Sridharan and K. Field, “A Road Map for the Advanced Manufacturing of Ferritic-Martensitic Steels,” Fusion Science and Technology, 75, 264-274 (2019).

134. Y. Chen, “Irradiation effects of HT-9 martensitic steel,” Nuclear Engineering and Technology, 45, 311-322 (2013).

135. N. Sridharan and K. G. Field, “Preliminary Characterization and Mechanical Performance of Additively Manufactured HT9”, ORNL report, SPR-2018-780 (2018).

136. G. Gupta, P. Ampornrat, X. Ren, K. Sridharan, T. R. Allen, and G. S. Was, “Role of grain boundary engineering in the SCC behavior of ferritic-martensitic alloy HT-9,” Journal of Nuclear Materials, 361, 160-173 (2007).

137. P. Xiu *et al.*, “Microchemical evolution of irradiated additive-manufactured HT9,” Journal of Nuclear Materials, 559, 153410 (2022).

138. “ASTM A213/A213M Tubing Standard specification − 19a Standard Specification for Seamless Ferritic and Austenitic Alloy-Steel Boiler, Superheater, and Heat-Exchanger Tubes 1”

139. T. Hatakeyama, K. Sawada, M. Suzuki, and M. Watanabe, “Microstructure development of modified 9Cr-1Mo steel during laser powder bed fusion and heat treatment,” Additive Manufacturing, 61, 103350 (2023).

140. L. Tan, W. Zhong, Y. Yang, K. G. Field, N. Sridharan, and A. T. Nelson, “Creep behavior of an additively manufactured 9Cr steel in the as-built condition”, Journal of Nuclear Materials, 570, 153943 (2022).

141. J. Feng, P. Zhang, Z. Jia, Z. Yu, C. Fang, H. Yn, H. Shi, Y. Tin and F. Xie, “Laser additive manufacturing and post-heat treatment on microstructure and mechanical properties of 9Cr steel,” International Journal of Pressure Vessels and Piping, 198, 104681 (2022).

142. W. Zhong, N. Sridharan, D. Isheim, K.G. Field, Y. Yang, K. Terrani and L. Tan, “Microstructures and mechanical properties of a modified 9Cr ferritic-martensitic steel in the as-built condition after additive manufacturing,” Journal of Nuclear Materials, 545, 152742 (2021).

143. O. El-Atwani, B. P. Eftink, C. M. Cady, D. R. Coughlin, M. M. Schneider, and S. A. Maloy, “Enhanced mechanical properties of additive manufactured Grade 91 steel,” Scripta Materialia, 199, 113888 (2021).

144. B. P. Eftink, D.A. Vega, O.E. Atwani, D.J. Sprouster, Y. S. J. Yoo, T.E. Steckley, E. Aydogan, C.M. Cady, M. Al-Sheikhly, T.J. Lienert, S. A. Maloy, “Tensile properties and microstructure of additively manufactured Grade 91 steel for nuclear applications,” Journal of Nuclear Materials, 544, 152723 (2021).

145. F. Abe, “Precipitate design for creep strengthening of 9% Cr tempered martensitic steel for ultra-supercritical power plants,” Science and Technology of Advanced Materials, 9, 013002 (2008).

146. X. Zhou, C. Liu, L. Yu, Y. Liu, and H. Li, “Phase Transformation Behavior and Microstructural Control of High-Cr Martensitic/Ferritic Heat-resistant Steels for Power and Nuclear Plants: A Review,” Journal of Materials Science & Technology, 31, 235-242 (2015).

147. C. Cabet, F. Dalle, E. Gaganidze, J. Henry, and H. Tanigawa, “Ferritic-martensitic steels for fission and fusion applications,” Journal of Nuclear Materials, 523, 510-537 (2019).

148. W. J. Sames, F. A. List, S. Pannala, R. R. Dehoff, and S. S. Babu, “The metallurgy and processing science of metal additive manufacturing,” International Materials Reviews, 61, 315-360 (2016).

149. T. Ronneberg, C. M. Davies, and P. A. Hooper, “Revealing relationships between porosity, microstructure and mechanical properties of laser powder bed fusion 316L stainless steel through heat treatment”, Material Design, 189, 108481 (2020).

150. B. Zhang, R. Seede, A. Whitt, D. Shoukr, X. Huang, I. Karaman, R. Arroyave, A. Elwany, “A printability assessment framework for fabricating low variability nickel-niobium parts using laser powder bed fusion additive manufacturing”, Rapid Prototyping Journal, 27, 9, 1737-1748 (2021).

151. M. Thomas, G.J. Baxter, I. Todd, “Normalised model-based processing diagrams for additive layer manufacture of engineering alloys, Acta Materialia”, 108, 26-35 (2016).

152. Z. Gan, O.L. Kafka, N. Parab, C. Zhao, L. Fang, O. Heinonen, T. Sun, W.K. Liu, “Universal scaling laws of keyhole stability and porosity in 3D printing of metals”, Nature communications, 12, 1, 2379 (2021).

153. C. Zhao, N.D. Parab, X. Li, K. Fezzaa, W. Tan, A.D. Rollett, T. Sun, “Critical instability at moving keyhole tip generates porosity in laser melting”, Science, 370, 6520, 1080-1086 (2020).

154. A. Caggiano, J. Zhang, V. Alfieri, F. Caiazzo, R. Gao, R. Teti, “Machine learning-based image processing for on-line defect recognition in additive manufacturing”, CIRP annals, 68, 1, 451-454 (2019).

155. L. Scime, J. Beuth, “A multi-scale convolutional neural network for autonomous anomaly detection and classification in a laser powder bed fusion additive manufacturing process”, Additive Manufacturing, 24, 273-286 (2018).

156. Y. Zhang, H.G. Soon, D. Ye, J.Y.H. Fuh, K. Zhu, “Powder-bed fusion process monitoring by machine vision with hybrid convolutional neural networks”, IEEE Transactions on Industrial Informatics, 16, 9, 5769-5779 (2019).

157. B. Zhang, S. Liu, Y.C. Shin, “In-Process monitoring of porosity during laser additive manufacturing process”, Additive Manufacturing, 28, 497-505 (2019).

158. R. Angelone, A. Caggiano, R. Teti, A. Spierings, A. Staub, K. Wegener, “Bio-intelligent selective laser melting system based on convolutional neural networks for in-process fault identification”, Procedia CIRP, 88, 612-617 (2020).

159. H. Baumgartl, J. Tomas, R. Buettner, M. Merkel, “A deep learning-based model for defect detection in laser-powder bed fusion using in-situ thermographic monitoring”, Progress in Additive Manufacturing, 5, 3, 277-285 (2020).

160. M.F. Khan, A. Alam, M.A. Siddiqui, M.S. Alam, Y. Rafat, N. Salik, I. Al-Saidan, “Real-time defect detection in 3D printing using machine learning”, Materials Today: Proceedings, 42, 521-528 (2021).

161. O. Davtalab, A. Kazemian, X. Yuan, B. Khoshnevis, “Automated inspection in robotic additive manufacturing using deep learning for layer deformation detection”, Journal of Intelligent Manufacturing, 33, 3, 771-784 (2022).

162. Z. Snow, B. Diehl, E.W. Reutzel, A. Nassar, “Toward in-situ flaw detection in laser powder bed fusion additive manufacturing through layerwise imagery and machine learning”, Journal of Manufacturing Systems, 59, 12-26 (2021).

163. X. Li, X. Jia, Q. Yang, J. Lee, “Quality analysis in metal additive manufacturing with deep learning, Journal of Intelligent Manufacturing” 31, 2003-2017 (2020).

164. S. Fathizadan, F. Ju, Y. Lu, “Deep representation learning for process variation management in laser powder bed fusion”, Additive Manufacturing, 42, 101961 (2021).

165. E. Westphal, H. Seitz, “A machine learning method for defect detection and visualization in selective laser sintering based on convolutional neural networks”, Additive Manufacturing, 41 101965 (2021).

166. J.-O. Andersson, T. Helander, L. Höglund, P. Shi, B. Sundman, Thermo-Calc & DICTRA, computational tools for materials science, Calphad 26(2), 273-312 (2002).

167. W. Huang, H. Wang, T. Rinker, W. Tan, “Investigation of metal mixing in laser keyhole welding of dissimilar metals”, Materials & Design, 195, 109056 (2020).

168. J.A. Mitchell, F. Abdeljawad, C. Battaile, C. Garcia-Cardona, E.A. Holm, E.R. Homer, J. Madison, T.M. Rodgers, A.P. Thompson, V. Tikare, “Parallel simulation via SPPARKS of on-lattice kinetic and Metropolis Monte Carlo models for materials processing”, Modelling and Simulation in Materials Science and Engineering, 31, 5, 055001 (2023).

169. W. Li, M. Soshi, “Modeling analysis of grain morphologies in Directed energy deposition (DED) coating with different laser scanning patterns”, Materials Letters, 251, 8-12 (2019).

170. W.E. Frazier, L. Li, K.S. Choi, Y. Fu, Z. Xu, V.V. Joshi, A. Soulami, “Microstructure-process relationships in monolithic U-10Mo fuel foil single-pass rolling: A parametric simulation study”, Journal of Nuclear Materials 576, 154271(2023).

171. F. Graner, J.A. Glazier, “Simulation of biological cell sorting using a two-dimensional extended Potts model”, Physical review letters, 69, 13, 2013 (1992).

APPENDIX A. NICKEL-BASED ALLOY SCORECARDS

Table A-1. Scorecard for Alloy 800H

Category	Criteria and corresponding ranking					
Manufacturing/ powder	Powder availability: 1	Powder properties: ND	Powder chemistry: ND	Cost: ND	Recycling: ND	—
Manufacturing/ components	Printability (LPBF): 3	Defects: 3	Post-treatment: 3	Processing window: ND	Weldability: ND	Surface roughness or finish: ND
History and applications	NE experience: 0	Other industry experience: 0	Data availability: 0	Code data availability: 5	Experience with non-LPBF AM: 0	Scaling up: ND
Mechanical properties	Creep: ND	Fatigue: ND	Creep-fatigue: ND	High-temperature tensile strength: ND	Room temperature: ND	—
Environmental effects	Radiation resistance: ND	Oxidation resistance: ND	Stress corrosion cracking: ND	Molten salt: ND	Liquid metal: ND	—
Physical properties	Thermal properties: ND	Solidification-relevant properties: ND	Other modeling-relevant properties: ND	CT-relevant properties: ND	—	—
Microstructure	Material homogeneity: ND	Microstructure stability: ND	LPBF microstructure specificity: 3	—	—	—
ND: not determined						

Table A-2. Scorecard for Alloy 617

Category	Criteria and corresponding ranking					
Manufacturing/ powder	Powder availability: 2	Powder properties: ND	Powder chemistry: ND	Cost: ND	Recycling: ND	—
Manufacturing/ components	Printability (LPBF): ND	Defects: ND	Post-treatment: ND	Processing window: ND	Weldability: ND	Surface roughness or finish: ND
History and applications	NE experience: 0	Other industry experience: 0	Data availability: 0	Code data availability: 5	Experience with non-LPBF AM: 1	Scaling up: ND
Mechanical properties	Creep: ND	Fatigue: ND	Creep-fatigue: ND	High-temperature tensile strength: ND	Room temperature: ND	—
Environmental effects	Radiation resistance: ND	Oxidation resistance: ND	Stress corrosion cracking: ND	Molten salt: ND	Liquid metal: ND	—

Table A-2. Scorecard for Alloy 617 (continued)

Category	Criteria and corresponding ranking					
Physical properties	Thermal properties: ND	Solidification-relevant properties: ND	Other modeling-relevant properties: ND	CT-relevant properties: ND	—	—
Microstructure	Material homogeneity: ND	Microstructure stability: ND	LPBF microstructure specificity: ND	—	—	—
ND: not determined						

Table A-3. Scorecard for Alloy 230

Category	Criteria and corresponding ranking					
Manufacturing/ powder	Powder availability: 4	Powder properties: ND	Powder chemistry: 3	Cost: 3	Recycling: ND	—
Manufacturing/ components	Printability (LPBF): 3	Defects: ND	Post-treatment: ND	Processing window: ND	Weldability: ND	Surface roughness or finish: ND
History and applications	NE experience: 0	Other industry experience: 0	Data availability: 0	Code data availability: 0	Experience with non-LPBF AM: ND	Scaling up: ND
Mechanical properties	Creep: ND	Fatigue: ND	Creep-fatigue: ND	High-temperature tensile strength: ND	Room temperature: ND	—
Environmental effects	Radiation resistance: ND	Oxidation resistance: ND	Stress corrosion cracking: ND	Molten salt: ND	Liquid metal: ND	—
Physical properties	Thermal properties: ND	Solidification-relevant properties: ND	Other modeling-relevant properties: ND	CT-relevant properties: ND	—	—
Microstructure	Material homogeneity: ND	Microstructure stability: ND	LPBF microstructure specificity: ND	—	—	—
ND: not determined						

Table A-4. Scorecard for Alloy 233

Category	Criteria and corresponding ranking					
Manufacturing/ powder	Powder availability: 2	Powder properties: ND	Powder chemistry: ND	Cost: ND	Recycling: ND	—
Manufacturing/ components	Printability (LPBF): ND	Defects: ND	Post-treatment: ND	Processing window: ND	Weldability: ND	Surface roughness or finish: ND
History and applications	NE experience: 0	Other industry experience: 0	Data availability: 0	Code data availability: 0	Experience with non-LPBF AM: ND	Scaling up: ND
Mechanical properties	Creep: ND	Fatigue: ND	Creep-fatigue: ND	High-temperature tensile strength: ND	Room temperature: ND	—
Environmental effects	Radiation resistance: ND	Oxidation resistance: ND	Stress corrosion cracking: ND	Molten salt: ND	Liquid metal: ND	—
Physical properties	Thermal properties: ND	Solidification-relevant properties: ND	Other modeling-relevant properties: ND	CT-relevant properties: ND	—	—
Microstructure	Material homogeneity: ND	Microstructure stability: ND	LPBF microstructure specificity: ND	—	—	—
ND: not determined						

Table A-5. Scorecard for Alloy 740H

Category	Criteria and corresponding ranking					
Manufacturing/ powder	Powder availability: 2	Powder properties: ND	Powder chemistry: ND	Cost: ND	Recycling: ND	—
Manufacturing/ components	Printability (LPBF): ND	Defects: ND	Post-treatment: ND	Processing window: ND	Weldability: 4	Surface roughness or finish: ND
History and applications	NE experience: 0	Other industry experience: 0	Data availability: 0	Code data availability: 0	Experience with non-LPBF AM: ND	Scaling up: ND
Mechanical properties	Creep: ND	Fatigue: ND	Creep-fatigue: ND	High-temperature tensile strength: ND	Room temperature: ND	—
Environmental effects	Radiation resistance: ND	Oxidation resistance: ND	Stress corrosion cracking: ND	Molten salt: ND	Liquid metal: ND	—

Table A-5. Scorecard for Alloy 740H (continued)

Category	Criteria and corresponding ranking					
Physical properties	Thermal properties: ND	Solidification-relevant properties: ND	Other modeling-relevant properties: ND	CT-relevant properties: ND	—	—
Microstructure	Material homogeneity: ND	Microstructure stability: ND	LPBF microstructure specificity: ND	—	—	—
ND: not determined						

Table A-6. Scorecard for Alloy GRX-810

Category	Criteria and corresponding ranking					
Manufacturing/ powder	Powder availability: 1	Powder properties: ND	Powder chemistry: ND	Cost: ND	Recycling: ND	—
Manufacturing/ components	Printability (LPBF): ND	Defects: ND	Post-treatment: ND	Processing window: ND	Weldability: 4	Surface roughness or finish: ND
History and applications	NE experience: 0	Other industry experience: 0	Data availability: 1	Code data availability: 0	Experience with non-LPBF AM: 0	Scaling up: ND
Mechanical properties	Creep: 4	Fatigue: ND	Creep-fatigue: ND	High-temperature tensile strength: 4	Room temperature: ND	—
Environmental effects	Radiation resistance: ND	Oxidation resistance: ND	Stress corrosion cracking: ND	Molten salt: ND	Liquid metal: ND	—
Physical properties	Thermal properties: ND	Solidification-relevant properties: ND	Other modeling-relevant properties: ND	CT-relevant properties: ND	—	—
Microstructure	Material homogeneity: ND	Microstructure stability: ND	LPBF microstructure specificity: ND	—	—	—
ND: not determined						

Table A-7. Scorecard for Alloy Hastelloy N

Category	Criteria and corresponding ranking					
Manufacturing/ powder	Powder availability: 1	Powder properties: ND	Powder chemistry: ND	Cost: ND	Recycling: ND	—
Manufacturing/ components	Printability (LPBF): ND	Defects: ND	Post-treatment: ND	Processing window: ND	Weldability: ND	Surface roughness or finish: ND
History and applications	NE experience: 0	Other industry experience: 0	Data availability: 0	Code data availability: 0	Experience with non-LPBF AM: 1	Scaling up: ND
Mechanical properties	Creep: ND	Fatigue: ND	Creep-fatigue: ND	High-temperature tensile strength: ND	Room temperature: ND	—
Environmental effects	Radiation resistance: ND	Oxidation resistance: ND	Stress corrosion cracking: ND	Molten salt: ND	Liquid metal: ND	—
Physical properties	Thermal properties: ND	Solidification-relevant properties: ND	Other modeling-relevant properties: ND	CT-relevant properties: ND	—	—
Microstructure	Material homogeneity: ND	Microstructure stability: ND	LPBF microstructure specificity: ND	—	—	—
ND: not determined						

Table A-8. Scorecard for Alloy 244

Category	Criteria and corresponding ranking					
Manufacturing/ powder	Powder availability: 1	Powder properties: ND	Powder chemistry: ND	Cost: ND	Recycling: ND	—
Manufacturing/ components	Printability (LPBF): ND	Defects: ND	Post-treatment: ND	Processing window: ND	Weldability: ND	Surface roughness or finish: ND
History and applications	NE experience: 0	Other industry experience: 0	Data availability: 0	Code data availability: 0	Experience with non-LPBF AM: 0	Scaling up: ND
Mechanical properties	Creep: ND	Fatigue: ND	Creep-fatigue: ND	High-temperature tensile strength: ND	Room temperature: ND	—
Environmental effects	Radiation resistance: ND	Oxidation resistance: ND	Stress corrosion cracking: ND	Molten salt: ND	Liquid metal: ND	—

Table A-8. Scorecard for Alloy 244 (continued)

Category	Criteria and corresponding ranking					
Physical properties	Thermal properties: ND	Solidification-relevant properties: ND	Other modeling-relevant properties: ND	CT-relevant properties: ND	—	—
Microstructure	Material homogeneity: ND	Microstructure stability: ND	LPBF microstructure specificity: ND	—	—	—
ND: not determined						